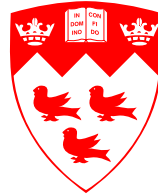


Signatures of Cosmic Strings on the Dark Matter Distribution

Disrael Camargo Neves da Cunha



Department of Physics
McGill University
Montréal, Québec, Canada

September 2019

A thesis submitted to McGill University in partial fulfillment of the requirements for the
degree of
Doctor of Philosophy.

© 2019 Disrael Camargo Neves da Cunha

Acknowledgments

I would like to thank my advisor, Professor Robert Brandenberger, for his exceptional guidance throughout my doctorate studies. More than an inspiring example on how to be a researcher and an educator, Professor Brandenberger has the ability to attentively instruct into the various aspects of academic life, including helping me to express my questions and ideas adequately, build collaborations and more importantly be a passionate physicist. Next, I would like to give my gratitude to my collaborators Oscar Hernández, Joachim Harnois-Déraps, Adam Amara, Alexandre Refregier, and Samuel Laliberte. I also would like to thank for the hospitality received at various institutions that I visited, including the Cosmology Research Group at ETH Zurich, Center for Computational Astrophysics at the Flatiron Institute, Tufts Institute of Cosmology, Harvard-Smithsonian Center for Astrophysics, Cosmology Group of the Institute for Theoretical Physics at the University of Heidelberg, International Centre for Theoretical Physics at Trieste and Brazilian National Observatory. Visiting those places and exchanging ideas were a fundamental part for my Ph.D., so I would like to thank the following people for the enriching conversations I had abroad: Adam Amara, Alexandre Refregier, Raphael Sgier, Tomasz Kacprzak, Aurel Schneider, Hamsa Padmanabhan, Janis Fluri, Andrina Nicola, Jailson Alcaniz, Beethoven dos Santos, Luca Amendola, Javier Rubio, David Spergel, Francisco Villaescusa-Navarro, Stephen Feeney, Alex Vilenkin, Ken Olum, Lars Hernquist and Douglas Finkbeiner.

I would like to thank the members of Robert Brandenberger's research group, visitors, colleagues post-docs and professors at McGill university for always maintaining a great environment to share ideas: Hossein Bazrafshan, Ryo Namba, Samuel Laliberte, Jerome Quintin, Bryce Cyr, Omar Alaryani, Guilherme Franzmann, Ziwei Wang, Matthew Muscat, Elisa Ferreira, Evan McDonough, Leila Graef, Yuki Omori, Yi-Fu Cai, Heliudson Bernardo, Renato da Costa, Rodrigo Cuzinatto, Bao-Min Gu, Daisuke Yoshida, Madeleine Anthonisen, Zeinab Sherkatghanad, Francis Duplessis, William Hipolito-Ricaldi and Rudnei Ramos, Gabriel Denicol, Ian Morrison, Gim Seng Ng and Shirley Ho, Mohit Bhardwaj, Laure-Anne Douxchamps, Maxim Emelin, Avi Friedlander, Yan Gobeil, Sigtryggur Hauks-son, Anh-Kho Trinh, Ioannis Tsiares and Zahra Zahraee. I appreciate the guidance given to me at McGill by professors Adrian Liu, Matt Dobbs, Gilbert Holder, Cynthia Chiang, and Jonathan Sievers. I had the great opportunity to work alongside the following summer students, which I acknowledge the effort and disponibility for periodical dialogues:

Félix Valin, Oumnia Bazi, Hyunji Lee, Maki Shimizu, Eloise Chakour, Samuel Laliberte, Fairhurst Lyons, Franco La Braca, Su Yu Ding, Justin Dragoman, and Mesbah Alsarraj. I also would like to thank the following McGill physics department staff: Eddie Del Campo for the friendliness, Paul Mercure for the patience, and especially Juan Gallego for going to the very bottom of computational technical problems and finally finding their solutions. Special thanks also go to Jackson Maia and Marco Maia.

I am thankful for the financial support from CAPES (science without borders), Natural Sciences and Engineering Research Council of Canada (NSERC), McGill Physics Department and McGill Graduate and Postdoctoral Studies.

Finally, I would like to thank my partner Julia Zamboni for the shared experiences during our Ph.D. and also for motivate me on giving my best effort to perform research, for which this journey wouldn't be conceivable without the loveling company, support, and influence. I could not miss the chance to give my thanks for the rest of my family, for the support throughout this phase.

Abstract

A broad class of models that describe physics beyond the Standard Model of Particle Physics predicts that topological defects, such as cosmic strings, will appear during a phase transition on the very early universe. Therefore cosmological data provides an important arena to test extensions of the Standard Model of Particle Physics. In this thesis, I will show that searches for cosmic strings using the Cosmic Microwave Background temperature power spectrum can put the most robust constraint to date on the parameter that characterizes the cosmic string, its tension. Given that new telescopes and satellites are providing us with an unprecedented amount of data on the large scale structure (LSS) of the universe as seen through the distribution of galaxies and 21cm intensity maps, it is essential to ask how powerful will LSS be to constrain the cosmic string parameter. It will be shown that cosmic string changes its surroundings by creating a wake consisted of a planar overdense region that forms behind the string as it passes by the dark matter distribution. First, an analytical study of the wake disruption is presented. After that, the thesis shows the characterization of cosmic string wakes in LSS by the use of numerical computations simulating the effects of cosmic string wakes and aiming to find optimal statistics that extract such effects in the presence of the “noise” produced by the dominant source of fluctuations. Codes which run statistics designed to identify the string wake signal have been developed. They include wavelet, ridgelet (bi and tridimensional), curvelet (bidimensional) transforms and smoothing algorithms. The conclusion is that a wake with tension slightly less than the current bound can be identifiable with high statistical significance down to redshift at least $z = 3$ in tomographic dark matter maps.

Abrégé

Une large classe de modèles décrivant la physique au-delà du modèle standard de la physique des particules prédit que des défauts topologiques, tels que les cordes cosmiques, apparaîtront durant une transition de phase au début de l'univers. Par conséquent, les données cosmologiques constituent un domaine important pour mettre à l'épreuve les extensions du modèle standard de la physique des particules. Dans cette thèse, je montrerai que la recherche de cordes cosmiques à l'aide du spectre de puissance de la température du fond diffus cosmologique permet de mettre la contrainte la plus robuste sur le paramètre qui caractérise les cordes cosmiques, c'est-à-dire leur tension. Étant donné que les nouveaux télescopes et satellites nous fournissent une quantité sans précédent de données sur les structures à grande échelle de l'univers telles que mesurées à partir de la distribution des galaxies et des cartes d'intensité de la raie à 21 cm, il est essentiel de se demander quelle sera la portée des structures à grande échelle de l'univers pour contraindre le paramètre des cordes cosmiques. Nous montrerons qu'une corde cosmique modifie son environnement en créant un sillage constitué d'une région surfacique plane qui se forme derrière la corde au passage de la distribution de la matière noire. Tout d'abord, une étude analytique de la perturbation de sillage est présentée. Après cela, la thèse montre la caractérisation des sillages de cordes cosmiques dans les structures à grande échelle de l'univers par l'utilisation de calculs numériques simulant les effets des sillages des cordes cosmiques et visant à trouver des statistiques optimales permettant d'extraire ces effets en présence du « bruit » produit par la source dominante des fluctuations. Des algorithmes qui calculent des quantités statistiques conçues pour identifier le signal des sillages de cordes cosmiques ont été développés. Ils incluent des transformations en ondelettes, en arêtelettes (bi et tridimensionnelles), en courbelettes (bidimensionnelles) et des algorithmes de lissage. La conclusion est qu'un sillage avec une tension donnée à peine inférieure à la limite actuelle peut être identifié avec une signification statistique élevée jusqu'à un décalage vers le rouge d'au moins $z = 3$ dans les cartes de matière noire tomographiques.

Contents

Preface	1
1 Overview	3
I Cosmic Strings and Cosmology	5
2 Introduction	6
2.1 Standard Cosmology	6
2.2 Cosmic Strings	11
2.3 Cosmic String network formation and evolution	17
2.4 Robust Observational Constraint on Cosmic Strings	19
3 Cosmic string wakes	21
3.1 Wake formation	21
3.2 Wake evolution	23
4 Probing particle physics beyond the Standard Model with Cosmic Strings	28
4.1 Signature of CS in the CMB temperature and polarization maps in position space	28
4.1.1 Signature of wakes in the CMB polarization maps	29
4.2 Signature of wakes in the 21 cm hydrogen transition line	31
4.3 Brief comments on methods of cosmic string detection in position space . .	33

II Publications	37
5 Disruption of Cosmic String Wakes by Gaussian Fluctuations	38
5.1 Introduction	38
5.2 String Wake Review	41
5.3 Displacement Condition	43
5.4 Local Delta Condition	44
5.5 Global Sigma Condition	47
5.6 Discussion and Conclusions	51
6 Dark Matter Distribution Induced by a Cosmic String Wake in the Non-linear Regime	53
6.1 Introduction	53
6.2 Wake Disruption	57
6.3 Simulations	59
6.3.1 The Code	59
6.3.2 Wake Insertion	60
6.3.3 Known limitations	63
6.3.4 Simulations	66
6.4 Statistical Analysis	69
6.4.1 1-d Projections	69
6.4.2 Spherical Statistic	76
6.5 Conclusions and Discussion	80
6.6 Peak Heights	81
7 Cosmic String Wake Detection using 3D Ridgelet Transformations	83
7.1 Introduction	83
7.2 Cosmic String Wake Formation	86
7.3 The Cosmological N-body simulations	88
7.4 The 3D Ridgelet Transform	90
7.5 Plane Wakes signature in partial ridgelet transformations	93
7.6 Weak plane wakes detection in partial ridgelet transformations	97
7.7 Conclusions and Discussion	102

8 Signature of a Cosmic String Wake at $z = 3$	106
8.1 Introduction	106
8.2 Review of Cosmic string wakes in the non-linear regime	109
8.3 Simulations	111
8.4 Analysis	111
8.4.1 A curvelet filtering of the two-dimensional projections	115
8.4.2 Wake signal extraction with wake orientation prior	117
8.4.3 Wake signal extraction without wake orientation prior	118
8.5 Conclusion	121
9 Conclusion	122
Bibliography	124

List of Figures

2.1	The <i>Planck</i> 2018 CMB temperature map.	10
2.2	<i>Planck</i> 2018 CMB Power spectra for temperature anisotropies.	11
2.3	Loop production mechanism.	18
2.4	Scalling cosmic string solution.	19
3.1	The plane perpendicular to a long cosmic string with a missing angle. . . .	22
3.2	Conical space in the plane perpendicular to a long cosmic string	23
3.3	Particles trajectories around a cosmic string	24
3.4	Displacement on a test particle due to the wake presence	25
4.1	Kaiser-Stebbins effect	29
5.1	Plot of $\Delta(k_3(z), z)$ (vertical axis) as a function of redshift z (horizontal axis) for $G\mu = 10^{-7}$ (black line) and $G\mu = 10^{-11}$ (gray line).	46
5.2	The value of $G\mu$ (vertical axis in units of 10^{-7}) above which the local Delta wake stability condition is satisfied as a function of redshift z (horizontal axis).	47
5.3	The r.m.s. value of the density contrast of the Gaussian perturbations in an anisotropic region which corresponds to the size of a wake produced at t_{eq} (vertical axis) as a function of redshift (horizontal axis). Note that the density fluctuations remain smaller than one.	50
6.1	Plot of fractional error of the dimensionless power spectrum compared with the HALOFIT predictions of the online CAMB tool	61

6.2	Density contrast of the two-dimensional projection of the dark matter distribution for a $G\mu = 4.0 \times 10^{-6}$ wake at redshift $z = 31, 10$ and 3 (from top to bottom, respectively). The color bar on the bottom associates each color with the corresponding density contrast	64
6.3	Plot of the induced displacement due to the wake as a function of axis position Z (horizontal axis) for redshift $z = 10$ and string tension $G\mu = 8 \times 10^{-7}$	66
6.4	Plot of the displacement induced by the wake (in blue) for different values of the scale factor. The expected displacement evolution from Zel'dovich approximation is shown in red.	67
6.5	Each panel shows the density contrast of the density field projected in a $(64h^{-1}\text{Mpc}/h)^2$ area. Each row depicts a redshift snapshot, chosen to be $z = 10, 7, 4, 2, 0$ from top to bottom. The left column corresponds to pure ΛCDM , the middle contains a $G\mu = 8 \times 10^{-7}$ wake and the right column contains a $G\mu = 1 \times 10^{-7}$ wake. The color bar on the bottom associates each color with the corresponding density contrast	68
6.6	Each panel shows the density contrast of the density field projected in a $(64 \text{ Mpc}/h)$ axis perpendicular to the wake, when there is one. Each row depicts a redshift snapshot, chosen to be $z = 15, 10, 7, 5, 3, 0$ from top to bottom. The left column corresponds to pure ΛCDM , the middle contains a $G\mu = 8 \times 10^{-7}$ wake and the right column contains a $G\mu = 1 \times 10^{-7}$ wake.	70
6.7	Continuous wavelet transforms of the density contrast of the 1-d projected dark matter density. The horizontal axis is the position parameter of the wavelet decomposition (with $Z = 32$ being the position of the wake), and the vertical axis is the width of the wavelet. The top panel is for a simulation without a wake, the middle panel includes a wake with $G\mu = 8 \times 10^{-7}$, and the bottom panel has a wake with $G\mu = 10^{-7}$. Note that the ΛCDM fluctuations are the same in all three simulations.	72

6.8	Reconstruction of the 1-d density contrast from the filtered wavelet transforms. The vertical axis is the density contrast, the horizontal axis is the distance of the projection plane from the wake plane. The top panel is the result of a simulation without a wake, the middle panel has a wake with $G\mu = 8 \times 10^{-7}$, and the bottom panel has a wake with $G\mu = 10^{-7}$. The data is for a redshift $z = 10$. Note that the wake signal is greatly enhanced compared to the original 1-d projection graphs of Fig. 8.	74
6.9	Continuous wavelet transforms after filtering. The axes are like in figure 7. The top panel is without a wake, the middle panel has a wake with $G\mu = 8 \times 10^{-7}$, and the bottom panel is for a wake with $G\mu = 10^{-7}$	75
6.10	Signal to noise analysis for the 1-d projections after wavelet transformation, filtering and reconstruction, and for the finer of samplings in wavelet width. The horizontal axis shows the redshift, the vertical axis is the signal to noise ratio. The two pair of curves in the bottom contains a wake with $G\mu = 10^{-7}$, and the top two curves are for a wake with $G\mu = 8 \times 10^{-7}$. The two members of a pair of curves correspond to different redshifts of wake insertion (as is obvious from the starting points of the curves). The points that are not shown correspond to values for the signal to noise equal to zero.	77
6.11	Reconstructed map for a simulation with wake tension $G\mu = 1 \times 10^{-7}$ at redshift $z = 10$	78
6.12	The same map for a simulation without a wake, at redshift $z = 10$	78
6.13	40 \times zoom of the reconstructed map for a simulation with wake tension $G\mu = 1 \times 10^{-7}$ at redshift $z = 10$	79
6.14	40 \times zoom of the the same map for a simulation without a wake, at redshift $z = 10$	79
6.15	The peak values for simulations without a wake are marked by circles, for those with a wake with tension $G\mu = 10^{-7}$ inserted at redshift $z = 31$ and $z = 15$ by “*” and “+”, respectively, and for those with tension $G\mu = 8 \times 10^{-7}$ inserted at redshifts $z = 31$ and $z = 15$ by inverted triangles and “x”, respectively.	82

7.1	Geometry of a cosmic string wake [27, 28, 65, 66]. In the figure, v_s is the string velocity v , γ_s is the gamma factor $\gamma(v)$ and c_1 is a constant of order unity that depends on the length of the string.	87
7.2	Plot of the wavelet function $\psi(x)$ in dimensionless units.	93
7.3	Density contrast of a 2D projection of the box on the y-z plane [49]. The $32 h^{-1}\text{Mpc} \times 32 h^{-1}\text{Mpc} \times 32 h^{-1}\text{Mpc}$ data box contains a cosmic string wake caused by a cosmic string of tension $G\mu = 10^{-6}$ at the position $y = 0 h^{-1}\text{Mpc}$ and the redshift $z = 7$. The color scheme, shown on the right, depicts the range of possible values for the fluctuation ratio $\delta S/S$. Here, S is the mean surface density and δS is the difference between the local surface density and the mean surface density.	94
7.4	For a wake caused by a cosmic string of string tension $G\mu = 10^{-6}$ at redshift $z = 7$, the Radon transform $\mathbf{R}(\rho) = \mathbf{R}(\rho)(\theta_1, \theta_2, t)$ where $\theta_1 = \theta_2 = \pi/2$, is plotted for 10000 values of t between $-15 h^{-1}\text{Mpc}$ and $15 h^{-1}\text{Mpc}$. For this specific orientation and position, t corresponds to the y axis which gives us a density projection on the y axis. The width of the wake is $(1.1382 \pm 0.0003) \times 10^{-1} h^{-1}\text{Mpc}$, where the uncertainty is defined as half the distance between two evaluated values of t	95
7.5	For a wake caused by a cosmic string of tension $G\mu = 10^{-6}$ at redshift $z = 7$, the ratio $R(a)$ is depicted for 1000 values of a between $0 h^{-1}\text{Mpc}$ and $1.5 h^{-1}\text{Mpc}$. The ratio has a maximum at $a_{max} = (1.168 \pm 0.006) \times 10^{-1} h^{-1}\text{Mpc}$, where the uncertainty is defined as half the distance between two evaluated values of a . As a becomes larger, $R(a)$ eventually converges to 1 as the wake signal becomes indistinguishable from the Gaussian fluctuations.	96
7.6	For a wake cased by a cosmic string of tension $G\mu = 10^{-6}$ at redshift $z = 7$, the ridgelet coefficents \mathcal{R}_ρ are plotted for 1000 values of b between $-0.5 h^{-1}\text{Mpc}$ and $0.5 h^{-1}\text{Mpc}$ while imposing that $a = a_{max}$, $\theta_1 = \theta_2 = \pi/2$. The ridgelet coefficients have a maximum at $b_{max} = (0 \pm 8) \times 10^{-1} h^{-1}\text{Mpc}$. The uncertainty is defined as half the width at half maximum of the peak.	97

- 7.7 Sketch of the partial wavelet transformation. The ridgelet transform is computed inside a sphere the size of the box for different orientations $(\theta_1, \theta_2) \in [0, \pi] \times [0, \pi]$. The ridgelet function is constant along the planes normal to the direction vector $\vec{n}(\theta_1, \theta_2)$ shown in black. Therefore, we expect the ridgelet coefficients to be maximised when $\theta_1 = \theta_2 = \pi/2$; that is, when the plane with normal $\vec{n}(\theta_1, \theta_2)$ coincides with the plane formed by the wake. 98

7.8 Surface plot of \mathcal{R}_ρ for $a = a_{max}$, $b = 0 h^{-1}\text{Mpc}$ and 50^2 orientations $(\theta_1, \theta_2) \in [0, \pi] \times [0, \pi]$. The plot has a clear maximum at $\theta_1 = \theta_2 = \pi/2$ for a wake cased by a cosmic string of string tension $G\mu = 10^{-6}$ at redshift $z = 7$ 99

7.9 Density contrast of a 2D projection of the box onto the y-z plane at redshift $z = 10$ [49]. The $64 h^{-1}\text{Mpc} \times 64 h^{-1}\text{Mpc} \times 64 h^{-1}\text{Mpc}$ data box contains a wake caused by a cosmic string of tension $G\mu = 10^{-7}$ at the position $y = 0 h^{-1}\text{Mpc}$. The color scheme, shown on the right, shows the range of possible values for the fluctuation ratio $\delta\rho/\rho$ (ρ being the density). The wake is not visible by eye. 100

7.10 For a wake caused by a cosmic string of string tension $G\mu = 10^{-7}$ introduced at redshift $z = 31$ at the center of the box in the x-z plane, the Radon transform $\mathbf{R}(\rho) = \mathbf{R}(\rho)(\theta_1, \theta_2, t)$ where $\theta_1 = \theta_2 = \pi/2$, is plotted for 10000 values of t between $-32 h^{-1}\text{Mpc}$ and $32 h^{-1}\text{Mpc}$. For this specific orientation and position, t corresponds to the y axis which gives us a density projection onto the y-axis. The orange region shows how points in the original wake spread in the density projection at lower redshifts. 101

7.11 For a wake caused by a cosmic string of string tension $G\mu = 10^{-7}$ at redshift $z = 10$, the Radon transform of the data box with a wake (in blue) and without a wake (in orange) is plotted for 10000 values of t between $-32 h^{-1}\text{Mpc}$ and $32 h^{-1}\text{Mpc}$ for the fixed orientation $\theta_1 = \theta_2 = \pi/2$. The Radon transform is fitted to as a second degree polynomial shown in red. The studentized residuals reveal the presence of a small region of overdensity at $t = 0 h^{-1}\text{Mpc}$ in the blue plot which is not found in the orange plot. We conclude that this region of overdensity is caused by the wake. 102

7.12 For a wake caused by a cosmic string of string tension $G\mu = 10^{-7}$ at redshift $z = 10$, the mean value of the ratio $R(a)$ is plotted for 3000 values of a between $0.01 h^{-1}\text{Mpc}$ and $0.20 h^{-1}\text{Mpc}$. The dashed lines show the standard deviation with respect to the means. The mean ratio for the data boxes is plotted in blue while the mean ratios for the data boxes without wakes are plotted in red.	103
7.13 For a set of data boxes with a wake caused by a cosmic string of string tension $G\mu = 10^{-7}$ at redshift $z = 10$ (in blue) and a set of data boxes without wake (in red), the mean ridgelet coefficients \mathcal{R}_ρ are plotted for 1000 values of b between $-0.25 h^{-1}\text{Mpc}$ and $0.25 h^{-1}\text{Mpc}$ while imposing that $a = a_{max}$, $\theta_1 = \theta_2 = \pi/2$. The dashed lines show the standard deviation with respect to the means and the vertical black lines show the interval in which the peak caused by the wake can be detected when compared to a set of simulations without wakes.	104
7.14 Surface plot of \mathcal{R}_ρ for the data box with the wake caused by a cosmic string of string tension $G\mu = 10^{-7}$ at redshift $z = 10$ (on the left) and without a wake at the same redshift (on the right). In both cases, the values of the ridgelet coefficients are computed for $a = a_{max}$, $b = 0 h^{-1}\text{Mpc}$ and 50^2 orientations $(\theta_1, \theta_2) \in [0, \pi] \times [0, \pi]$. For this example of data box with a wake, the coefficients have a clear maximum at $\theta_1 = \theta_2 = \pi/2$. This maximum is not observable in the coefficients of the data box without a wake. Therefore, we conclude that the maximum in the ridgelet coefficients on the left plot is indeed caused by the wake.	105
8.1 Average displacement induced by the wake (in blue), compared with the analytical prediction (in red).	112
8.2 Average velocity perturbation induced by the wake (in blue), compared with the analytical prediction (in red).	112
8.3 Logarithm of the mass of a two-dimensional projection of simulation particles for lateral size $L = 4\text{Mpc}/h$ and redshift $z = 3$. The upper plot shows the simulation without the wake, and the plot on the bottom shows the simulation with a $G\mu = 10^{-7}$ wake at the central position of the z axis.	113

8.4	Logarithm of the mass of a two-dimensional projection of a slice of the simulation box with lateral size $L = 4Mpc/h$ and redshift $z = 3$. The upper plot shows the slice without the wake, and the plot on the bottom shows the slice with a $G\mu = 10^{-7}$ wake at the central position of the z axis.	114
8.5	Filtered version of the logarithm of the mass of a two-dimensional projection of a slice of the simulation box with lateral size $L = 4Mpc/h$ and redshift $z = 3$. The upper plot shows the slice without the wake, and the plot on the bottom shows the slice with a $G\mu = 10^{-7}$ wake at the center.	117
8.6	Distribution of the wake indicator S for the wake simulations (in red), and with pure ΛCDM (in blue).	118
8.7	Wake indicator S values for different orientations for a simulation box with lateral size $L = 4Mpc/h$ and redshift $z = 3$. The upper plot shows the spherical map without the wake, and the plot on the bottom shows the spherical map with a $G\mu = 10^{-7}$ wake.	119
8.8	Histogram in logarithmic scale of the S values for all 384 angles and ten simulation boxes with lateral size $L = 4Mpc/h$ and redshift $z = 3$. The blue histogram correspond to the simulations without wakes, and the red histogram correspond to $G\mu = 10^{-7}$ wakes.	120

List of Tables

- 6.1 Configuration of the various N -body simulations. L_{box} and nc are the side of the cosmological box and number of cells per dimension, respectively. 60

List of Acronyms

SMC	Standard Model of Cosmology
CMB	Cosmic Microwave Background
SMPP	Standard Model of Particle Physics
SSB	Spontaneous Symmetry Breaking
BAO	Baryonic Acoustic Oscillation

Preface

This thesis contains two peer-reviewed paper, one preprint and one paper submitted to a peer-reviewed journal listed below. Due to copyright reasons, some of the articles in this thesis could not be changed. Therefore to maintain consistency, virtually no changes were made in Chapters 5, 6, 7, and 8.

- D. C. N. da Cunha, O. F. Hernández, and R. H. Brandenberger, “Disruption of Cosmic String Wakes by Gaussian Fluctuations” Phys. Rev. D93, 123501 (2016), arXiv:1508.02317 [astro-ph.CO] .
- D. C. Neves da Cunha, J. Harnois-Deraps, R. Brandenberger, A. Amara, and A. Refregier, “Dark Matter Distribution Induced by a Cosmic String Wake in the Nonlinear Regime”, Phys. Rev. D98, 083015 (2018), arXiv:1804.00083 [astro-ph.CO] .
- S. Laliberte, R. Brandenberger, and D. C. N. da Cunha, “Cosmic String Wake Detection using 3D Ridgelet Transformations”, (2018), arXiv:1807.09820 [astro-ph.CO].
- D. C. N. da Cunha, “Signature of a Cosmic String Wake at $z = 3$ ”, (2018), arXiv:1810.07737 [astro-ph.CO].

Contributions of the Author

In the first paper, I had the main idea of using anisotropic window functions to characterize the cosmic string wake. All authors contributed equally to discussions, computations, and writing. All authors contributed equally to the discussions on the second paper. The simulations runs were performed by myself under the guidance of Dr. Harnois-Deraps, and all the computational analyses were performed by myself. I was responsible for writing $\approx 75\%$ of the material, Dr. Harnois-Deraps wrote $\approx 10\%$, and Professor Brandenberger

wrote $\approx 15\%$. For the third paper, all authors contributed equally to discussions. I was responsible for running the simulations, Laliberte was responsible for writing most of the document and performing the computational analysis and Professor Brandenberger and myself checked the manuscript.

Chapter 1

Overview

Cosmology is the branch of science that studies the origin, composition, and evolution of the universe. Since it is known today that the universe is expanding and cooling, it is clear that understanding the properties of the very early universe involves studying a regime of small scales and high energies. Therefore, fundamental physics and cosmology are intimately interconnected, and cosmological probes offer an arena to probe both the Standard Model of particle physics and its proposed extensions.

A broad class of models that describe physics beyond the standard model predicts the appearance of topological defects, which are regions in space of trapped energy density. The consequences of topological defects in the large scale structure (LSS) of the universe is studied by performing numerical computations that simulate the influences of topological defects, aiming to find optimal statistics that extract such effects.

The main focus of this thesis is a one-dimensional type of topological defect called “cosmic string” and its effect on the LSS of the universe. The primary goal of this project is to model the impact of such strings on the distribution of matter in the universe, applying statistical tests for their identification and predicting their expected signals in cosmological observations. The most important effect of a cosmic string on the LSS is the production of a wake –a sheet-like overdensity that forms behind the string as it passes through the dark matter distribution. The thickness of this wake depends on the string tension μ , which is the main parameter that describes the gravitational effects of the string. The presented project concerns the extraction of this signal in the presence of the “noise” produced by the dominant source of fluctuations (Λ *CDM* fluctuations). Currently, the most robust

constraint on the cosmic string tension comes from cosmic microwave background (CMB) analyses, and it is $G\mu < 1.5 \times 10^{-7}$, where G is Newton's gravitational constant. This project aims to find how powerful LSS data are for constraining the cosmic string parameter, and which values for the cosmic string tension can be restricted using a robust statistical analysis of the LSS.

The thesis is organized into two parts. The first part is called *Cosmic Strings and Cosmology* and covers the basic physics and motivation necessary for the second part. The first part contains four chapters: *Introduction*, which shows an overview of cosmology, cosmic strings, and its current robust constraints; *Cosmic string wakes*, exposing how wakes of cosmic strings are formed and how they evolve; *Probing particle physics beyond the Standard Model with Cosmic Strings*, contains attempts to use spatial information to constrain the cosmic string parameter.

The second part of the thesis contains four publications: *Disruption of Cosmic String Wakes by Gaussian Fluctuations*, where the question if the Λ CDM fluctuations would disrupt the wake is approached; *Dark Matter Distribution Induced by a Cosmic String Wake in the Nonlinear Regime*, which studies the evolution of the LSS using N-body simulations of the distribution of dark matter particles, and implements a code for creating the initial conditions used in the N-body simulations with and without a cosmic string wake. In addition, a ridgelet statistic is designed to identify the string wake signal; *Cosmic String Wake Detection using 3D Ridgelet Transformations*, applying a similar strategy for the wake signal extraction; and *Signature of a Cosmic String Wake at $z = 3$* , showing that a $G\mu = 1 \times 10^{-7}$ wake is identifiable with high statistical significance down to $z = 3$ in a two-dimensional dark matter map.

Part I

Cosmic Strings and Cosmology

Chapter 2

Introduction

2.1 Standard Cosmology

Cosmology is the branch of science that studies the origin, composition, and evolution of the universe. Its study has a long and rich history, but only relatively recently, it became a science subject to experimental verification. An example was the observation of Hubble that the galaxies are moving away from us at a speed proportional to the distance. The rate of departure of galaxies is measured by the redshift z , which is the ratio between the emitted λ_E and received λ_R wavelength :

$$z + 1 = \frac{\lambda_R}{\lambda_E}. \quad (2.1.1)$$

A positive redshift indicates that the universe expanded (explaining the increase of the wavelength of light), and so the galaxies are moving away. Another useful way to measure the expansion of the universe is to divide the emitted wavelength $\lambda_E(t)$ at time t by the received wavelength λ_R today:

$$a(t) = \frac{\lambda_E}{\lambda_R}(t). \quad (2.1.2)$$

$a(t)$ measures the length of an object at time t compared to its length today. The luminosity distance, defined as $d_L = (\frac{L}{4\pi F^2})$ is used to measure the distance from other galaxies to us, where L is the intrinsic luminosity of the object and F is the measured flux.

Hubble discovered the following experimental law:

$$z \approx H_0 d_L. \quad (2.1.3)$$

The proportionality constant is known as the Hubble constant of the present time, and it is defined as $H_0 = 100h \text{ km sec}^{-1} \text{ Mpc}^{-1}$, where h is measured by experiments. For example, the measurements in [1] show $h = 0.72 \pm 0.008$. For small velocities compared to the speed of light, this law is rewritten as:

$$v \approx H_0 d_L, \quad (2.1.4)$$

since the redshift z caused by moving-away sources is given by $z = v/c$. This form of the Hubble's law permits the interpretation that galaxies are moving away from each other with a velocity proportional to their distance, which is a straightforward conclusion if space is expanding.

The inverse of the Hubble parameter is known as the Hubble radius. At a distance greater than this radius, the velocity associated with the expansion is higher than the speed of light, and therefore the photons outside this region cannot reach the center and are not in causal contact with the central portion of this region.

Hubble's observation allowed him to discard the static universe model initially proposed by Einstein in favor of a dynamic universe. Extrapolation into the past of a dynamic, expansive universe leads to the conclusion that it passed through an early period of high energy known as the Big Bang. In its current state, the Standard Model of Cosmology (SMC) is the dominant paradigm of cosmology. It assumes the validity of three principles: General Relativity; the Cosmological Principle (spatial homogeneity and isotropy of the universe on large scales) and that a perfect gas describes well the content of the universe. Einstein's equations of General Relativity describe the dynamics of the universe, and relate the evolution of the metric of the cosmos with the distribution of sources of gravitational fields. The SMC leads to a series of predictions, such as the existence of an initial state of high energy density (or Big Bang), the existence and black body nature of the Cosmic Microwave Background (CMB), and the description of the abundance of light elements.

The Robertson-Walker metric assumes a homogeneous and isotropic space, and it is

given by

$$ds^2 = -dt^2 + a^2(t) \left[\frac{dr^2}{1 - \kappa r^2} + r^2 d\Omega^2 \right], \quad (2.1.5)$$

where $\kappa = \frac{K}{a^2(t)}$ and $K \in (-1, 0, 1)$, depending on the spatial curvature of the universe (hyperbolic, planar or spherical, respectively). Here, $a(t)$ is the scale factor, related to the Hubble parameter at time t by the equation $H(t) = \frac{\dot{a}(t)}{a(t)}$ ¹. The distance measured by the coordinate r is called comoving distance. If two test particles are always at fixed comoving distance r , they will depart from each other because their physical distance $r_{phy} = a(t)r$ will increase.

Applying Einstein's equations to the metric above and using the energy-momentum tensor given by a perfect gas, $T_\nu^\mu = diag(\rho, -p, -p, -p)$ (where ρ is the energy density and p is the pressure of the perfect gas) two independent equations result:

$$d(\rho a^3) = -pd(a^3) \quad (2.1.6)$$

$$\frac{k}{H^2 a^2} = \frac{\rho}{3H^2/8\pi G} - 1 = \Omega - 1, \quad (2.1.7)$$

where the last equality is used to define Ω , which is the ratio of the density ρ to the critical density $\rho_c = \frac{3H^2}{8\pi G}$, which is $1.879h^2 \times 10^{-29} g \text{ cm}^{-3}$ today. Equation (2.1.6) is nothing but the equation of energy conservation for the gas (first law of thermodynamics) and equation (2.1.7) is called the Friedmann equation.

The Friedmann equation (2.1.7) provides a criterium for the spatial curvature: since $H^2 a^2 \geq 0$, there is a correspondence between the k sign and the Ω sign. If $\Omega > 1$ (higher energy density than the critical density) then $k = 1$, and it will lead to a spherical universe. Similarly, $\Omega = 1$ and $\Omega \leq 1$ implies $k = 0$ and $k = -1$, respectively.

The energy conservation equation (2.1.6) provides the dependence of the energy density on the scale factor: for an energy density of radiation (where $p = \frac{1}{3}\rho$), $\rho \propto a^{-4}$; for an energy density of matter ($p = 0$), $\rho \propto a^{-3}$; and a density of energy of the cosmological constant ($p = -\rho$), $\rho \propto const$. The various components of the energy density at any time add together to form the total energy density $\rho = \rho_{cc} + \rho_{dm} + \rho_{bm} + \rho_r + \rho_n$, corresponding to the sum of the energy densities associated with the cosmological constant (or dark energy),

¹This definition for the Hubble constant together with the definition of the physical distance $r_{phy} = a(t)r$ allows us to obtain 2.1.4, by only taking the temporal derivative of r_{phy} . The result is $v_{phy} = H(t)r_{phy}$

dark matter, baryonic matter, radiation, and neutrinos, respectively. Other contributions may be considered, depending on the model. Measurements indicate that currently there is a dominant contribution of dark energy $\Omega_{cc} = 0.74$, followed by dark matter $\Omega_{dm} = 0.2$ and a small contribution of baryonic matter $\Omega_{bm} = 0.05$. The other contributions are negligible today. Since $\rho_r \propto a^{-4}$, $\rho_m \propto a^{-3}$ and $\rho_{CC} \propto const$, it follows that the current period corresponds to a cosmological constant dominated universe, preceded by a relatively recent period which had the dominant contribution to the energy density coming from matter, and before that a much earlier period when the dominant contribution was from radiation. Inserting $\rho(t)$ in 2.1.7, the following results: $a \propto t^{\frac{1}{2}}$ for the universe dominated by radiation; $a \propto t^{\frac{2}{3}}$ when it is dominated by matter; and $a \propto e^{(H_0 t)}$ when it is dominated by the cosmological constant.

Initially, the universe was very hot, and as it cools, radiation decouples from matter (time of decoupling) which in turn forms neutral atoms (recombination time). From this period onwards, the radiation will no longer interact intensively with matter, because there will not be a considerable number of free charges, and the universe becomes transparent to photons. The radiation from the time of recombination is called CMB (Cosmic Microwave Background), and its existence was proposed theoretically by Ralph Alpher and Robert Herman in 1948 and discovered experimentally by Arno Penzias and Robert Wilson in 1964. The CMB has a blackbody spectrum with a temperature of $2.72548 \pm 0.00057 K$.

The hypothesis of homogeneity is only an approximation. If it were strictly true, the energy density of the universe would be precisely the same in all points, contradicting the existence of structures like galaxies (which have energy densities orders of magnitude higher than the average) and stars. Thus, the description of the content of the universe in terms of a homogeneous ideal gas no longer applies but must be viewed only as a first approximation. One can perturb the RW metric to account for the inhomogeneities, and treat the evolution of these fluctuations through a perturbative analysis of Einstein's equations. The characterization of fluctuations involves the quantification of the initial conditions of such fluctuations and the determination of their physical origins. Figure 2.1 shows the fluctuations of the CMB temperature map measured by the Planck collaboration [2]

The fluctuations of the primordial potential Φ are usually encoded in its power spectrum [4], defined as of

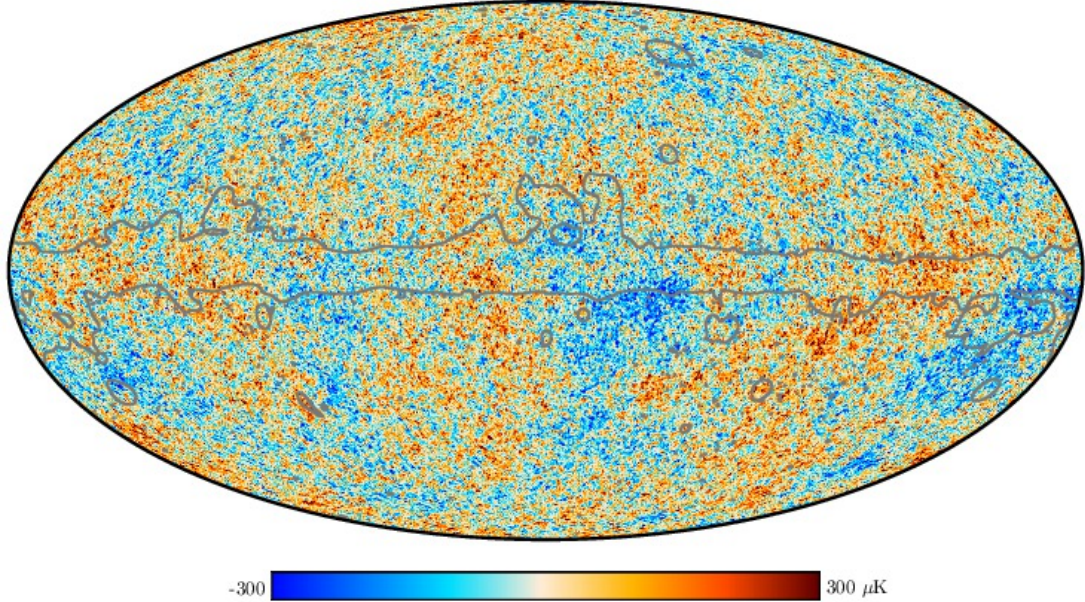


Figure 2.1 *Planck* 2015 CMB sky map taken from [3]. The CMB map has been masked and inpainted in regions where residuals from foreground emission are expected to be substantial. This mask, mostly around the Galactic plane, is delineated by a grey line in the full resolution temperature map. The color code indicates the fluctuations in temperature in μK .

$$\langle \Phi(\vec{k})\Phi^*(\vec{k}') \rangle = (2\pi)^3 P_\Phi(k)\delta^3(\vec{k} - \vec{k}'), \quad (2.1.8)$$

where the brackets denote an average over the distribution, $\Phi(\vec{k})$ is the gravitational potential in Fourier space, $\Phi^*(\vec{k}')$ its complex conjugate and $\delta^3(\vec{k} - \vec{k}')$ the three dimensional Dirac delta function. $P_\Phi(k)$ has dimensions of k^{-3} , so if we multiply $P_\Phi(k)$ by k^3 we can obtain a dimensionless quantity proportional to the variance Δ^2 :

$$\Delta^2(k) = \frac{k^3 P_\Phi(k)}{2\pi^2}. \quad (2.1.9)$$

Δ^2 indicates the clumpiness on a scale k^{-1} . When the combination $k^3 P_\Phi(k)$ (and also the variance) does not depend on k , the power spectrum is called scale invariant. Assuming a nearly scale-invariant power spectrum allows for a successful description of the fluctuations observed in the CMB, as can be seen by Figure 2.2

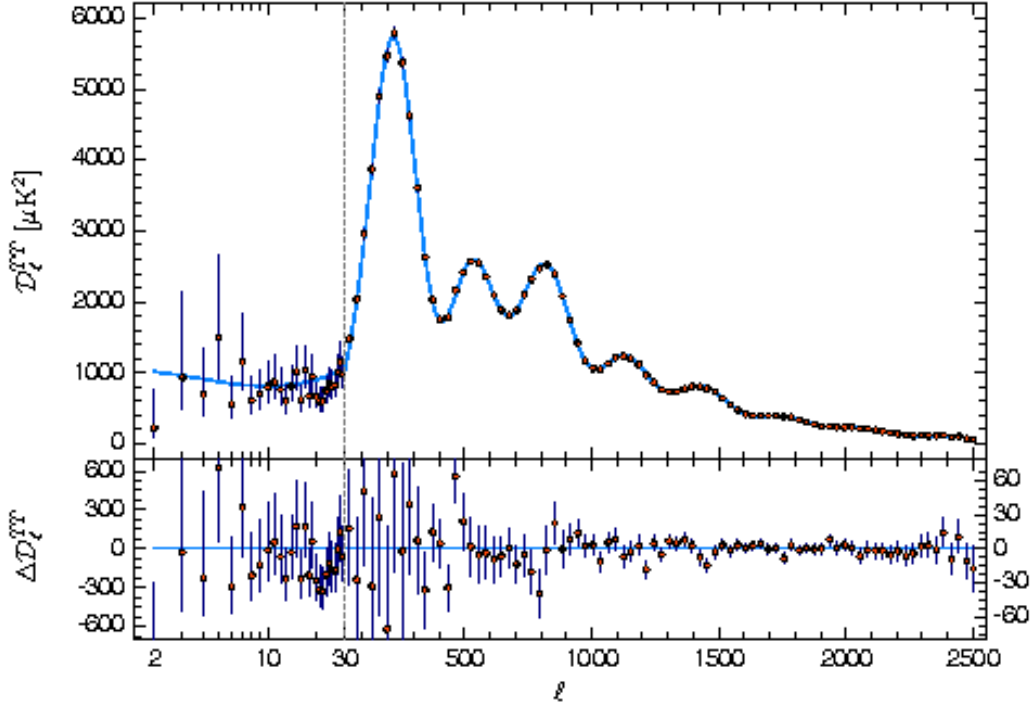


Figure 2.2 *Planck 2018 CMB anisotropies taken from [3].* The x-axis is multipole (large multipoles correspond to small angles) and the y-axis is the angular power spectrum $D_l^{TT}[\mu K^2]$, with red dots indicating the measurements and blue lines showing the best-fitting model. $\Delta D_l^{TT}[\mu K^2]$ indicates the difference between the best-fitting model and Planck measurements.

The most popular candidate responsible for the primordial fluctuations is the inflationary scenario, although other scenarios also can lead to a nearly scale-invariant primordial power spectrum.

2.2 Cosmic Strings

Cosmic strings are one-dimensional topological defects in space-time. A broad class of models that describe physics beyond the Standard Model of Particle Physics (SMPP) admits cosmic strings as solutions, which are regions of trapped energy density. Generally, theories that go beyond the Standard Model lead to phase transitions in the high energy regime. Cosmological probes offer an alternative possibility (with respect to modern parti-

cle colliders) to test the large energy scales needed to observe the effects of those theories since the high energy regime arises naturally during the very early universe.

The presence of cosmic strings is a generic property of many extensions of the SMPP. While in some models, cosmic strings can be produced during and at the end of inflation, such as [5], in many, they are produced during phase transitions after inflation or after early universe scenarios alternative to inflation [6]. It is also important to mention that superstring theory, one of the most studied proposals for a unified theory of all fundamental interactions inspires models beyond the standard model that contain cosmic strings (called cosmic superstrings in this context). Among the extensions that are not necessarily motivated by string theory is the class of Grand Unification Theories (GUTs), which unify the strong, weak, and electromagnetic forces into one single interaction. GUT theories assume that the SMPP forces were unified into a large gauge group during a regime of high energy density, such as the very early universe. Below a specific critical temperature, the gauge group is reduced to a product of subgroups due to a phase transition characterized by spontaneous symmetry breaking (SSB). Under certain conditions (see 2.2.21 below), the formation of linear topological defects is unavoidable during this transition.

Regardless of which specific description beyond the Standard Model holds, Kibble [7] found in 1976 that if a model of nature admits cosmic string solutions, they will necessarily form during the early universe. Both numerical simulations [8, 9] and analytic arguments [10] shows that after formation, a cosmic string scaling network will always persist. The network will consist of both long strings moving near the speed of light and also a distribution of loops. A scaling solution means that the statistical properties of the network will be the same at all times if the length scales are measured in units of the Hubble radius.

The tension μ of cosmic strings is determined by the energy scale η at which the string network forms [11], and is given by:

$$G\mu = \left(\frac{\eta}{m_{pl}}\right)^2, \quad (2.2.10)$$

where G is Newton's constant and m_{pl} is the Planck mass. μ is also the linear mass density of the string.

A simple example that illustrates the most important properties of cosmic strings is the Abelian Higgs model with a spontaneously broken $U(1)$ symmetry [12]. In the context of GUT theories, this is an over-simplistic realization with a $U(1)$ symmetry completely

breaking. This model still keeps the essential features of a generic symmetry breaking process that are interesting for cosmic string physics. The Lagrangian L of this model contains a gauge field A_μ of charge q (with respect to the $U(1)$ symmetry) and a complex Higgs field ϕ :

$$L = D_\mu \phi D^\mu \phi^* - \frac{1}{4} F_{\mu\nu} F^{\mu\nu} - \lambda(\phi \phi^* - \frac{\eta^2}{2})^2, \quad (2.2.11)$$

where

$$F_{\mu\nu} = \partial_\mu A_\nu - \partial_\nu A_\mu \quad (2.2.12)$$

$$D_\mu \phi = \partial_\mu \phi - iqA_\mu \phi. \quad (2.2.13)$$

It can be noted that the potential $V(\phi) = -\lambda(\phi \phi^* - \frac{\eta^2}{2})^2$ is minimized for the value of the modulus of the Higgs field given by $|\Phi|^2 = \frac{\eta^2}{2}$. Therefore the condition for minimum potential energy:

$$\phi = (\frac{\eta}{\sqrt{2}}) e^{i\theta} \quad (2.2.14)$$

provides conditions only for the modulus of the Higgs field and not for its phase θ , which in general will depend on the position $\theta = \theta(\vec{x})$. This phase needs to be single-valued, so the total change of θ around a closed path $\Delta\theta$ needs to be an integer multiple of 2π . Considering a path where $\Delta\theta = 2\pi$, and compressing it to a single point, $\Delta\theta$, cannot change continuously from 2π to 0. Therefore there must be a point inside the first path at which the phase is undefined, i.e., $\phi = 0$ (this is known as a false vacuum). The point at which the Higgs field is equal to zero is part of a tube-shaped region of false vacuum. Such a region needs to be a closed tube or an infinite tube. Otherwise, it would be possible to deform the path around the tube and contract it to a point without finding the false vacuum. This tube is the cosmic string.

The first approximate solution of the equations of motion of the Lagrangian (2.2.11) containing a cosmic string was found by Nielsen and Olesen [13]:

$$\phi = \frac{\eta}{\sqrt{2}} \left[1 - e^{-\frac{r}{r_1}} \right] e^{-i\theta} \quad (2.2.15)$$

$$A_\theta = \frac{\left[1 - e^{-\frac{r}{r_2}}\right]^2}{er}, \quad (2.2.16)$$

where a cylindrical coordinate system was used, with the string centered along the z-axis, and where r_1 and r_2 are $\propto \eta^{-1}$. The linear energy density of the cosmic string is given by equation 2.2.10 above.

Vilenkin [14] solved the Einstein equation for the metric of an infinite cosmic string along the z-axis. In terms of cylindrical coordinates, the result is:

$$ds^2 = dt^2 - dz^2 - dr^2 - (1 - 4G\mu)^2 r^2 d\theta^2. \quad (2.2.17)$$

By a coordinate transformation of the polar angle $\theta \rightarrow ((1 - 4G\mu)\theta)$ the metric becomes the Minkowski metric, which means that space perpendicular to a string is a cone. It is spatially flat away from the string core, but the polar angle can only vary between 0 and $e^{2\pi(1 - 4G\mu)}$. This fact indicates that the flat metric of a cosmic string has a deficit angle α given by

$$\alpha = 8\pi G\mu. \quad (2.2.18)$$

This result is known as the conical singularity, and it is responsible for the important gravitational effects caused by cosmic strings.

To explain in more detail the appearance of cosmic strings from GUT theories, consider a Lagrangian $L(A_\mu, \phi, \dots)$ containing a gauge field A_μ , a scalar field ϕ and possibly other fields. The Lagrangian is invariant under the action of some internal symmetry group G , which is broken spontaneously in one or several stages into a smaller symmetry group H . Usually H is the SMPP group $H = SU(3) \times SU(2) \times U(1)$. The Higgs field ϕ is responsible for the SSB by taking an expectation value that is not invariant under the full G , but under $H \subset G$. To accomplish this, the potential $V(\phi)$ of the Higgs field must have a global minimum at $\phi \neq 0$. The set of all field configurations M that minimize the potential is known as the vacuum manifold. Under the symmetry breaking $G \rightarrow H$ the vacuum manifold is characterized by:

$$M \cong G/H, \quad (2.2.19)$$

where the symbol \cong means an isomorphism.

The condition on M for the existence of a cosmic string solution needs the following concept of homotopy classes of M . Consider a set of maps $\psi : S^n \rightarrow M$, where S^n is the n -dimensional sphere. ψ_1 and ψ_2 are equivalent (symbolically $\psi_1 \approx \psi_2$) if \exists a one-parameter family of maps $\psi(t) : S^n \rightarrow M$, $t \in [0, 1]$ such that $\psi(0) = \psi_1$ and $\psi(1) = \psi_2$. That means it is possible to continuously deform ψ_1 into ψ_2 . The n 'th homotopy group of M , $\Pi_n(M)$ is the set of all homotopy classes of maps $S^n \rightarrow M$. As we saw above, if the vacuum manifold is equivalent to a circle, then cosmic solutions exist. Therefore the condition for the existence of cosmic strings is the following [15]:

$$\Pi_1(M) \neq I, \quad (2.2.20)$$

which means that the first homotopy group of M must be non-trivial. Now it is possible to show [11] (if it is connected and simply connected) that $\Pi_1(G/H) \cong \Pi_0(H)$. Therefore a simpler condition for the existence of cosmic strings follows:

$$\Pi_0(\tilde{H}) \neq I, \quad (2.2.21)$$

where the tilde symbol means \tilde{G} was taken, which is the universal covering group of G , defined as the embedding of any compact Lie group G in a simply connected \tilde{G} . The transformation $G \rightarrow \tilde{G}$ also applies to $H \rightarrow \tilde{H}$. Since $n = 0$ in the condition 2.2.21 , Π_0 counts the number of connected components of \tilde{H} . Therefore the complicated verification that $\Pi_1(M) \neq I$ reduces to the simple verification whether the H is connected or not.

One can illustrate the condition 2.2.21 with the previous example. The initial symmetry group was $G = U(1)$. Since the covering group for the multi-connected $U(1)$ is the simply connected real line $\tilde{G} = R$, H which was the identity become the set of translations by $2\pi n$, which are the integers: $\tilde{H} = Z$. Since Z is a disconnected set, cosmic string solutions will exist.

A realistic GUT model should contain a larger symmetry group that includes the standard model groups. The group $G = SO(10)$ is one well-known example, having a Higgs that spontaneously breaks the symmetry at an energy scale of approximately $10^{14} GeV$ leaving an unbroken $\tilde{H} = SU(3) \times SU(2) \times U(1) \times Z_2$ group, which excepting the Z_2 , contains the Standard Model group [11]. The presence of the disconnected component Z_2 guarantees

the existence of cosmic strings in this particular model.

The strings discussed so far are called local cosmic strings. The term local refers to the role played by the gauge field as a local symmetry. It is also possible to consider global strings, in which the gauge field A_μ is absent. In the local case, the gauge field compensates the phase gradients in the kinetic term, allowing then not to contribute to the energy of the string at large distances. In the absence of the gauge field, the kinetic term contributes to the energy density of the string, which is not exponentially suppressed outside the string core and leads to a logarithmic growing contribution to the mass per unit length of the string given by:

$$G\mu(r) = \left(\frac{\eta}{m_{pl}}\right)^2 \ln(r/\delta), \quad (2.2.22)$$

where r is a large distance cutoff (e.g. radius of a string loop, Hubble radius for an isolated long string) and δ is its width. Also, the deficit angle will be modified. At a distance r from the string core, it is:

$$\alpha(r) = 8\pi G\mu(r), \quad (2.2.23)$$

where $\mu(r)$ is given by 2.2.22 above. As for local strong, the global strings will also achieve a scaling network. One example of an extension of the SMPP which contains global strings (see [16, 17]) is the axion model, which was proposed as a solution to the strong CP problem. Global cosmic strings appear because the axion breaks a global Peccei-Quinn $U(1)$ symmetry.

As already mentioned, superstring theory also contains cosmic strings. The first proposal [17] suggested that $O(32)$ and $E_8 \times E_8$ string theories might have stable vortex lines, but they required an energy density close to the Planck mass, which is ruled out by observations. Otherwise, they would generate large unseen perturbations. Since then, more one-dimensional objects were found to exist in superstring theory: D-strings, high-dimensional D-, NS-, M-branes that have components which are wrapped along compact cycles with only one non-compact remaining dimension. There is an inflationary model which gives rise to cosmic strings, called brane-inflation [5], that considers a brane anti-brane pair annihilation. Each brane has a $U(1)$ symmetry (with opposite charges), with the daughter brane having a remaining $U(1)$ symmetry. The brane annihilation produces stable cosmic strings, referred to as cosmic superstrings [18].

2.3 Cosmic String network formation and evolution

The Kibble mechanism [7] ensures that if a theory of nature admits cosmic strings solutions, strings will be produced during a phase transition in the early universe. To illustrate this, consider the Abelian-Higgs model discussed above where temperature effects were not considered. But since the temperature was very high in the early universe, its effect has to be taken into account. A simple way to insert temperature effects to the Abelian-Higgs model is to add an interaction between ϕ and another scalar field ψ which is in equilibrium with the thermal bath. Adding a interaction of the form $1/2\tilde{\lambda}\phi^2\psi^2$ to the Lagrangian presented in 2.2.11 results in :

$$L = D_\mu\phi D^\mu\phi^* - \frac{1}{4}F_{\mu\nu}F^{\mu\nu} - \lambda(\phi\phi^* - \frac{\eta^2}{2})^2 - \frac{1}{2}\lambda'\phi^2\psi^2. \quad (2.3.24)$$

The expectation value for ψ^2 in thermal equilibrium is $\langle\psi^2\rangle_T \approx T^2$, allowing 2.3.24 to be rewritten as:

$$L = D_\mu\phi D^\mu\phi^* - \frac{1}{4}F_{\mu\nu}F^{\mu\nu} - V_T(\phi, T) \quad (2.3.25)$$

where $V_T(\phi, T)$ is the finite temperature effective potential:

$$V_T(\phi, T) = \lambda\phi^4 + m^2(T)\phi^2 + \lambda\frac{\eta^4}{4} \quad (2.3.26)$$

and

$$m(t) = \tilde{\lambda}T^2 - \lambda\eta^2 \quad (2.3.27)$$

is the effective mass. Above the critical temperature $T_c = \eta\sqrt{\lambda/\tilde{\lambda}}$ the mass term is positive, and the potential has a minimum at $\phi = 0$. On the other hand, if $T < T_c$ the Higgs field acquires a vacuum expectation value that fixes ϕ to $|\phi|^2 = (1/2)|m(T)|/\lambda$ and symmetry breaking occurs. This yields a non-zero value for the modulus for the Higgs field but does not fix its phase, which can take any value. By causality, the phase of the Higgs field in different Hubble volumes must be uncorrelated. Therefore, there is a probability of order one that given a circle of the size of the Hubble radius, the phase of the Higgs field will change by a non-zero multiple of 2π . The consequence is that there will exist a point on every surface that has this circle as a boundary such that this field is zero, with the phase undefined there. The cosmic string will be the collection of these points. Kibble's mechanism ensures that after the phase transition, the universe will be filled with

cosmic strings having a correlation length approximately equal to the Hubble radius: $\xi \approx t$. Besides this, numerical simulations [19] shows that about 80% of the energy of the network will be in infinite strings and the remaining 20% will be in cosmic string loops.

After they form, cosmic strings achieve a scaling network. The main reason for this is that cosmic strings exchange ends when they collide. In the picture 2.3 bellow, two cosmic strings collide in two points and exchange ends, resulting in a loop. The same process occurs when a cosmic string intersects itself, also producing a loop. After the loop forms, it releases energy through a radiation channel. To see that the cosmic string network reaches a scaling solution, consider the correlation length of the network at a time t , $\xi(t)$. The correlation length measures the mean distance between cosmic strings. If this distance is much smaller than the Hubble radius ($\xi(t) \ll t$), then there will be a lot of cosmic string intersections and loops will be produced copiously and evaporate, increasing $\xi(t)/t$. On the other hand, if $\xi(t) > t$, the correlation length will not change, because no physical process can occur between regions that are not causally connected. This will decreases $\xi(t)/t$, rendering $\xi(t) \approx t$ as a stable solution. Figure 2.4 shows a sketch of the string scaling solution.

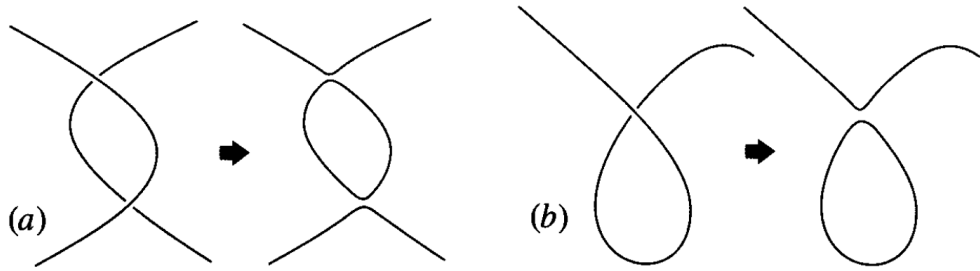


Figure 2.3 Visualization of the exchanging end mechanism that allows loop production. Picture taken from [11].

This analytical argument presented above for the scaling network solution is corroborated by numerical simulations, which also indicate that the long strings will have velocities near the speed of light. There are two ways of numerically studying the cosmic string dynamics. In one of them, called Nambu-Goto simulation, the thickness of the string is set to zero [9] and the string worldsheet dynamics is studied using the equations of motion derived from the Nambu-Goto action, with the string crossing prescription imposed by hand. In the other type, called field-theory simulations, the field equations of motion de-

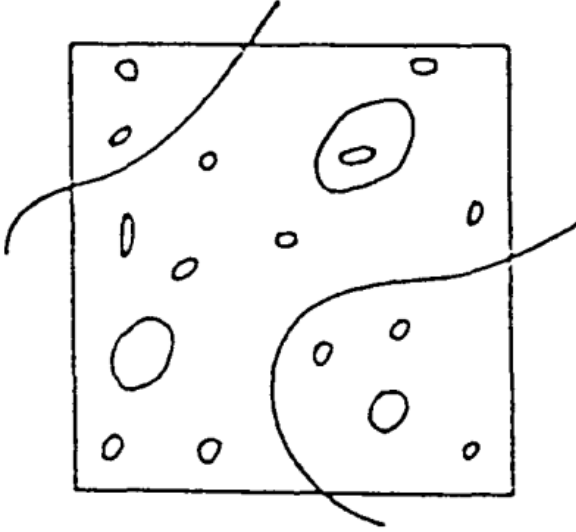


Figure 2.4 Sketch of the scaling distribution of a cosmic string network, consisting of $O(1)$ long strings and a distribution of loops. At an arbitrary time, all pictures will look similar if their size is give by the Hubble radius. Picture taken from [15].

rived from the abelian-Higgs model are solved numerically [20]. Although in this case it is possible to resolve the thickness of the cosmic string, there are difficulties treating the very different scales of the problem, because the cosmic string thickness is about 100 order of magnitude smaller than the correlation length at late cosmological times. Both methods agree concerning the scaling network evolution, but they produce different distributions for the loops, with the Nambu-Goto simulations containing more loops than the field-theory simulations. Another critical difference is that in Nambu-Goto simulations, the energy of the string network goes into gravitational radiation, whereas in the field theory simulations the energy of the cosmic string goes to particle production.

2.4 Robust Observational Constraint on Cosmic Strings

The initial interest in cosmic string appeared with the idea that they could be the leading candidates to seed fluctuations [21]. However, this idea was proven wrong. The features observed in the fluctuations of the CMB temperature cannot be explained only by cosmic strings. If cosmic string exists, they cannot be responsible for more than 5% of the observed

fluctuations, having only a subdominant contribution. The reason for this is because the fluctuations provided by cosmic strings are incoherent and active, whereas the observations indicate that the dominant source of fluctuations is the opposite (coherent and passive) [22]. Fluctuations generated by inflation are called “passive” because once inflation ends, the fluctuations will evolve without additional sources of fluctuations, contrary to the fluctuations caused by topological defects, which will always source them [23] (that is why they are called “active”). Also, fluctuations generated by cosmic strings are “incoherent” in the sense that the strong non-linear dynamics will force all correlations in different times to zero, as opposed to the inflationary case.

Inflationary models predict an ensemble of pressure waves in the photon-baryon fluid that are phase-focused, that is, the entire ensemble $|\vec{k}| = k$ reaches an amplitude equal to zero at the same time. Waves with different wavenumbers k pass through the moments of zero amplitude at different times, giving to the CMB the oscillatory features (called acoustic peaks) that can be seen in 2.2. On the other hand, cosmic strings will not contain BAO features in the CMB, because the random nature of the pressure waves will destroy the phase focusing [24]. In fact, observing the BAO imposes the most robust constraint on cosmic strings [25, 26]:

$$G\mu < 1.3 \times 10^{-7}. \quad (2.4.28)$$

where the quoted constraint is obtained from an analysis of Planck data, and the modeled cosmic string effects come from Nambu-Gotto simulations. For field theory simulation, the constraint in [26] is $G\mu < 3.0 \times 10^{-7}$.

There are also stronger limits which come from pulsar timing surveys [112], but these depend on assumptions about the distribution of string loops which are not universally accepted.

By studying the observational aspects of cosmic strings, two possibilities can happen. One is that a cosmic string is observed, which would be a significant achievement in probing particle physics models beyond the SMPP. Another option is not to find cosmic strings, which may lower the bound on the cosmic string tension, thus ruling out more classes of particle physics models.

Chapter 3

Cosmic string wakes

This chapter will be dedicated to showing how cosmic strings create a wake, changing the distribution of matter behind them.

3.1 Wake formation

A cosmic string wake is a planar overdense region that forms behind a long cosmic string as it passes by the matted distribution [27, 28]. A long cosmic string produces a wake due to two of its features: the missing angle (see 2.2.18) and the fact that it has a non-zero velocity v_s .

Recall that the plane perpendicular to a long cosmic string will have a missing angle giving by the following expression:

$$\alpha = 8\pi G\mu. \quad (3.1.1)$$

Also, remember that numerical simulations indicate that long cosmic strings have velocities v_s near the speed of light. This introduces velocity perturbations δv given by:

$$\delta v = 4\pi\gamma_s v_s G\mu, \quad (3.1.2)$$

where γ_s is the Lorentz factor associated with v_s . To see this, consider two test particles at rest and near each other and the long cosmic string passing between the two. In the frame in which the long string is at rest, the two dark matter particles will meet at some point behind the string, as the two figures 3.1 and 3.2 below indicate.

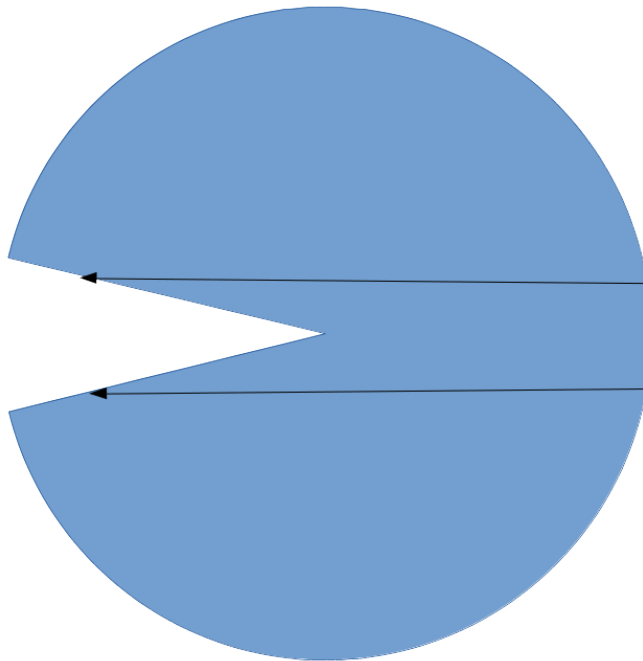


Figure 3.1 The plane perpendicular to a long string has a missing angle with two test particles meeting behind the string, in the frame in which the long cosmic string is at rest

Going back to the previous frame (here is the origin of the Lorentz factor in 3.1.2) an equivalent situation is obtained, where the two dark matter particles initially at rest receive a velocity kick towards the plane behind the string as soon as the string passes between the two.

Repeating the same line of thought to many test particles results in having two times more particles behind the long cosmic string after it passes through the matter distribution, as can be viewed in the following figure 3.3.

This leads to an overdense wedge-shaped region, which is the wake of the cosmic string. At a time of wake formation t_f , the string length is given by $c_1 t_f$, where c_1 is a constant of the order of unity and t_f is roughly the Hubble radius. Since the string has a velocity v_s in the normal direction of the string, the depth of the wake is given by $t_f v_s \gamma_s$. The width is much smaller, given by the deficit angle times the average depth: $4\pi G \mu t_f v_c \gamma_c$. So a wake

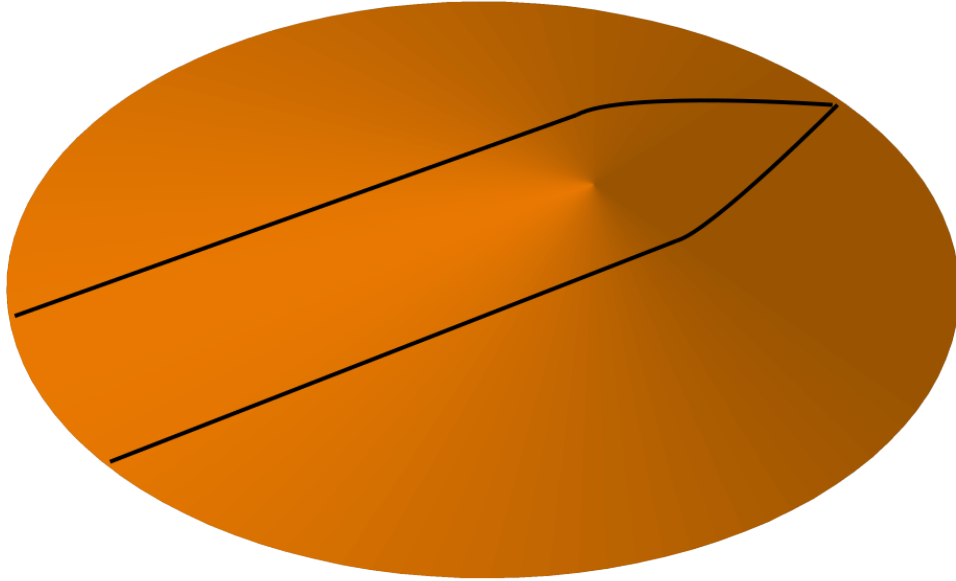


Figure 3.2 This is an equivalent visualization of the space perpendicular to a long string with two test particles meeting behind the string, in the frame in which the long cosmic string is at rest

generated by a cosmic strings at a time t_f has dimensions given by:

$$c_1 t_f \times t_f v_s \gamma_s \times 4\pi G \mu t_f v_s \gamma_s. \quad (3.1.3)$$

Wakes of cosmic strings produce non-linear density fluctuations at arbitrary early times, but perturbations can only grow after the time of equal matter and radiation energy density.

3.2 Wake evolution

The wake evolution is studied analytically by using the Zel'dovich approximation [29], which is applied to the wake dynamics to provide the wake thickness as a function of time [30, 31]. To obtain the evolution of the wake thickness, consider a test particle near the

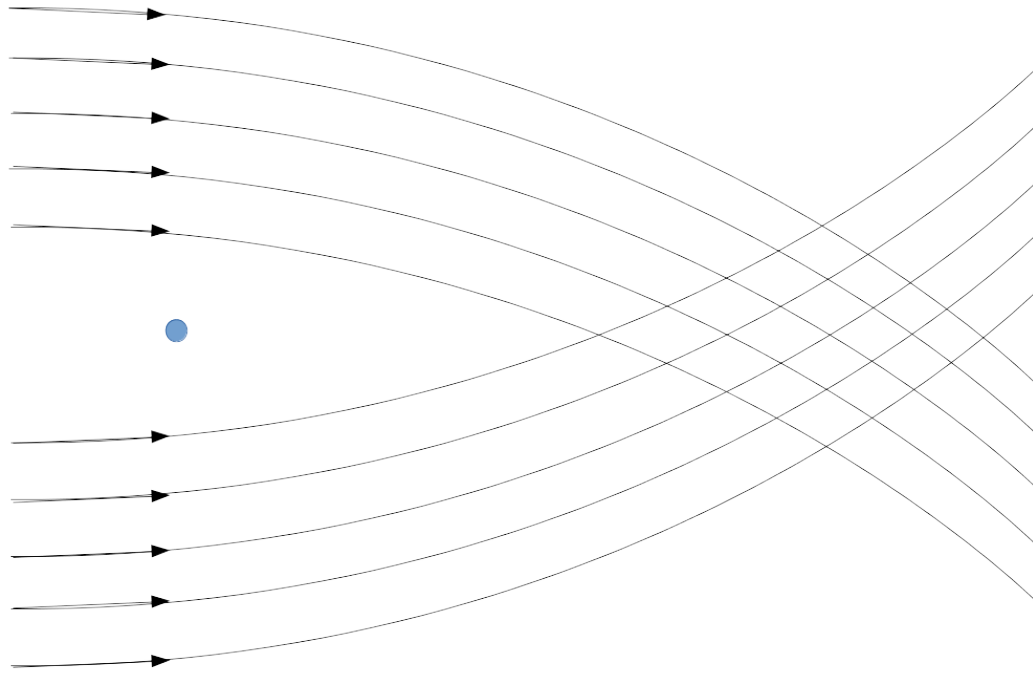


Figure 3.3 This is a visualization of the space perpendicular to a long string with a set of test particles meeting behind the string, in the frame in which the long cosmic string is at rest

wake. Its physical distance h to the wake (as depicted by figure 3.4) is the scale factor $a(t)$ times the initial comoving distance q to the wake minus a comoving displacement ψ , which depends on the initial position:

$$h(q, t) = a(t)[q - \psi(q, t)]. \quad (3.2.4)$$

The particle has no displacement initially (at time t_i):

$$\psi(t_i) = 0. \quad (3.2.5)$$

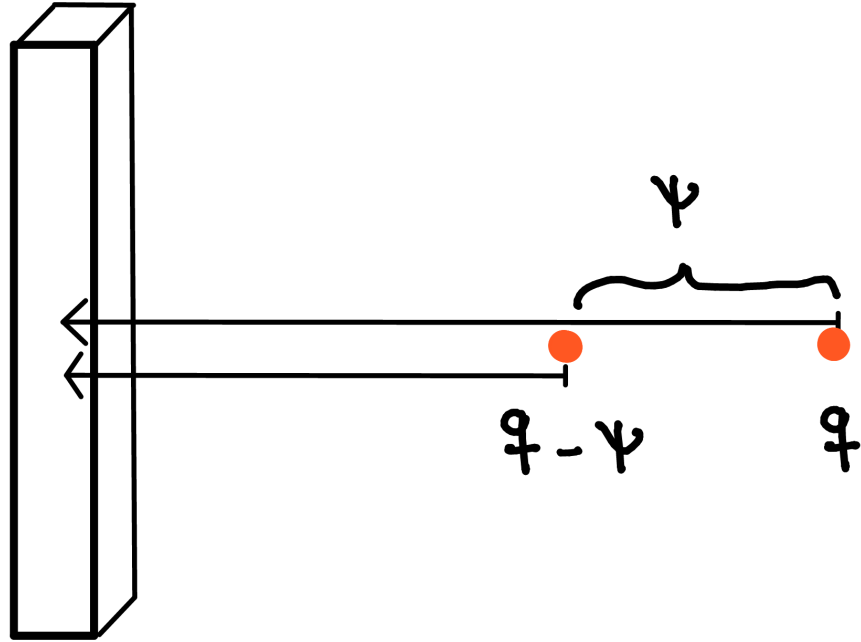


Figure 3.4 This figure depicts the displacement of a test particle represented by the red dot in terms of its comoving distance to the center of the wake. q is its initial comoving distance and ψ is its comoving displacement

It also receives a velocity kick induced by 3.1.2 (here shown in comoving coordinates):

$$\dot{\psi}(t_i) = \frac{4\pi\gamma_s v_s G\mu}{a} \quad (3.2.6)$$

The dynamics is set by Newton's law

$$\ddot{h} = -\frac{\partial\Phi}{\partial h} \quad (3.2.7)$$

and the Poisson equation of motion:

$$\frac{\partial^2\Phi}{\partial h^2} = 4\pi G[\rho + \sigma\delta(h)], \quad (3.2.8)$$

where Φ is the gravitational potential, G is Newton's constant, ρ is the volume energy

density, $\delta(h)$ enforces the extra surface density σ to be at $h = 0$. The extra surface density σ induced by the wake is given by:

$$\sigma(t) = 4\pi G \mu t_i v_s \gamma_s \left(\frac{t}{t_i}\right)^{\frac{2}{3}} \rho(t), \quad (3.2.9)$$

which is the physical initial wake thickness $4\pi G \mu t_i v_s \gamma_s \left(\frac{t}{t_i}\right)^{\frac{2}{3}}$ at time $t \geq t_i$ times the energy density $\rho(t)$. The linear version of equations 3.2.7 and 3.2.8 results in:

$$\ddot{\psi} + \frac{4}{3t} \dot{\psi} - \frac{2}{3t^2} \psi = 0, \quad (3.2.10)$$

This equation has the following growing mode solution:

$$\psi(t) = \frac{12\pi}{5} G \mu v_s \gamma_s t_i \left(\frac{t}{t_i}\right)^{\frac{2}{3}}. \quad (3.2.11)$$

Plugging this solution back into 3.2.6 an interesting scenario appears: initially the physical distance from the test particle to the wake starts to increase due to the Hubble expansion, but eventually the growing mode dominates and the particle starts to move towards the wake. The wake thickness is now defined as the length for which all particles within it are moving towards the wake. The point of which the transition occurs is called turn around point given by the condition that the time derivative of h vanishes $\dot{h} = 0$. This condition implies that a test particle that is turning around at time t was initially at the following initial comoving position q_{ta} :

$$q_{ta} = \frac{24\pi}{5} G \mu v_s \gamma_s t_0 \frac{\sqrt{1+z_i}}{(1+z)}. \quad (3.2.12)$$

When comparing this initial position with the displacement induced by the wake, the result is that at the turning around point the test particle is at half the comoving distance where it started:

$$\psi(q_{ta}, t) = \frac{1}{2} q_{ta}. \quad (3.2.13)$$

This means that when the test particle turns around, the wake has two times the average density, therefore this property, which was true initially is maintained by the wake evolution.

The wake thickness $d(t)$ will include the distance between particles on both sides of the

wake that are turning around at time t :

$$d(t) = \frac{24\pi}{5} G \mu v_s \gamma_s t_0 \frac{\sqrt{1+z_i}}{(1+z)}. \quad (3.2.14)$$

After formation, the planar dimensions of the wake increase with the Hubble flow (they are fixed in comoving coordinates). The wake thickness increases because the wake starts to accrete matter, and grows as the scale factor in comoving coordinates. The equation above also confirms the intuition that wakes formed earlier (higher redshift z_i) are thicker. For wakes formed at the time of matter-radiation equality, the comoving planar dimension of the wake is $\approx 100 Mpc$, and the thickness is $\approx 0.1 a Mpc$ in comoving coordinates if the cosmic string has a tension given by the current bound 2.4.28

The linear approximation developed in the previous section breaks down when the scale corresponding to the wake thickness enters the non-linear regime in pure ΛCDM cosmology. There is a necessity for a description of the wake evolution during these regimes that goes beyond the linear approximation. Early on the wake is very distinguishable from the rest of the matter distribution, but as time passes the ΛCDM fluctuations start to become more pronounced than the fluctuations caused by the wake, causing fragmentation of the wake plane.

The criteria for wake disruption was studied in [32] (see also chapter 5). Two different criteria were considered, called “local” and “global” disruption conditions. The local wake disruption condition uses a box of the size of the wake thickness and studies the standard deviation of the density contrast in this region, given by ΛCDM cosmology, to look whether it overcomes the wake density contrast. Since there are fluctuations of the order one in the wake, the local wake disruption criterium is the following: if the standard deviation on a cube of side d (given by the wake thickness 3.2.14) is of order one, then the wake is locally disrupted. For the current bound on the cosmic string tension, the local criteria give a disruption at $z \approx 8$.

The local criterion does not take into account the global volume of the wake, so a natural extension would be to consider an anisotropic box with dimensions given by the whole wake. The global disruption criterion reads the following: if the standard deviation for a box with wake dimensions is of order one, then the wake is globally disrupted. This criterion yields the result that although the wake gets disrupted locally, its global signal remains present at all times, independently of the cosmic string tension.

Chapter 4

Probing particle physics beyond the Standard Model with Cosmic Strings

In section 2.4 of chapter 2 the most robust current constraint on the cosmic string parameter was presented. It was based on the difference between attributes introduced by cosmic strings in the angular power spectrum of the CMB and the ones observed. It will be shown that cosmic strings leave distinct features in position space as well, and this information has the potential to constrain the cosmic string tension parameter even more.

4.1 Signature of CS in the CMB temperature and polarization maps in position space

Cosmic strings predict non-Gaussian temperature anisotropies because photons passing on different sides of a long string with velocity v_s reach the observer with the following Doppler shift:

$$\frac{\delta T}{T} = 8\pi\gamma_s v_s G\mu, \quad (4.1.1)$$

where γ_s is the gamma factor associated with v_s . The observer will detect a discontinuous jump on the CMB temperature map given by δT above. This is called the Kaiser-Stebbins (KS) effect [33], and is illustrated by figure 4.1 below.

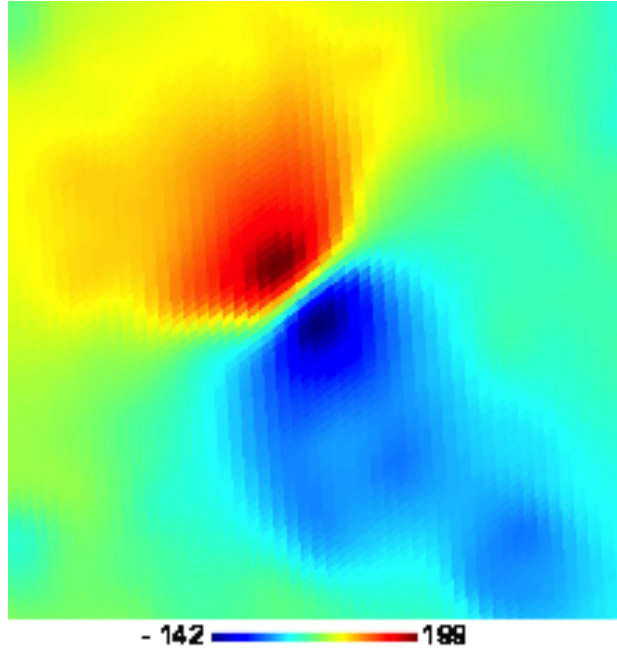


Figure 4.1 This is a visualization of the Kaiser-Stebbins effect in the temperature (in μK units) CMB maps (figure taken from [26]).

4.1.1 Signature of wakes in the CMB polarization maps

CMB photons travelling to us acquire polarization when they transverse regions of inhomogeneous density. The polarization of a photon depends on the direction of its electric field [34]. Given the electric field of monochromatic radiation

$$\vec{E} = (\vec{\epsilon}_1 E_1 + \vec{\epsilon}_2 E_2) e^{i\vec{k}\cdot\vec{x} - iwt}, \quad (4.1.2)$$

the polarization vector can be decomposed in two perpendicular vectors given by $\vec{\epsilon}_1$ and $\vec{\epsilon}_2$. One way to characterize the polarization is using the Stokes parameters I, Q, U, V , defined by

$$I = |\vec{\epsilon}_1 \cdot \vec{E}|^2 + |\vec{\epsilon}_2 \cdot \vec{E}|^2 \quad Q = |\vec{\epsilon}_1 \cdot \vec{E}|^2 - |\vec{\epsilon}_2 \cdot \vec{E}|^2 \quad (4.1.3)$$

$$U = 2Re[(\vec{\epsilon}_1 \cdot \vec{E})^*(\vec{\epsilon}_2 \cdot \vec{E})] \quad V = 2Im[(\vec{\epsilon}_1 \cdot \vec{E})^*(\vec{\epsilon}_2 \cdot \vec{E})]. \quad (4.1.4)$$

The amplitude of the polarization P is given by $P = \sqrt{Q^2 + U^2}$.

In addition to the Stokes parameters, another way to characterize the polarization is in terms of the E and B modes, which are components of the polarization vector with the property they have null divergence and null curl, respectively. The inflation model predicts that the contribution to the polarization is more significant for E mode than for B mode. The latter is produced only by gravitational waves. An accurate observation of the polarization spectrum of the B modes can test whether these were produced by inflation or by an effect of string gas cosmology [22], for example. On the other hand, disturbances generated by wakes of cosmic strings contribute equally to the two modes [36].

If the initially unpolarized CMB radiation encounters free electrons with a quadrupole anisotropy, then the resulting Thomson scattering will lead to polarization. The magnitude of the polarization is given by

$$P \cong \frac{1}{10} \left(\frac{3}{4\pi} \right)^{\frac{1}{2}} \tau_T Q \quad (4.1.5)$$

where τ_T is the optical depth and depends on the Thomson cross section σ_T and the integral of the density of free electrons $n_e(t, t_i)$ along the geodesic traveled by the photon:

$$\tau_T = \sigma_T \int n_e(\chi) d\chi. \quad (4.1.6)$$

For wakes formed after recombination $t_i > t_{rec}$, the baryonic content has a quadrupole anisotropy and can ionize the gas. Thus, photons passing through this gas suffer Thomson scattering and acquire polarization [36]. The initial density of free electrons in the wake is $n(t, t_i) \approx f \rho_b(t_i) m_p^{-1}$ (where f is the fraction of free electrons and m_p is the proton mass). For $t > t_i$, the density changes according to the inverse of the volume ($n \propto a^{-3}$) and therefore

$$n_e(t, t_i) = f \rho_b(t_i) m_p^{-1} \left(\frac{z(t) + 1}{z(t_i) + 1} \right)^3. \quad (4.1.7)$$

The integral of (4.1.6) results in

$$\tau_T = 2 \rho_T n_e(t, t_i) (z(t) + 1) h(t, t_i). \quad (4.1.8)$$

Using the value of h from (3.2.4), (3.2.11) and (3.2.12) yields

$$\frac{P}{Q} \cong \frac{24\pi}{25} \left(\frac{3}{4\pi} \right)^{\frac{1}{2}} \sigma_T f G \mu v \gamma \Omega_b \rho(t_0) m_p^{-1} t_0 (z(t) + 1)^2 (z(t_i) + 1)^{\frac{1}{2}}. \quad (4.1.9)$$

The polarization signal in position space of the CMB produced by a wake will be very specific: it will be a rectangle in the sky with extra polarization in the same direction with the following comoving dimensions:

$$c_1 t_i(z(t_i) + 1) \times v\gamma t_i(z(t_i) + 1). \quad (4.1.10)$$

4.2 Signature of wakes in the 21 cm hydrogen transition line

The 21 cm radiation is emitted (or absorbed) by the hydrogen atoms, which make up the bulk of the baryonic matter, when the proton and electron exchange among themselves their respective spins directions. The background radiation temperature T_γ passing through a cloud of hydrogen with a spin temperature T_S and optical depth τ_ν will emerge with a temperature [37] [38]

$$T_b = T_S(1 - e^{-\tau_\nu}) + T_\gamma e^{-\tau_\nu}, \quad (4.2.11)$$

where the spin temperature gives the fraction of hydrogen in the excited state and is implicitly defined by the equation

$$\frac{n_1}{n_2} = 3e^{\frac{-T_*}{T_S}}, \quad (4.2.12)$$

where n_1 and n_2 are the hydrogen densities in the states 1 and 2, corresponding to this hyperfine transition and $T_* = \frac{E_{12}}{k_b}$ is the energy difference between these states divided by the Boltzmann constant.

What is measured in observations is the difference in brightness temperature between the CMB and a cloud of hydrogen gas. This difference is given by

$$\delta T_b(\nu) = \frac{T_b(\nu) - T_\gamma(\nu)}{1+z} \cong \frac{T_S(\nu) - T_\gamma(\nu)}{1+z} \tau_\nu, \quad (4.2.13)$$

where the optical depth is given by

$$\tau_\nu = \int dS \alpha_\nu, \quad (4.2.14)$$

where α_ν is the absorption coefficient. The spin temperature can also be expressed in terms of the wake gas temperature T_K , of the incident photon temperature T_γ and the collision

coefficient x_c , which determines the scattering rate between hydrogen atoms and electrons:

$$T_S = \frac{1 + x_c}{1 + x_c \frac{T_\gamma}{T_K}}. \quad (4.2.15)$$

Inserting (4.2.15) in (4.2.12) results in

$$\delta T_b(\nu) \approx T_S \frac{x_c}{1 + x_c} \left(1 - \frac{T_\gamma}{T_K}\right) \tau_\nu (1 + z)^{-1}. \quad (4.2.16)$$

The optical depth of the hydrogen cloud is given by

$$\tau_\nu = \frac{3c^2 A_{10}}{4\nu^2} \left(\frac{\hbar\nu_{10}}{k_B T_S}\right) \frac{N_{HI}}{4} \phi(\nu). \quad (4.2.17)$$

where N_{HI} is the column density of hydrogen, and the term $\phi(\nu)$ is due to enlargement of the emission line.

In the case of a wake, the column density equals the density of hydrogen of the wake n_{HI}^{wake} times the length of the light ray passing through the wake, given by the wake width w and the angle θ that it makes with the vertical:

$$N_{HI} = \frac{2n_{HI}^{rastro} w}{\cos\theta} \quad (4.2.18)$$

Considering a point of the wake where the photons come in at an angle that is not orthogonal to the plane of the wake, it results that, relative the photon emitted in the center of the path, the emitted photons from the highest point and lowest generate a relative Doppler effect:

$$\frac{\delta\nu}{\nu} = 2\sin(\theta)\tan(\theta) \frac{Hw}{c}. \quad (4.2.19)$$

Both the width w and the expansion rate H are evaluated at the time that the photons are emitted. By normalization of $\phi(\nu)$, it follows that

$$\phi(\nu) = \frac{1}{\delta\nu} \quad (4.2.20)$$

for $\nu \in (\nu_{10} - \frac{\delta\nu}{2}, \nu_{10} + \frac{\delta\nu}{2})$ and $\phi(\nu) = 0$ otherwise. The result is

$$\delta T_b(\nu) = 2 \frac{x_c}{1+x_c} \left(1 - \frac{T_\gamma}{T_K}\right) \frac{3c^3 A_{10} \hbar}{16 \nu_{10}^2 k_B H_0 \Omega_m^{\frac{1}{2}}} \quad (4.2.21)$$

$$\times n_{HI}^{bg}(t_0) \frac{n_{HI}^{rastro}(t_0)}{n_{HI}^{bg}(t_0)} (2\sin^2(\theta))^{-1} (1+z)^{\frac{1}{2}}. \quad (4.2.22)$$

For illustrative proposes, using the parameters

$$\begin{aligned} A_{10} &= 2.85 \times 10^{-15} s^{-1}, T_* = 0.068 K, H_0 = 73 km s^{-1} Mpc^{-1}, \\ \nu_{10} &= 1420 MHz, \Omega_b = 0.042, \Omega_m = 0.26, 2\sin^2(\theta) = 1, \\ T_K &= 20 K, G\mu = 0.310^{-6}, (v_c \gamma_c)^2 = \frac{1}{3}, \\ z_i &= 10^3, 1+z = 30, T_\gamma = 82 K, x_c = 0.16 \end{aligned} \quad (4.2.23)$$

results in an emission of

$$\delta T_b(\nu) \approx -160 mK. \quad (4.2.24)$$

The planar dimensions of the emission will be in the angular direction, and are given by:

$$c_1 t_i(z_i + 1) \times t_i v_c \gamma_c(z_i + 1) \quad (4.2.25)$$

In summary, a cosmic string wake lead to a three-dimensional wedge of extra absorption in 21 cm redshift maps of angular size [4.1.10](#) with frequency direction of [4.2.19](#) and amplitude [4.2.24](#).

4.3 Brief comments on methods of cosmic string detection in position space

The previous two sections were devoted to showing that cosmic strings produce distinct localized features in position space of either the CMB (in both temperature and polarization maps) or the 21 cm map of the distribution if neutral hydrogen. In this section, various strategies used to extract such position space signals will be shown. One can divide the detection methods into several categories: the Canny edge detection algorithm, which uses intensity gradients to find edges in images; Minkowski functionals, which are used to study the topology of d-dimensional bodies embedded in a D-dimensional Euclidean space (with

$D > d$); convolutional neural networks, which use artificial intelligence methods to find patterns in images; multiresolution representations, which are used to detect discontinuities in one to three-dimensional maps. Some extraction techniques combine two of the methods above.

The CANNY algorithm consists of various stages to detect the edges in images. The first step consists of filtering the data to eliminate point sources. The length scale of the Gaussian filter is a free parameter of the algorithm and should be smaller than the scale of interest of the problem, but high enough to eliminate most of the point sources. The second step involves computing the gradient vector of the Gaussian-filtered image. The third step looks for local maxima of the gradients. The next step involves a double threshold procedure, done by labeling the pixels with maximum gradient given below as “strong”, “weak” or “suppressed”, depending if the value of the gradient is higher than a high cutoff, in between the high and low cutoffs or lower than the lower cutoff, respectively. Finally, the algorithm produces a list of points belonging to edges. This algorithm has three free parameters that can be tuned to differentiate CMB maps with and without cosmic strings [39] (see also [40] for the algorithm applied to cosmic superstrings). A modified version of the algorithm is presented in [41], where it was found that the South Pole Telescope will be able to constrain the cosmic string parameter one order of magnitude lower than the current constraint from CMB temperature maps.

Minkowski functionals are used in cosmology to probe the topology of a three-dimensional distribution of matter, by discriminating the filamentary and wall-like structures in the universe [42]. It can also be applied to estimate in a model-independent way the non-Gaussianities of the Planck CMB maps [43]. The use of Minkowski functionals is motivated by Hadinger’s theorem, which states that for a convex body B embedded in a d -dimensional Euclidean space, there exist $D + 1$ functionals M_μ , $\mu = 1, \dots, d + 1$ on B satisfying certain natural conditions (motion invariance, additivity, and conditional continuity) that characterize the topology of B entirely. Minkowski functionals are particularly interesting for wake characterization since in three-dimensional Euclidean space, the second Minkowski functional measures the surface of the body B . The work pursued this approach in [44], where the authors consider the 21-cm signature of wakes in the distribution of neutral hydrogen. To define the body B in the temperature maps, they considered the body as enclosed by an iso-temperature surface. Therefore this analysis has one free parameter, which is the temperature used to construct the surfaces. The authors found that using

simulated Gaussian maps (matching the ΛCDM power spectrum) with wakes of cosmic strings it is possible to extract the wake presence for $G\mu = 5 \times 10^{-8}$, which corresponds to an improvement factor of 3 over the current robust constraint.

Machine learning applies a numerical algorithm that improves its performance at a given task based on experience [45]. The goal of machine learning algorithms is to predict a set of values \vec{y} from a set of numerical inputs \vec{x} . The experience is gained from a collection of N examples (X, Y^*) , where $X = \vec{x}_i$ and $Y^* = \vec{y}^*$, $i = 1,..N$ that could come from simulations or observations from the phenomena at interest. The performance is measured by comparing the predicted values of y with the true target values y^* . The simplest choice for performance evaluation is the squared error, $SE = \sum (y_i^* - y_i)^2$, which must be minimized. The algorithm “learns” when its performance has improved under the exposure to new experience. Recent advances in machine learning come from neural network methods which are widely used for pattern recognition. A deep neural network consists in a set of nested non-linear functions that are adjusted to predict data, meaning that the input values, \vec{x} receive a non-linear transformation at each layer of the network, with the final layer producing the guesses of the prediction, \vec{y} . Each layer has a given number (called width of the layer) of neurons, and the number of layers is called depth, with the intermediate layers called hidden layers. In image pattern recognition, usually neighboring pixels are correlated, and a convolutional network is designed to take this correlation into account. One example of cosmic string detection using artificial intelligence methods is in [46, 47], where the authors use deep convolutional neural networks to extract signals from cosmic strings in the CMB. The pattern recognized is the Kaiser-Stebbins effect on the temperature maps of the CMB. The authors find that noise-free CMB maps with ΛCDM plus cosmic strings can be distinguished from pure ΛCDM maps for $G\mu \leq 5 \times 10^{-9}$. Their analysis involved the use of 11 free parameters (called hyperparameters).

Another class of important analysis tools that are suitable for wake detection is generically called multiscale methods. “Sparse representations” also refers of the same group of methods. Those methods involve the decomposition of a signal (a map in a given dimension) into a complete series of basis functions. Like in the case of Fourier analysis, in a multiscale basis any signal can be described using the basis function, but unlike the Fourier analysis case, which has non-localized (in position space) basis functions, the multiscale basis functions are localized in position space and therefore are widely used to find discontinuities in a signal [48]. The discontinuities correspond to the highest coefficients in this

basis decomposition having a specific localization and scale. For cosmic string localization, one uses mostly three different kinds of sparse representations: wavelets, ridgelets, and curvelets, which are suitable for point, line and line segment detection, respectively (for 2d maps). For three dimensional maps, ridgelets are used for plane detection, with the size of the ridgelet basis vector being of the same order as the image size; and curvelets are used for the location of plane segments, with variable size. The “publications” part of this thesis (except the first paper therein) explores the use of ridgelets and curvelets for wake detection in the dark matter distribution [49–51]. These papers conclude that it is possible to locate a cosmic strings wake with tension $G\mu = 10^{-7}$ down to redshift of $z = 3$. Wavelets and curvelets can be applied to searches for cosmic strings in the CMB. [52] uses wavelet-bayesian inference to put constraints of $G\mu \leq 5 \times 10^{-7}$ for Nambu-Goto cosmic strings, including integrated Sachs-Wolfe effects. Additionally, [53] uses curvelets to put constraints of $G\mu \leq 1.4 \times 10^{-7}$ for CMB maps with SPT-3G specifications. The multiscale methods have one free parameter which is the scale that is being probed, which can be fixed to match the size of the effect in interest, therefore can be chosen in accordance to the string tension to be searched.

An exciting option for cosmic string detection in real space is to use a combination of the methods above. For example, in [54], a curvelet analysis followed by the Canny edge detection method is performed, resulting in a constraint $G\mu \leq 4.3 \times 10^{-10}$ on the cosmic string tension for noiseless maps and $G\mu \leq 1.2 \times 10^{-7}$ constraint for a CMB-S4 phase II experiment. Another example is found in [55], where a combination of curvelet and artificial intelligence techniques was applied to CMB maps to find $G\mu \leq 4.3 \times 10^{-10}$ constraint for noise-free maps and $G\mu \leq 3 \times 10^{-8}$ for a CMB S4-like maps.

Part II

Publications

Chapter 5

Disruption of Cosmic String Wakes by Gaussian Fluctuations

5.1 Introduction

Cosmic strings exist as solutions of the field equations in many particle physics models beyond the Standard Model. A sufficient criterion is that the vacuum manifold \mathcal{M} of the model (the space of field configurations which minimize the potential energy density) has non-vanishing first homotopy group $\Pi_1(\mathcal{M}) \neq 1$. Roughly speaking the condition is that the vacuum manifold has the topology of a circle. A simple causality argument [7] leads to the important conclusion that in models which admit cosmic string solutions, a network of such strings inevitably forms during the symmetry breaking phase transition in the early universe and survives to the present time (see [11, 15, 56] for reviews of the role of cosmic strings in cosmology). Cosmic strings carry energy and hence induce gravitational effects which can lead to signatures in cosmological observations. The strength of these effects is proportional to the string tension μ which in turn is given (up to a numerical constant) by η^2 , where η is the scale of symmetry breaking at which the strings are formed. Hence, searching for cosmic strings in cosmological observations is a way to probe particle physics beyond the *Standard Model* which is complementary to accelerator searches (which can only probe new physics at low energy scales)¹.

Based on analytical arguments [11, 15, 56] it is expected that the distribution of cosmic

¹See [57] for an elaboration on this theme.

strings will take on a “scaling solution” according to which the statistical properties of the distribution of strings are independent of time if all lengths are scaled to the Hubble radius $H^{-1}(t)$ (where $H(t)$ is the cosmic expansion rate at time t). The distribution of strings consists of a network of infinite strings with mean curvature radius and separation $c_1 t$ (where c_1 is a constant of order one whose precise value needs to be determined in numerical simulations)² and a set of string loops which are the remnants of intersections of long string segments. Numerical simulations [9, 58–64] have confirmed that the distribution of strings takes on a scaling solution.

String loops oscillate and gradually decay by emitting gravitational radiation. Long string segments moving through the plasma of the early universe will lead to nonlinear overdensities in the plane behind the moving string. These are called string *wakes* [27, 28, 65, 66]. Wakes are formed because the geometry of space perpendicular to a long string segment is conical with deficit angle

$$\alpha = 8\pi G\mu, \quad (5.1.1)$$

where G is Newton’s gravitational constant [14]. A string moving through the plasma with a velocity v perpendicular to the tangent vector of the string will lead to a velocity perturbation

$$\delta v = 4\pi G\mu v\gamma(v) \quad (5.1.2)$$

from both sides towards the plane behind the moving string (where $\gamma(v)$ is the relativistic gamma factor associated with the velocity v). In turn, this leads to a thin region behind the string with twice the background density, the *wake*. The dimensions of the wake behind a string at time t_i are

$$c_1 t_i \times v\gamma(v)t_i \times 4\pi G\mu v\gamma(v)t_i, \quad (5.1.3)$$

where the dimensions are length along the string, depth of the wake in the direction of string motion, and mean thickness of the wake, respectively. We will denote these dimensions by ψ_1 , ψ_2 and ψ_3 respectively when using comoving coordinates.

Cosmic string loops accrete matter in a roughly spherical way and give rise to density fluctuations which are hard to tell apart from fluctuations formed by other point sources. String wakes, on the other hand, give rise to signals with a clear geometrical signature,

²We are here considering a simplified “one-scale-model” of strings.

and have hence been the focus of a lot of recent work (see e.g. [22]). Long cosmic string segments produce line discontinuities in CMB (cosmic microwave background) temperature maps [33]. The contribution to the power spectrum of cosmological perturbations is scale-invariant [67–69]. However, the fluctuations are active and incoherent [23, 35, 70] and hence do not lead to acoustic oscillations in the CMB angular power spectrum anisotropies. At present, the angular CMB power spectrum, in fact, provides the most robust upper bounds on the string tension [25, 26] (see the introduction of [71] for a more detailed discussion on string tension limits as well as [72–80] for earlier studies)

$$G\mu < 1.3 \times 10^{-7}. \quad (5.1.4)$$

Hence, it follows that cosmic strings are only a sub-dominant component to the power spectrum of perturbations. The dominant contribution must be due to almost Gaussian and almost adiabatic fluctuations such as those produced by inflation (or by alternatives to inflation such as *String Gas Cosmology* [81, 82] or the *Matter Bounce* [83–85]).

Whereas overall cosmic strings are a sub-dominant component to structure formation, string wakes can nevertheless give rise to prominent signatures in position space maps. They give rise to a network of edges in CMB temperature maps across which the temperature jumps [33], rectangles in the sky with a specific CMB polarization signal (statistically equal E-mode and B-mode polarization with a polarization angle which is uniform over the rectangle and whose amplitude has a linear gradient [36]), and thin wedges of extra absorption or emission in 21cm redshift maps [37] (see also [44, 71, 86]). These features are most prominent at high redshifts when string wakes are already nonlinear fluctuations, but the Gaussian fluctuations are still in their linear regime. The cosmic string signals are also most easily visible in position space maps (e.g., with edge detection algorithms [39, 41, 87]), whereas the distinctive stringy features are washed out in power spectra (see e.g., [88]).

At early times, cosmic strings dominate the nonlinearities in the universe, the reason being that wakes are nonlinear perturbations beginning at the time they are formed, whereas Gaussian perturbations are linear at early times. At late times, however, the Gaussian fluctuations dominate the structure in the universe. Most of the nonlinearities at present are due to the Gaussian fluctuations. The question we wish to address in this paper is whether the string-induced inhomogeneities, which at early times are clearly visible, are

still observable as coherent objects in position space maps at later times (in particular times after reionization). Concretely, we wish to study whether string wakes will remain coherent or whether the Gaussian fluctuations disrupt them. This analysis is a crucial preliminary step towards identifying string signals at low redshifts, e.g., in 21cm redshift maps at redshifts comparable and smaller than the redshift of reionization, or in large-scale structure redshift surveys.

In this paper, we study various stability criteria for string wakes. We study the stability of a wake to local disruption and find the redshift above which a cosmic string wake remains locally intact, as a function of $G\mu$. However, even if Gaussian fluctuations cause the wake to be locally disrupted, a global signal may remain. We study a specific criterion which can be used to search for the signals of primordial wakes. This analysis shows that signals of string wakes remain from a global perspective to the present time. Interestingly, the signals can be identified independently of the value of $G\mu$, and do not depend on whether the wakes are shock-heated or diffuse (see [89] for a discussion of the difference between these two cases). Our various stability criteria will be relevant for developing robust observational strategies to search for string wakes.

In the following section, we give a brief review of cosmic string wakes. In Section 3, we present a local stability condition based on a *displacement condition*. In Section 4, we consider a local density contrast consideration. The resulting stability condition shows that wakes are locally disrupted by the Gaussian perturbations at a redshift lower than some critical redshift which depends on $G\mu$. In Section 5, we discuss a global stability condition which shows that wakes are visible up to the present time independent of the value of $G\mu$.

5.2 String Wake Review

Consider a string segment at time t_i moving with velocity v in the direction perpendicular to the string. This segment will produce an overdense region with twice the background density behind it whose dimensions are given by (5.1.3). Once formed, this wake will be stretched in the planar directions by the expansion of space, and it will grow in thickness by accreting matter from above and below. This accretion can be studied using the Zel'dovich approximation [29]. We will consider wakes produced at times $t_i > t_{eq}$, where t_{eq} is the time of equal matter and radiation. Those produced earlier cannot grow until t_{eq} , and they will hence be smaller.

The thickness of the wake at time $t > t_i$ is determined by computing the comoving distance $q_{nl}(t)$ of a shell of matter which is starting to collapse (“turning around”) onto the wake, i.e. for which

$$\dot{h}(q_{nl}(t), t) = 0, \quad (5.2.5)$$

where the physical height is given by

$$h(q, t) = a(t)[q - \psi(q, t)], \quad (5.2.6)$$

where $a(t)$ is the cosmological scale factor and $\psi(q, t)$ is the comoving displacement induced by the gravity of the wake. A standard calculation (see e.g. [30, 31, 36]) yields

$$q_{nl}(t, t_i) = (z(t) + 1)^{-1} \frac{24\pi}{5} v \gamma(v) G \mu(z(t_i) + 1)^{1/2} t_0, \quad (5.2.7)$$

where $z(t)$ is the cosmological redshift at time t and t_0 is the present time. At the turnaround $\psi(q_{nl}, t) = \frac{1}{2}q_{nl}$. After turnaround, the shell of baryonic matter virializes at a distance which is half of the turnaround radius, whereas the dark matter remains extended [90]. Hence, the physical height of the dark matter wake at time t is

$$h(t, t_i) = (z(t) + 1)^{-1} q_{nl}(t, t_i). \quad (5.2.8)$$

This is also the displacement which a particle experiences due to the wake if this particle ends up at the edge of the wake. We also denote the wake thickness in comoving coordinates by

$$\psi_3(z) = \frac{24\pi}{5} 10^{-7} (G\mu)_7 v \gamma(v) t_0 \frac{\sqrt{1+z}}{(1+z)}, \quad (5.2.9)$$

where $(G\mu)_7$ is the value of $G\mu$ in units of 10^{-7} .

The result (5.2.8) shows that the thickest wakes are those produced at the earliest times, namely $t_i = t_{eq}$. The thickness of a wake is obviously proportional to $G\mu$, and its comoving size grows linearly in the cosmological scale factor $a(t)$, as expected from linear cosmological perturbation theory.

5.3 Displacement Condition

In this section, we will obtain a stability condition which is based on displacements induced by primordial Gaussian fluctuations. For simplicity, we will restrict the analysis of this section to the matter-dominated period. In the next section, we will extend the validity range to include dark energy in the evolution of the growth factor. The wake plane (formed by the ψ_1 and ψ_2 lengths) can be subdivided into pieces of area $(\psi_3)^2$, where ψ_3 is the thickness of the wake in comoving coordinates. We will compute the displacement (in a direction perpendicular to the wake plane) which is coherent on this scale. In order to do this, we will integrate in time the fluctuation of the peculiar velocity field on the scale ψ_3 .

If S_{ψ_3} is the induced physical displacement, then

$$S_{\psi_3}(t) < h(t, t_i) \quad (5.3.10)$$

is a local displacement condition for the stability of the wake. To compute S_{ψ_3} consider the continuity equation

$$\dot{\delta} + \frac{1}{a} \vec{\nabla} \vec{v} = 0, \quad (5.3.11)$$

where δ is the relative matter density contrast and \vec{v} is the physical peculiar velocity field. Choosing a Fourier mode parallel to \vec{v} and taking the modulus of the Fourier transform of the above equation we obtain a relation between the amplitudes of the velocity and density contrast fields in momentum space:

$$|v_k(z)| = \frac{faH}{k} |\delta_k(z)| \quad (5.3.12)$$

where we used $\delta(z) = g(z)\delta(0)$, $g(z) = D(z)/D(0)$ and $D(z)$ is the growth factor [91]. For the matter dominated period, $g(z) = 1.29/(1+z)$ and the function $f(z) = \frac{a}{D(z)} \frac{dD(z)}{da}$ is approximately one.

The contribution to the standard deviation of the peculiar velocity field on a scale $L = \frac{2\pi}{k}$ at redshift z is denoted by $\Delta_v(k, z)$ and from the above equation we obtain

$$\Delta_v(k, z) = aH\left(\frac{L}{2\pi}\right)\Delta(k, z), \quad (5.3.13)$$

where

$$\Delta(k, z) \equiv \sqrt{\frac{k^3}{2\pi^2} P(k, z)} \quad (5.3.14)$$

is the dimensionless contribution to the standard deviation of the matter density fluctuations δ on a length scale corresponding to k , given the dimensional power spectrum $P(k, z)$ at redshift z . The induced physical displacement S_{ψ_3} is given by

$$S_L(z) = a \int_{z_i}^z a^{-1}(t') \Delta_v(k, z(t')) dt' \quad (5.3.15)$$

evaluated at $k = k_3$ where $k_3 = 2\pi/\psi_3$ is the wavenumber associated with the comoving thickness $\psi_3(z)$ of the wake. The integral will be dominated by the upper limit of integration, therefore

$$S_{\psi_3} = a \frac{\psi_3}{2\pi} \Delta(\psi_3(z), z), \quad (5.3.16)$$

and the displacement condition (5.3.10) becomes

$$\Delta(k_3(z), z) < 2\pi. \quad (5.3.17)$$

When the above equation holds, the coherent displacement in a region perpendicular to the wake plane will be smaller than the wake thickness ψ_3 . This displacement condition agrees to within one order of magnitude with the local delta condition of the next section and gives a physical interpretation to it. The above condition is valid during the matter-dominated period, but in the next section, this restriction will be extended to include the dark energy period.

5.4 Local Delta Condition

Another criterium for the stability of a wake can be obtained by demanding that the r.m.s. Gaussian mass fluctuations Δ on the scale $k_3(z)$ of the wake thickness is smaller than unity, i.e.

$$\Delta(k_3(z), z) < 1. \quad (5.4.18)$$

We call (5.4.18) the ‘‘Local Delta condition’’, which is stronger than (5.3.17). If this condition is satisfied, then the wake is locally stable. This condition can be justified by noticing that the matter density contrast δ in a volume within the wake fluctuates around one inside

the wake and around zero outside, so if the standard deviation σ of δ is of order one the wake matter signal will be lost.

The late time power spectrum is obtained by multiplying the primordial power spectrum by the square of a *transfer function* T , which comes from the non-trivial evolution of fluctuations on sub-Hubble scales. Specifically, for scales which enter the Hubble radius before the redshift z_{eq} of equal matter and radiation the fluctuations in matter on sub-Hubble scales grow only logarithmically since the universe is dominated by a smooth radiation fluid at these times and on these scales.

The late time power spectrum for a model with Gaussian fluctuations with fixed spectral index is obtained from ([4], page 184)

$$P(k, z) = 2\pi^2 \delta_H^2 \frac{k^n}{H_0^{n+3}} T^2(k) g^2(z) \quad (5.4.19)$$

where we use the expression given by [91] in the growth factor, which now includes dark energy, $T(k)$ is the transfer function, n is the scalar spectral index, and δ_H is the amplitude of Δ evaluated for a Fourier mode that corresponds to the Hubble scale. We choose a normalization that gives $\sigma_8 = 0.83$, where σ_8 is the rms fluctuation smoothed on a scale 8 Mpc/h using a top-hat window function. We use $n = 0.97$ and $\Omega_\Lambda = 0.7$. At this point, we will switch from natural units to units used conventionally in cosmology, namely Mpc for lengths and seconds for time. In these units $c = 9.6 \times 10^{-15}$ Mpc/s, and the expression on the right hand side of (5.4.19) has to be multiplied by c^{n+3} . We will also use $v\gamma(v) = c/\sqrt{3}$, $z_i = 1000$ and $t_0 = 4.35 \times 10^{17}$ s

The transfer function T from ([92] page 60) is used to obtain an analytic expression for $\Delta(k_3)$, which together with the approximation $(k_3(z))^{-0.0145} \approx 1$ gives

$$\Delta(k_3(z), z) = 0.607 \ln(1 + 22.7 k_3(z)) g(z). \quad (5.4.20)$$

This computation of Delta can now be applied to either condition (5.3.17) or (5.4.18). For example, using the “Local delta condition” (5.4.18), we find that the disruption redshift, the redshift when $\Delta(k_3(z), z) = 1$ depends only logarithmically on the wake thickness and hence on the value of $G\mu$. We see that wakes are stable to fairly late times.

In Figure 1 we plot the value of $\Delta(k_3(z), z)$ (vertical axis) as a function of redshift (horizontal axis) for the value $(G\mu)_7 = 1$ (black line) and $(G\mu)_7 = 10^{-4}$ (gray line). The

dashed horizontal line is $\Delta = 1$. We see that the wake is locally stable for z above approximately 6 in the case of $G\mu = 10^{-7}$ and for z above approximately 11 in the case of $G\mu = 10^{-11}$.

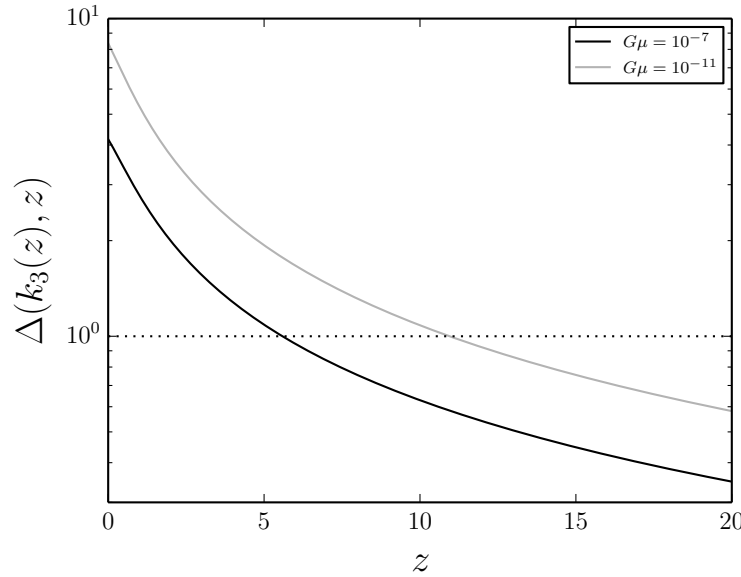


Figure 5.1 Plot of $\Delta(k_3(z), z)$ (vertical axis) as a function of redshift z (horizontal axis) for $G\mu = 10^{-7}$ (black line) and $G\mu = 10^{-11}$ (gray line).

In Figure 2 we plot (the solid black line) the value of $(G\mu)_7$ (vertical axis) for which the stability condition of a wake ceases to be satisfied at redshift z_d (horizontal axis). From this plot it follows that at $z_d = 20$ all wakes $(G\mu) \geq 10^{-14}$ are stable. The dashed horizontal line is $(G\mu)_7 = 1$, and we see that it intersects the solid black line (which gives the value of $G\mu$ below which the wake is disrupted) at $z \approx 6$, confirming the result of Figure 1. To obtain the value of $(G\mu)_7(z_d)$ such that the wake will be disrupted at redshift z_d (when the equality of (5.4.18) is satisfied) we use

$$k_3(z_d) = 113(1 + z_d)/(G\mu)_7 \quad (5.4.21)$$

in (5.4.20) to obtain

$$(G\mu)_7(z_d) = \frac{2565(1 + z_d)}{e^{1/0.607g(z)} - 1}. \quad (5.4.22)$$

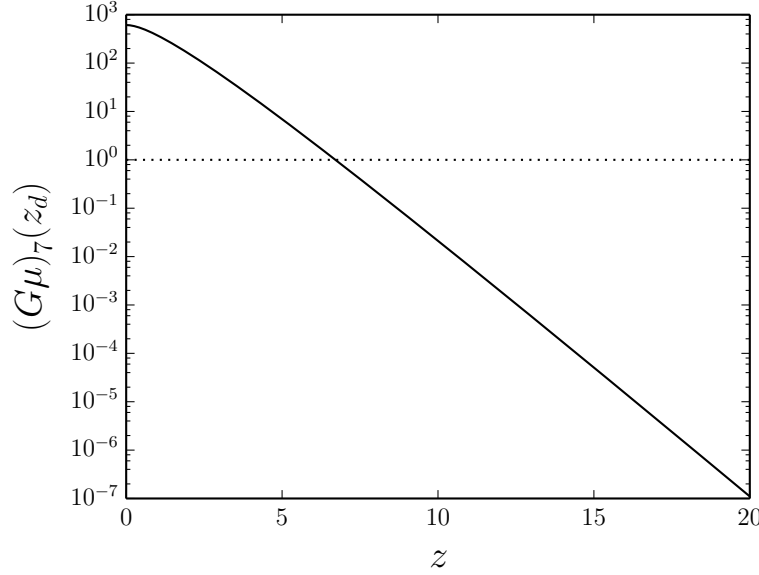


Figure 5.2 The value of $G\mu$ (vertical axis in units of 10^{-7}) above which the local Delta wake stability condition is satisfied as a function of redshift z (horizontal axis).

5.5 Global Sigma Condition

The local Delta stability condition studied in the previous section is a very strict condition. It is demanding that no section of the wake gets moved on a scale of the wake thickness. A less restrictive condition is to demand that the wake remains visible if we probe space with a filter which has the shape of the three dimensional, extended wake, i.e., which has two large dimensions given by the length and depth of the wake, respectively, and one small dimension given by the wake thickness. We call the resulting condition the “Global Sigma Condition”.

The variance of δ_w for a non-isotropic window function \tilde{W}_w is given by

$$\sigma_w^2 = \frac{g^2(z)}{(2\pi)^3} \int_{-\infty}^{\infty} \int_{-\infty}^{\infty} \int_{-\infty}^{\infty} dk_1 dk_2 dk_3 P(\|\vec{k}\|) \tilde{W}_w^2(\vec{k}, z) \quad (5.5.23)$$

where $g(z)$ is the growth factor and P is the power spectrum at the present time. Note that we are working in terms of comoving momenta. The “Global Sigma condition” then

is

$$\sigma_w < 1 \quad (5.5.24)$$

when we consider a window function whose two large dimensions are given by the planar size of the wake which is fixed in comoving coordinates. The first guess would be to choose the small dimension to be given by the wake thickness which is increasing in comoving coordinates. Before making this choice, however, let us choose the thickness of the window to be fixed in comoving coordinates, and present a rough analytical analysis. The integral (5.5.23) is essentially cutoff by the radial planar size that corresponds to the comoving momentum k_r , and the orthogonal size that correspond to k_3 , with $k_3 \gg k_r$. We then obtain

$$\begin{aligned} \sigma_w^2 &\sim \frac{g^2(z)}{2\pi^2} \int_0^{k_3} dk_3 \int_0^{k_r} k_r P(\sqrt{k_r^2 + k_3^2}) \\ &\sim \frac{g^2(z)}{4\pi^2} k_r^2 \int_0^{k_3} dk_3 P(k_3). \end{aligned} \quad (5.5.25)$$

For a roughly scale-invariant power spectrum of Gaussian fluctuations, the final integral is dominated by scales which enter the Hubble radius at around t_{eq} where the power spectrum turns over (i.e. changes from scaling as k^{-3} for large values of k to scaling as k for small values). Let us denote this value of k as k_{to} . Then (5.5.25) yields

$$\sigma_w^2 \sim \frac{g^2(z)}{4\pi^2} \left(\frac{k_r}{k_{to}} \right)^2 \Delta(k_{to})^2, \quad (5.5.26)$$

where $\Delta(k)^2$ is given by (5.3.14). Note that the result is independent of k_z as long as $k_z \gg k_{to}$.

Our result (5.5.26) lets us draw important conclusions. Most importantly, the global delta criterium (5.5.24) is independent of the thickness of the wake, and hence independent of the string tension $G\mu$. The equation (5.5.26) also shows that wakes with larger planar extent, i.e., those laid down later, are easier to identify than smaller wakes. The dependence on k_r is linear. This prediction can be used as a consistency check on the numerical analysis.

Another nice feature about our result is that it tells us that we can choose a window function with a width greater than what we expect the local displacements of the wake to be.

We now turn to the quantitative evaluation of the condition. First, the comoving planar

dimensions of the wake can be read off from (5.1.3). They are

$$\psi_1 = \frac{c_1 t_0}{\sqrt{1+z_i}}, \quad (5.5.27)$$

$$\psi_2 = \frac{v\gamma t_0}{\sqrt{1+z_i}}, \quad (5.5.28)$$

The wake thickness in comoving coordinates depends on z and is given by equation (5.2.9)

Considering a wake region V centred at the origin of coordinate space in the form of a parallelepiped of volume $V_w = \psi_1 \times \psi_2 \times \psi_3$ the wake window function in real space becomes

$$W_w(X, Y, Z) = \begin{cases} \frac{1}{V_w} & \text{if } (X, Y, Z) \in V \\ 0 & \text{if } (X, Y, Z) \notin V \end{cases} \quad (5.5.29)$$

and the Fourier transform of the above quantity is

$$\tilde{W}_w(k_1, k_2, k_3, z) = \frac{1}{V_w(z)} \left[\frac{2 \sin(k_1 \psi_1/2)}{k_1} \right] \left[\frac{2 \sin(k_2 \psi_2/2)}{k_2} \right] \left[\frac{2 \sin(k_3 \psi_3(z)/2)}{k_3} \right]. \quad (5.5.30)$$

The variance of δ_w is given by (5.5.23). Replacing (5.5.30) into (5.5.23) results in

$$\sigma_w^2(z) = \frac{1}{(2\pi)^3} \left(\frac{g(z)}{V_w(z)} \right)^2 \int_{-\infty}^{\infty} \int_{-\infty}^{\infty} \int_{-\infty}^{\infty} dk_1 dk_2 dk_3 P(\|\vec{k}\|) \left(\left[\frac{2 \sin(k_1 \psi_1/2)}{k_1} \right] \left[\frac{2 \sin(k_2 \psi_2/2)}{k_2} \right] \left[\frac{2 \sin(k_3 \psi_3(z)/2)}{k_3} \right] \right)^2 \quad (5.5.31)$$

Note that in the integrand above the $2 \sin(k_3 \psi_3(z)/2)/k_3$ term together with the ψ_3 term of V_w approaches 1 as $G\mu \rightarrow 0$. Since for large k_3 the power spectrum also goes to zero, we can take this last term as 1 and hence for small $G\mu$ σ_w is independent of $G\mu$. This confirms our expectation from equation (5.5.26). But this does not mean string wakes are visible at arbitrarily low string tension. A wake should not be disrupted in order for it to be seen. In this sense the global delta condition is a necessary but not a sufficient reason for detection. Though very low $G\mu$ wakes may not be disrupted, they are not necessarily detectable, since cosmic string wake signals are proportional to the string tension (see introduction of Ref. [71] for a more detailed discussion of this point). We explicitly verified the independence of σ_w on $G\mu$ by evaluating the above integral numerically for several values from $G\mu = 0$ to 10^{-7} . It was assumed that $v\gamma(v) = c/\sqrt{3}$ and $z_i = 1000$. We find that $\sigma_w(0) = 0.32$. Note that the entire z dependence for $\sigma_w(z)$ is given by the $g(z)$ factor in front of the integral.

Until the time when dark energy becomes important we have $g(z) \propto 1/(z + 1)$ and

$$\sigma_w(z) = 0.32g(z) . \quad (5.5.32)$$

The plot of $\sigma_w(z)$ is shown in Figure 3. We conclude that even if the wake is locally disrupted, the overall density pattern remains manifest. Good strategies for cosmic string searches need to take this result into account.

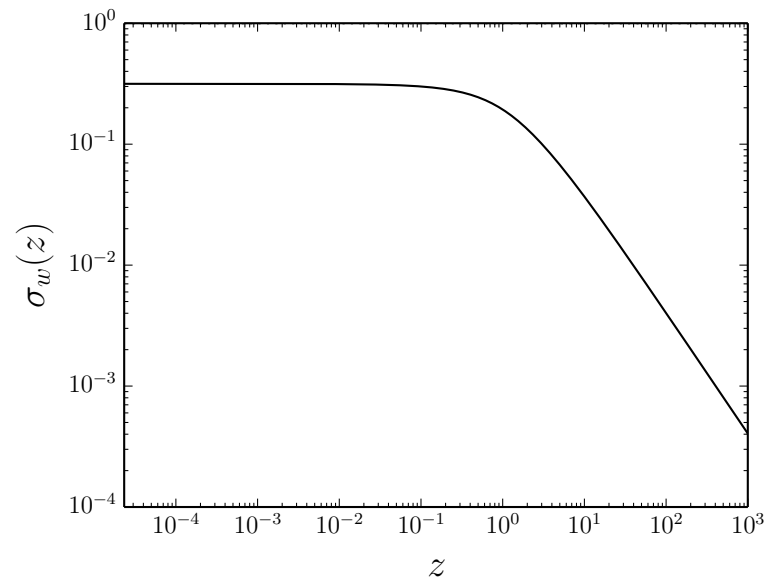


Figure 5.3 The r.m.s. value of the density contrast of the Gaussian perturbations in an anisotropic region which corresponds to the size of a wake produced at t_{eq} (vertical axis) as a function of redshift (horizontal axis). Note that the density fluctuations remain smaller than one.

Note that the $\sigma < 1$ conditions (both the global and local ones) are good provided the fraction of additional matter (due to the wake) that is within a region of the window function is of order one. In this case, δ will fluctuate around 1 inside the wake and around 0 outside, so $\sigma < 1$ will be a good condition to distinguish between the presence and absence of a wake in a given region of space.

5.6 Discussion and Conclusions

We have studied the disruption of a cosmic string wake by the gravitational effects of the Gaussian fluctuations which dominate the current spectrum of cosmological perturbations. At large redshifts, the wakes are stable whereas at smaller redshifts they are locally disrupted. The crossover redshift depends on the string tension $G\mu$. For $G\mu = 10^{-9}$ the crossover redshift is $z \simeq 11$. At redshifts greater than $z = 20$, wakes are stable down to tensions of $G\mu = 10^{-14}$. To arrive at this result, we investigated both a local density contrast criterion and a displacement criterion.

As an example, let us evaluate the possibility of seeing a $G\mu = 10^{-9}$ cosmic string wake in a particular slice of the 21 cm maps from the SKA. Just above its local disruption of $z \simeq 11$, such a generically oriented wake has a projected wake thickness Δz_{wake} , two orders of magnitude smaller than the SKA redshift resolution of $\Delta z_{\text{SKA}} = 10^{-4}$. The planar size of the wake is $N = 10^5$ times greater than the SKA angular resolution of 10^{-7} radians. Since the wake is not disrupted there is a slight overdensity over the entire $0.01 \text{ rad} \times 0.01 \text{ rad}$ region in redshift space. Consider those N^2 pixels that contain the wake as N^2 measurements in a no-wake theory. Knowing that the wake is undisrupted allows us to calculate the χ^2 between a no-wake theory and a theory with a wake for these pixels [93]. We find that $\chi^2 = N^2 \times (\Delta z_{\text{wake}}/\Delta z_{\text{SKA}})^2 = 10^6$. Such a large χ^2 results because we have assumed that all our pixels contain the wake. Obviously we have not addressed how to choose such candidate pixels, however here we wish only to show that a wake is visible in the scenario where our pixels do contain a wake.

The physical difference between the “Local delta condition” and the “Global sigma condition” is due to the fact that in the local criteria, the relevant scale of the problem is the wake thickness, and this scale is proportional to the string tension. On the other hand, as discussed above, the relevant scale for the global criteria is the planar dimension of the wake, which is independent of the string tension.

Even if Gaussian fluctuations locally disrupt a string wake, it could possibly be identified using a “Global Sigma Condition”. We have computed the r.m.s. density contrast due to the Gaussian fluctuations for an anisotropic window function whose planar dimensions correspond to those of a wake, and whose thickness is much smaller than the scale where the density power spectrum turns over and shown that the result is lower than 1 for all redshifts. Hence, if we smooth the density field with such a window function, then the wake

will be visible even if it is locally disrupted. This global condition is independent of the value of $G\mu$. We are looking for the dark matter component, so we do not have to consider (baryonic) diffuse wake corrections to the wake thickness.

Our work has implications for search strategies to find string signals. Local features of wakes (e.g., discontinuity lines in CMB polarization maps or sharp edges in three-dimensional 21cm redshift surveys) will only be visible for redshifts higher than the crossover redshift determined by our local criteria. In contrast, searches for string signals using global signals (e.g., statistical analyses of maps obtained by smearing the original maps by an anisotropic window function of the shape of the expected wake signal) will be promising even at very low redshifts. We are currently studying this question.

Chapter 6

Dark Matter Distribution Induced by a Cosmic String Wake in the Nonlinear Regime

6.1 Introduction

Cosmic strings are linear topological defects which arise in a large class of quantum field theory models describing physics beyond the Standard Model. If Nature is described by such a model, then a network of strings inevitably forms in the early universe and persists to the present time [94, 95]. Strings are thin lines of trapped energy density, and their gravitational effects lead to specific signatures which can be searched for in cosmological observations.

The network of cosmic strings¹ which form in a gauge field theory approaches a *scaling solution* in which the statistical properties of the distribution of strings is independent of time when all lengths are scaled by the Hubble radius (see e.g. [11, 15, 56] for reviews of cosmic strings and their role in cosmology). The string distribution has two components: firstly a network of infinite strings with mean curvature radius comparable to the Hubble radius t (where t is the physical time), and secondly a distribution of string loops with radii $R < t$. The loops result from the long string intersections which also are responsible for maintaining the long string scaling distribution. Analytical arguments lead to the

¹We are focusing on non-superconducting strings. In some quantum field theory models the strings can be superconducting [96] which will lead to additional effects of non-gravitational origin.

conclusion that the number N of long string segments that pass through any Hubble volume is of the order 1. The exact number must be determined in numerical cosmic string evolution simulations (see e.g. [9, 58–64] for some recent results). Current evidence is that $N \sim 10$.

Cosmic strings are characterized by their mass per unit length μ which is usually expressed in terms of the dimensionless quantity $G\mu$ (where G is Newton’s gravitational constant²). The value of μ is determined by the energy scale η at which the strings are formed (it is the energy scale of the phase transition leading to the strings)

$$\mu \sim \eta^2. \quad (6.1.1)$$

The strength of the signatures of cosmic strings in the sky is proportional to $G\mu$. The current upper bound on the string tension is

$$G\mu < 1.5 \times 10^{-7} \quad (6.1.2)$$

and is derived from the features of the angular power of cosmic microwave background (CMB) anisotropies [25, 26, 97] (see also [72–76, 78–80] for some older works). Searching for cosmic strings in the sky hence is a way to probe particle physics beyond the Standard Model “from top-down”, as opposed to accelerator searches which are more sensitive to low values of η and hence probe particle physics “from bottom-up”. The current bound on $G\mu$ already rules out the class of “Grand Unified” particle physics models containing cosmic string solutions with a scale of symmetry breaking which is on the upper end of the preferred range. Improving the upper bound on the cosmic string tension will lead to tighter constraints on particle physics models (see e.g., [57] for an elaboration on these points).

The long string segments lead to non-Gaussian signals in the sky characterized by specific geometrical signatures in position space maps. One set of string signatures comes from lensing produced by a string. Space perpendicular to a long straight string segment is a cone with deficit angle α given by [14]

$$\alpha = 8\pi G\mu. \quad (6.1.3)$$

The deficit angle extends to a distance t from the string [98]. Cosmic strings are relativistic

²Note that we are using natural units in which the speed of light is $c = 1$.

objects, and hence the curvature of the string segments (the curvature radius is of the order t) will induce relativistic motion of the string in the plane perpendicular to the tangent vector of the string. This will lead to line discontinuities in CMB anisotropy maps [33] of magnitude

$$\frac{\delta T}{T} = 4\pi v_s \gamma_s G \mu, \quad (6.1.4)$$

where v_s is the transverse speed of the string segment in speed of light units, and γ_s is the corresponding relativistic gamma factor.

A moving long string segment will also induce a velocity perturbation behind the string towards to plane determined by the tangent vector of the string and the velocity vector. This leads to a region behind the string with twice the background density called a cosmic string *wake* [27, 28, 65, 66]. A wake produced by a string passing through matter at time t will have comoving planar dimensions given by the Hubble radius at time t , and a comoving thickness which initially is given by the deficit angle (6.1.3) times the Hubble radius and which grows linearly in time as given by the result of an analytical analysis [30, 31] making use of the Zel'dovich approximation [29]. Hence, the comoving dimensions of a wake produced at time t are

$$c_1 t z(t) \times t z(t) v_s \gamma_s \times 4\pi G \mu v_s \gamma_s z(t) t, \quad (6.1.5)$$

where $z(t)$ is the redshift at time t , and c_1 is a constant of order unity which gives the string curvature radius relative to t .

According to the cosmic string network scaling solution, strings lead to a set of line discontinuities in CMB temperature maps. The overall distribution of these discontinuities is scale-invariant. However, since cosmic strings are primordial isocurvature fluctuations, they do not give rise to acoustic oscillations in the angular CMB temperature power spectrum, oscillations which are typical of adiabatic perturbations [23, 35, 70]. Hence, detailed measurements of the CMB angular power spectrum leads to the constraints on the string tension is given by (6.1.2). It is likely that the bound can be strengthened by analyzing CMB temperature maps in position space using statistical methods designed to identify linear discontinuities. Initial studies using the Canny edge detection algorithms [39, 41, 87], wavelets [26, 52, 53], curvelets [53] and machine learning tools [46, 47] have shown that

good angular resolution is key to obtaining improved constraints ³. Cosmic strings also lead to direct B-mode polarization in the CMB sky [36] (see also [22] for a recent review of signatures of cosmic strings in new observational windows) ⁴.

Cosmic strings also lead to distinct patterns in 21cm redshift surveys: a cosmic string wake present at a redshift before reionization will lead to a three-dimensional wedge of extra absorption in the 21cm maps because at these redshifts the wake is a region of twice the background density of neutral hydrogen and CMB photons passing through a wake suffer twice the absorption compared to photons which do not pass through the wake [37]. Strings also lead to a Wouthuysen-Field brightness trough in the integrated 21cm signal [71].

In contrast, there has been little recent work on how well the cosmic string tension can be constrained by the large-scale structure of the Universe at lower redshifts, well into the nonlinear region of gravitational clustering ⁵. In this paper, we take first steps at studying these signals. We will study how well a single cosmic string wake can be identified in N -body dark matter simulations of gravitational clustering.

Specifically, we include the effects of a cosmic string wake in a cosmological N -body simulation which evolves the dark matter distribution. We introduce a statistic which is designed to pick out the signal of a cosmic string wake in the “noise” of the primordial Gaussian fluctuations in a Λ *CDM* cosmology. Since the string wake grows only in the direction perpendicular to the plane of the wake, whereas the Gaussian fluctuations grow in all three dimensions, the Gaussian fluctuations will eventually disrupt the wake, as studied analytically in [32]. However, even once the wake has been locally disrupted, its global signal will persist for some time. We study how the redshift when this global signal ceases to be identifiable varies as the string tension changes. In the following, we shall call the Gaussian fluctuations in a Λ *CDM* cosmology simply as “Gaussian noise”.

³See also [99, 100] for earlier searches for position space signals of cosmic strings in CMB temperature maps.

⁴Searching for cosmic strings in position space has an additional advantage over analyzing only correlation functions such as the power spectrum: searching for signals of individual strings in position space maps leads to less sensitivity to the parameter N (number of long strings per Hubble volume) which is not yet well determined).

⁵Most previous work on cosmic strings signals in the large- scale structure has been in the context of string models [21, 67, 68] without Λ *CDM* fluctuations.

6.2 Wake Disruption

The challenge of identifying cosmic string wake signals in the nonlinear regime of structure formation was addressed in [32]. If a cosmic string wake is added to the initial conditions of a cosmological model which is characterized by a scale-invariant spectrum of primordial Gaussian cosmological perturbations, then the wake is clearly identifiable at high redshifts since the Gaussian perturbations are all in the linear regime whereas the wake is already a nonlinear density contrast. However, once the Gaussian perturbations become nonlinear, they will start to disrupt the wake.

A first criterion for the stability of a wake is that the local displacement S_k of matter on the comoving scale of the wake thickness $k^{-1}(t)$ due to the Gaussian fluctuations be smaller than the physical width of the wake $h(t)$, i.e.

$$S_k(t) < h(t). \quad (6.2.6)$$

If this condition is satisfied, then the wake should persist as a locally coherent entity. This condition was called the *local stability condition*. A closely related condition is the *local delta condition* which demands that the mean fluctuation Δ due to the Gaussian fluctuations on the scale k of the wake thickness be smaller than unity, i.e.

$$\Delta(k, t) < 1. \quad (6.2.7)$$

For a string tension of $G\mu = 10^{-7}$ it was found that the local delta condition is satisfied down to a redshift of $z \simeq 5$. The limiting redshift increases as the string tension decreases. For $G\mu = 10^{-11}$ the limiting redshift is $z \sim 11$, and this limiting redshift increases only slowly as the string tension is reduced further (for a string tension of $G\mu = 10^{-14}$ the limiting redshift is $z \sim 20$).

The above result shows that in principle very high redshift surveys of the distribution of matter in the universe such as what can be achieved by high redshift 21cm maps yield a very promising avenue to detect cosmic strings [37]. The challenge, however, is to be able to identify the very thin features (in redshift direction) which string wakes will produce.

As was also studied in [32], wakes might be identifiable through the global mass distribution which they induce even if they are locally disrupted. We can ask the question whether the Gaussian fluctuations are able to induce a nonlinear overdensity in a box of

the expected dimensions of a string wake. The contribution of the Gaussian fluctuations to the variance in a such a box $B(G\mu)$ is

$$\sigma_w^2 = \frac{g^2(z)}{(2\pi)^3} \int d^3k P(|k|) W_w^2(k), \quad (6.2.8)$$

where $P(|k|)$ is the power spectrum of the Gaussian noise, $g(z)$ is the cosmological growth factor, and $W_w(k)$ is a non-isotropic window function which filters out contributions from modes which have wavelength smaller than the width of the wake in one direction, and smaller than the extent of the wake in the two other dimensions. If $\sigma_w < 1$, then a string wake can be identified by its global signal (it will produce a nonlinear density contrast in this box). Thus, we can define the *global delta condition* for the identifiability of a string wake:

$$\sigma_w < 1. \quad (6.2.9)$$

It was found [32] that for a roughly scale-invariant power spectrum of primordial fluctuations the result for σ_w is to first-order independent of the thickness of the wake, and that the condition (6.2.9) remains satisfied down to redshift 0. Hence, in the absence of noise and with an unlimited resolution, a string wake should be identifiable even at present for any value of $G\mu$. In practice, however, the limited resolution of a survey (and the limiting resolution of numerical simulations) will limit the redshift range where the string wake can be detected.

The goal of the present study is to determine to what value of $G\mu$ cosmic string wakes can be identified in practice. Ultimately we are interested in comparing the results of numerical simulations of the distribution of matter, obtained if the usual initial conditions for the primordial fluctuations are supplemented with the presence of a cosmic string wake, with observational data. In the current project, we will study the distribution of dark matter only. Any observational data set will have a limiting resolution in the same way that any numerical simulation has a resolution limit. These limits will render the effects of string wakes harder and harder to detect the smaller the value of $G\mu$, in spite of the fact that the result (6.2.9) is independent of $G\mu$. In this paper, we wish to study whether the wake of a string with tension $G\mu = 10^{-7}$, a value just below the current upper bound, can be identified with simulations having a resolution which can currently be achieved.

In the next section, we describe the simulation code and various performance tests of

the code which we have performed. For these test runs, we use a value of $G\mu$, which is larger than the current upper bound in order to better visualize the results. In Section 4, we then present the output of runs or values of $G\mu$ down to $G\mu = 10^{-7}$, and study down to which redshift the wake signal can be identified with various statistics. In Section 5 we summarize the results and discuss prospects for deriving improved limits.

6.3 Simulations

6.3.1 The Code

This section describes the main features of the N -body simulations that we use to model numerically the wake evolution and its impact on the density field. We detail our wake insertion strategy and validate our results with consistency checks.

The simulations were produced with CUBEP³M, a public high performance cosmological N -body code based on a two-level mesh gravity solver augmented with sub-grid particle-particle interactions [101]. The initial conditions generator reads a transfer function constructed with the CAMB online toolkit⁶ and produces Λ CDM fluctuations at any chosen initial redshift z_i with the following cosmological parameter: $\Omega_\Lambda = 0.7095$, $\Omega_b = 0.0445$, $\Omega_m = 0.246$, $n_t = 1$, $n_s = 0.96$, $\sigma_8 = 0.8628$, $h = 0.70$, $T_{\text{cmb}}(t_0) = 2.7255$. The initial redshift is chosen such that the initial fluctuations are in the linear regime for all scales that we resolve. Except for a few cases, the initial redshift was $z_i = 63$. Particles are then displaced using linear theory [29], then evolved with CUBEP³M until redshift $z = 0$. Several test simulations were performed with various computational power on four systems: a laptop with four processors, a 64 cores computer cluster in the McGill Physics Department called irulan, and a set of 128 cores from the Guillimin Cluster and, finally, a set of 128 cores from the Graham Cluster. The two last clusters are part of the Compute Canada Consortium. The first two sets of simulations were launched as a single MPI task job, whereas the two last ones were distributed over eight compute nodes. The cosmological volume and the number of particles were varied, as summarized in Table 6.1. The most powerful simulation was performed in Graham, in a volume of $L_{\text{box}} = 64 \text{Mpc}/h$ per side, with $nc = 2048$ cells per dimension (corresponding to 1024 particles per dimension). The phase space output data was saved for checkpoints chosen in equal spaced logarithmic

⁶CAMB:https://lambda.gsfc.nasa.gov/toolbox/tb_camb_form.cfm

intervals for the scale factor. In addition to that, a few more checkpoints were added, corresponding in total to the following redshifts: 63, 31, 15, 10, 7, 5, 4, 3, 2, 1, 0.5, 0 (some other simulations contain 255 and 127 as well).

Machine	L_{box} (in Mpc/ h)	nc
ACER	40	240
irulan	64 and 32	512 and 256
Guillimin	64	1024
Graham	64	1024 and 2048

Table 6.1 Configuration of the various N -body simulations. L_{box} and nc are the side of the cosmological box and number of cells per dimension, respectively.

The ΛCDM part of the N -body code has been shown to match the predictions to within 5% over a large range of scales. We verify this in Fig. 6.1, where we compare the matter power spectrum $P(k)$ with the predictions at $z = 15$ for a ACER simulation with $L_{\text{box}} = 40 \text{Mpc}/h$ and $nc = 240$. The power spectrum is computed by first assigning the particles onto a density grid $\delta(x)$ using the cloud-in-cell interpolation, then squaring the Fourier transformed field $\delta(k)$ and averaging over the solid angle Ω : $P(k) = \langle |\delta(k)|^2 \rangle_\Omega$. The mass assignment scheme has been removed in this calculation, but the shot noise was not removed, which explains the large rise at $k > 10h/\text{Mpc}$. We observe that the agreement is indeed as expected, with a 10% match for $k < 3.0h/\text{Mpc}$, corresponding to scales $1.04 \text{ Mpc}/h$.

The reason we cannot achieve 5% precision on $P(k)$ is due to the fact that we do not fully capture the linear scales, because we are considering a small box size. We would normally need $L_{\text{box}} > 200 \text{ Mpc}/h$ to get 5% precision on $P(k)$. In our case, this is not an issue, since we are still producing representative ΛCDM fluctuations from which the wake must be extracted.

6.3.2 Wake Insertion

One of the goals is to produce particle distributions including the effects of a wake with a cosmic string tension compatible with the current limit of $G\mu = 10^{-7}$, which corresponds to a comoving width of $\approx 0.003h^{-1}\text{Mpc}$ at redshift 20, a redshift in which we have confidence that the wake is not yet locally disrupted [32].

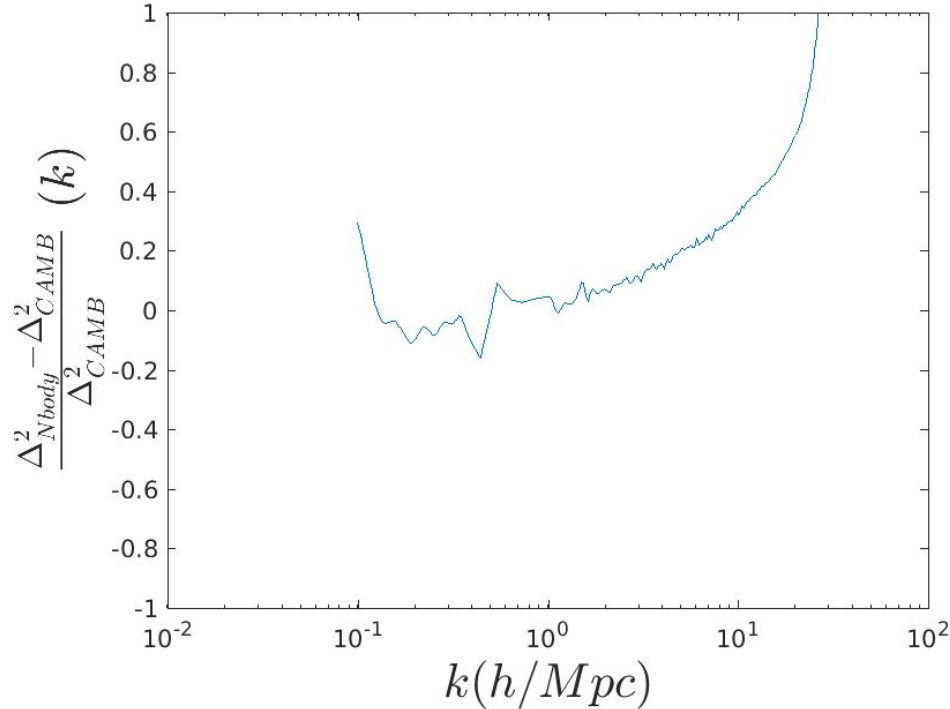


Figure 6.1 Plot of fractional error of the dimensionless power spectrum compared with the HALOFIT predictions of the online CAMB tool

For a given simulation without a wake, we evolved two independent simulations corresponding to wake insertions at redshifts $z = 31$ and $z = 15$ to test the sensibility of the results on the time of wake insertion. The advantage of an early insertion is that the dark matter distribution is in the linear regime. On the other hand, a late wake insertion corresponds to a thicker wake at the time of insertion, giving a better resolution of its thickness.

For each configuration, a Λ CDM-only simulation was evolved to $z = 0$, without the wake, writing the particle phase space at a number of redshifts including the wake insertion redshift. We next modified the particle phase space at the wake insertion redshift by displacing the particles and also giving them a velocity kick towards the central plane. The magnitudes of the velocity and displacement are calculated according to the Zel'dovich approximation [29].

We consider a wake which was laid down at the time t_{eq} of equal matter and radiation (such wakes are the most numerous and also the thickest). Their comoving planar distance

d is given by the comoving horizon at t_{eq} , namely

$$d = z(t_{eq})^{-1/2}t_0 \quad (6.3.10)$$

where t_0 is the present time. This distance is larger than the size of our simulation box, which justifies inserting the effects of a wake as a planar perturbation. The initial velocity perturbation towards the plane of the wake which the particles receive at t_{eq} is

$$\delta v = 4\pi G\mu v_s \gamma_s, \quad (6.3.11)$$

where v_s is the transverse velocity of the string and γ_s is the corresponding relativistic gamma factor. Since cosmic strings are relativistic objects, we will take $v_s \gamma_s = 1/\sqrt{3}$. In the following equations, however, we leave $v_s \gamma_s$ general.

The initial velocity perturbation leads to a comoving displacement $\psi(t)$ of particles towards the plane of the wake. This problem was discussed in detail in [30, 31], with the result that the comoving displacement at times $t > t_{eq}$ is given by

$$\psi(t) = \frac{3}{5}4\pi G\mu v_s \gamma_s t_{eq} z(t_{eq}) \frac{z(t_{eq})}{z(t)}. \quad (6.3.12)$$

The last factor represents the linear theory growth of the fluctuation, the previous factor of $z(t_{eq})$ represents the conversion from physical to comoving velocity. The (comoving) velocity perturbation is

$$\dot{\psi}(t) = \frac{2}{5}4\pi G\mu v_s \gamma_s t_{eq} z(t_{eq}) \frac{z(t_{eq})}{z(t)} \frac{1}{t}. \quad (6.3.13)$$

In our simulations the displacement and velocity perturbations towards the plane of the wake were given by (6.3.12) and (6.3.13), respectively, evaluated at the time $t = t_i$ of wake insertion. We then reload this modified particle data into CUBEP³M and let the code evolve again to redshift $z = 0$. This method ensures that the differences seen in the late time matter fields are caused only by the presence of the wake. The Λ CDM background is otherwise identical.

To test the wake insertion code, simulations were run with a large cosmic string tension of $G\mu = 4.0 \times 10^{-6}$. The following three panels each show a two-dimensional projection of

the resulting dark matter distribution at redshifts $z = 31$, $z = 10$ and $z = 3$. The results are from a Graham simulation with $nc = 512$ particles per dimension and a cubic lateral size of $64 \text{ Mpc}/h$. The initial conditions for the ΛCDM fluctuations were generated at $z = 255$, and a wake was inserted at $z = 127$.

The first figure shows the completely undistorted initial wake signal. At redshift $z = 10$ the wake is no longer perfectly uniform, and at redshift $z = 3$ the ΛCDM fluctuations have caused major inhomogeneities in the wake, and some small deflections. However, for this large string tension, the string fluctuations still dominate.

6.3.3 Known limitations

Our numerical modeling of a string-induced wake has multiple limitations. The first one concerns resolution and results from the fact that we are not always able to resolve the wake itself, which is increasingly thinner for lower string tensions. Ideally, the thickness of the wake should be at least as large as the simulation cell size, but this is not always feasible to achieve in a cosmological setup, given the computing resources at our disposal. For example, supposing we would like to resolve a wake produced by a cosmic string with tension $G\mu = 1.0 \times 10^{-7}$ at redshift $z = 7$, the grid size needs to be $0.01 \text{Mpc}/h$, which, assuming a large simulation with 8192 cells per dimension, corresponds to a lateral size of $\approx 57 \text{ Mpc}/h$. We circumvent this computing challenge by noting that the wake has a global impact on the matter field and that we do not need to resolve the initial wake exactly to detect its presence.

A second, less intuitive, limitation arises from the wake insertion itself: once every particle has been moved towards the wake, a planar region parallel to the wake is left empty at the boundary of the simulation box. In other words, the number of particles in the simulation is fixed, and the dislocation of the particles that is required to create the wake (an overdense region in the central plane of the simulation) produce at the same time an underdense region at the boundary plane. Although there is indeed a compensating under density at large distances from the wake (this is required by the “Traschen integral constraints”[\[102\]](#) on density fluctuations in General Relativity), the fact that the void occurs at the boundary of our simulation box is unphysical. Note, in particular, that in the simulations, the location of the underdensity depends on the box size, and it should be pushed to the horizon size at wake formation [\[98\]](#). In order to preserve the cosmological

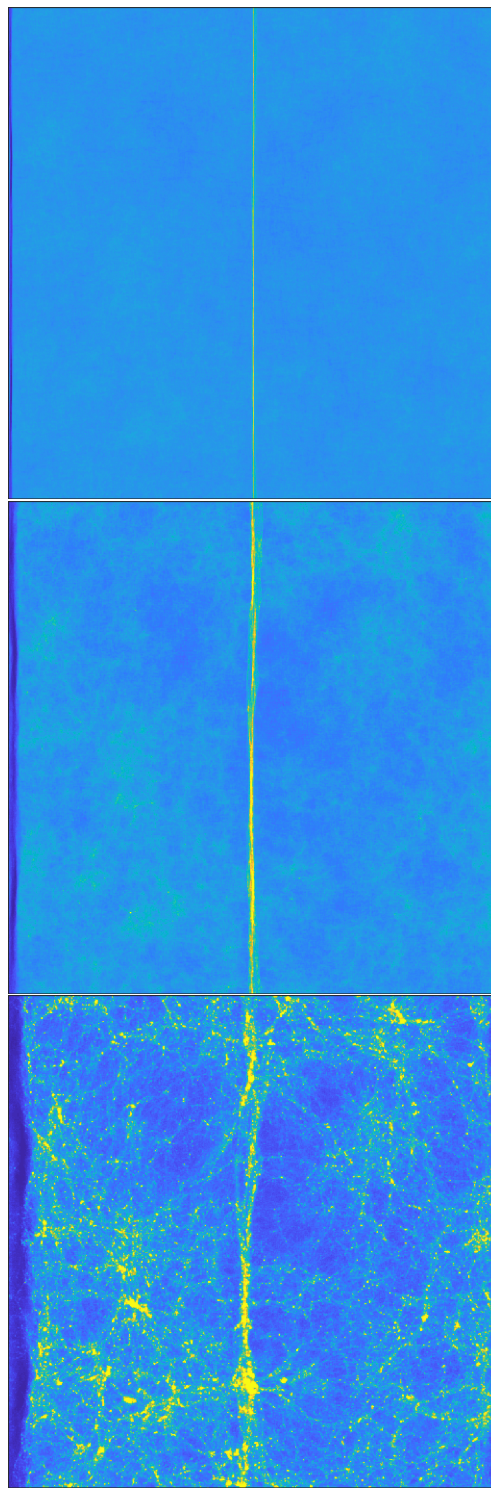


Figure 6.2 Density contrast of the two-dimensional projection of the dark matter distribution for a $G\mu = 4.0 \times 10^{-6}$ wake at redshift $z = 31, 10$ and 3 (from top to bottom, respectively). The color bar on the bottom associates each color with the corresponding density contrast

background in the simulation, we cannot introduce new particles to fill this empty region, and hence we have no way to get rid of this undesired effect.

Our approach is, therefore, to examine whether or not this void affects the evolution of the wake. We achieve this by measuring the displacement of the particles induced by the presence of the wake (and the corresponding void at the boundary) and comparing the result with the Zel'dovich approximation formula (6.3.12). Each particle in the simulation carries an identification number, and so it is possible to compute the position of a particle in a simulation without a wake and compare with the position of the same particle in the simulation that has an inserted wake. Since the only difference between the two simulations is the wake insertion, by subtracting the two positions, it is possible to obtain the displacement of this particle induced by the wake.

Figure 6.3 shows the displacement in the direction perpendicular to the wake induced on the particles by the presence of the wake. A Guillimim simulation with $G\mu = 8 \times 10^{-7}$, number of cells per dimension $nc = 512$ and lateral size $L = 64 \text{ Mpc}/h$ was used and the figure corresponds to $z = 10$, with a wake inserted at $z = 31$. The axis perpendicular to the wake was divided into bins with the same thickness as the cell size and the displacement associated to a given bin was computed by averaging over the displacements of all the particles inside it. The particles on the left receive a positive dislocation (towards the wake at the center), and the particles on the right side receive a negative displacement towards the wake, as expected.

A number associated to the displacement associated to the above case was computed by considering the mean of the positive part, the absolute value of the mean of the negative part and taking the average of those two quantities. The error associated with this displacement computation was the average of the standard deviation of each part (positive and negative). Figure 6.4 is a summary of this computation for different redshifts together with the expected result from the Zel'dovich approximation.

It can be seen from the results that the displacement induced by the wake in the simulation grows linearly in the scale factor as it should. However, in the worst case, it is about two times higher than the expected value.

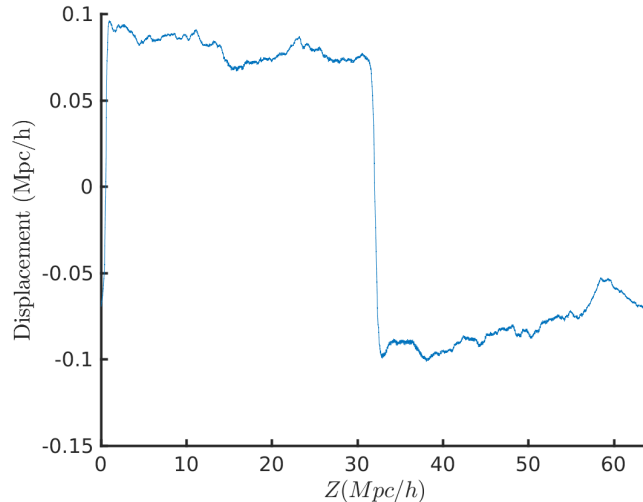


Figure 6.3 Plot of the induced displacement due to the wake as a function of axis position Z (horizontal axis) for redshift $z = 10$ and string tension $G\mu = 8 \times 10^{-7}$

6.3.4 Simulations

After these checks of the numerical code, we will turn to the Guillimin “production” runs. We performed 10 simulations without wakes. From the 10 samples, the first three were chosen for wake insertion and evolution, adding to the dataset three samples with $G\mu = 10^{-7}$ wakes and three with $G\mu = 8 \times 10^{-7}$ wakes. The lower value of $G\mu$ was chosen to be just slightly below the current limit on the string tension, the second one is a larger value for which the string effects are manifest and which can be used as a guide for the analysis.

All simulations have a grid of 1024 cells per dimension and 512 particles per dimension. The volume of the simulations is $(64)^3(h^{-1}\text{Mpc})^3$. The initial conditions were laid down at a redshift of $z = 63$, and the wake was inserted at redshift $z = 31$. To obtain a better resolution of the wake at the time of wake insertion, we also ran simulations where the wake was inserted at redshift $z = 15$. A later time of wake insertion, however, then leads to simulations where the effects of the ΛCDM fluctuations in the wake are neglected for a longer time. We will show that our final results do not depend sensitively on the redshift of wake insertion.

Figure 6.5 shows output maps of simulations at a range of redshifts. Output map sequences of simulations without a wake, including a wake with $G\mu = 8 \times 10^{-7}$, and a wake

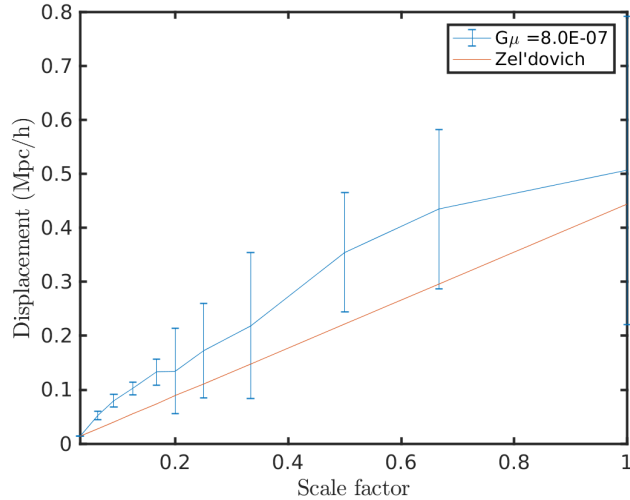


Figure 6.4 Plot of the displacement induced by the wake (in blue) for different values of the scale factor. The expected displacement evolution from Zel'dovich approximation is shown in red.

with $G\mu = 10^{-7}$ are shown. The wake is placed at the center of the box along the x-axis (the horizontal axis) and is taken to lie in the y-z plane. The y-axis is the vertical axis, and the mass has been projected along the z-direction.

Note that the initial thickness of the wake is 5% of the resolution of the simulation. With better resolution the wake would be more clearly visible, in particular at higher redshifts. Given the same computing power, we could increase the local resolution at the cost of reducing the total volume, and we could study the optimal values for the identification of the string signals. This challenge is similar to the challenge on the observational side, where observation resolution and sky coverage need to be balanced.

The leftmost column of Figure 6.5 shows the resulting mass distribution for redshifts $z = 10, 7, 4, 2, 0$ in a simulation without a wake, the middle column gives the corresponding output maps for a simulation including a wake with $G\mu = 8 \times 10^{-7}$, and with the same realization of the Gaussian noise. The wake leads to a planar overdensity of mass which is visible by eye as a linear overdensity along the y-axis. Until redshift $z = 4$ the wake is hardly distorted by the Gaussian noise (it appears as an almost straight line in the plots). At redshift $z = 2$ the linear overdensity is still clearly visible, although the Gaussian perturbations dominate the features of the map. By redshift $z = 0$ the wake has been disrupted, although the remnants of the linear discontinuity are still identifiable. The

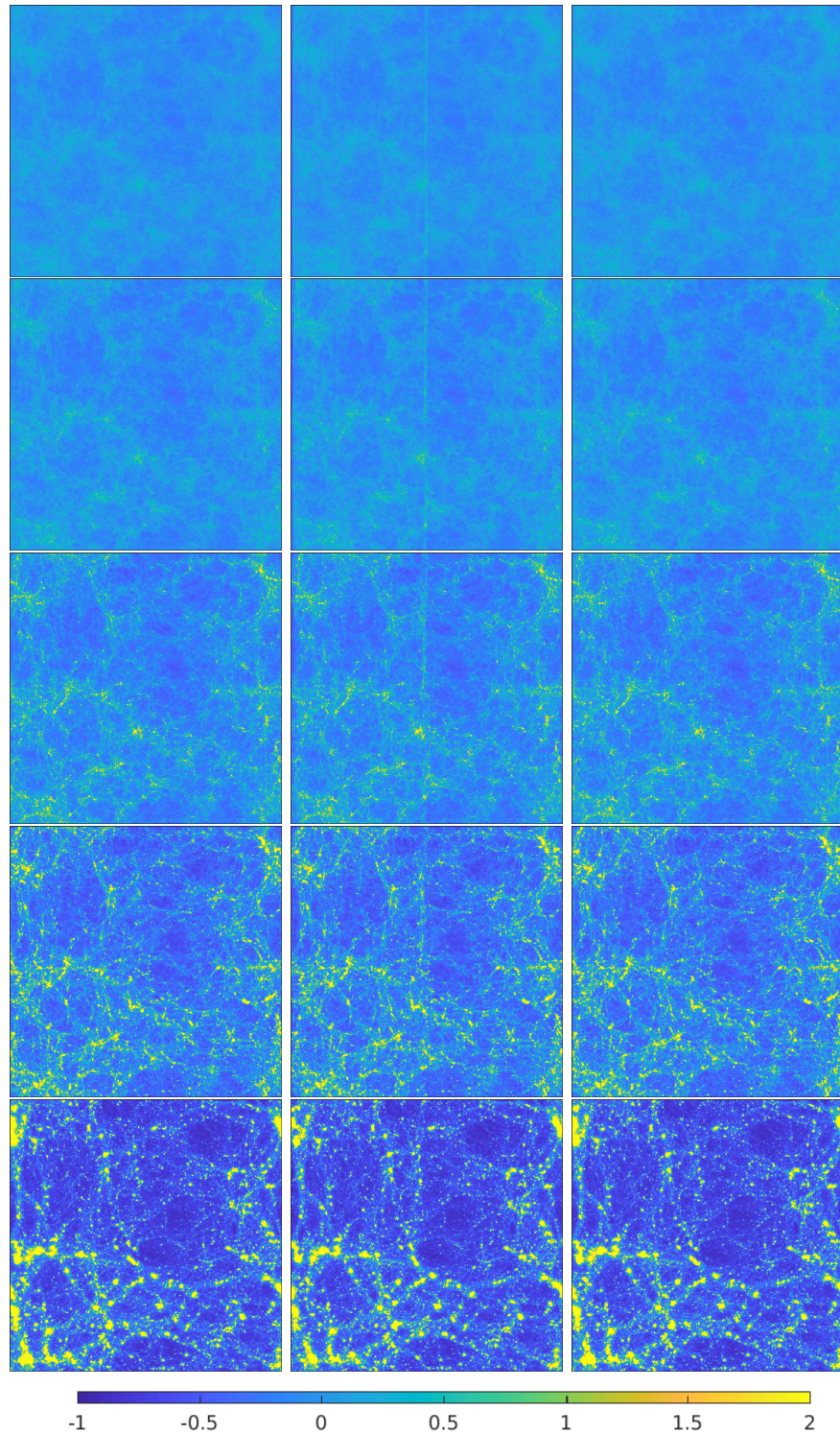


Figure 6.5 Each panel shows the density contrast of the density field projected in a $(64h^{-1}\text{Mpc}/h)^2$ area. Each row depicts a redshift snapshot, chosen to be $z = 10, 7, 4, 2, 0$ from top to bottom. The left column corresponds to pure Λ CDM, the middle contains a $G\mu = 8 \times 10^{-7}$ wake and the right column contains a $G\mu = 1 \times 10^{-7}$ wake. The color bar on the bottom associates each color with the corresponding density contrast

challenge for a statistical analysis is to extract the wake signal at the lowest redshifts in a quantitative way. The rightmost column of Figure 6.7 shows the corresponding output maps for a simulation including a wake with $G\mu = 10^{-7}$, again with the same realization of the Gaussian noise. In this case, the wake is a factor of 8 thinner and creates primordial fluctuations which are suppressed by the same factor. The planar overdensity due to the wake is only (and even then only extremely weakly) identifiable at redshift $z = 10$. The challenge will be to extract this signal in a manifest way.

6.4 Statistical Analysis

6.4.1 1-d Projections

Our first step in the statistical analysis of the output maps is to consider a further projection of the density, namely a projection onto the direction perpendicular to the wake. Figure 6.6 shows the resulting distributions for a selection of redshifts (decreasing from top to bottom) for a simulation without a wake (left column), including an added wake with $G\mu = 8 \times 10^{-7}$ (middle column) and $G\mu = 10^{-7}$ (right column), in both cases with the same realization of the Gaussian noise. The vertical axis shows the relative density contrast, the horizontal axis is the coordinate perpendicular to the wake. The wake corresponds to the peak located at distance $d_z \simeq 32h^{-1}\text{Mpc}$. At redshifts $z = 15$ and $z = 10$ the wake can be clearly identified by eye at this redshift even for $G\mu = 10^{-7}$.

As the wake gets disrupted by the Gaussian noise, the wake signal gets harder to identify at lower redshifts. For $G\mu = 10^{-7}$ the signal can be seen at redshift $z = 10$, but it has disappeared by $z = 7$, while for $G\mu = 8 \times 10^{-7}$ the signal is still present at $z = 3$, but no longer at $z = 0$.

Wakes are very thin compared to the scale where the power spectrum of the Gaussian density perturbations peaks. This is particularly true for lower values of the string tension. Hence, a promising method of rendering the wake signal more visible is to perform a wavelet transform of the 1-d projection plots.

We have applied the *continuous Morse wavelet transformation* [103] to the above 1-d projection plots, and below we show some of the results. The basis used for the continuous wavelet transform is the Generalized Morse Wavelet [103] which has two parameters: β , measuring compactness and γ , characterizing the symmetry of the Morse wavelet. We

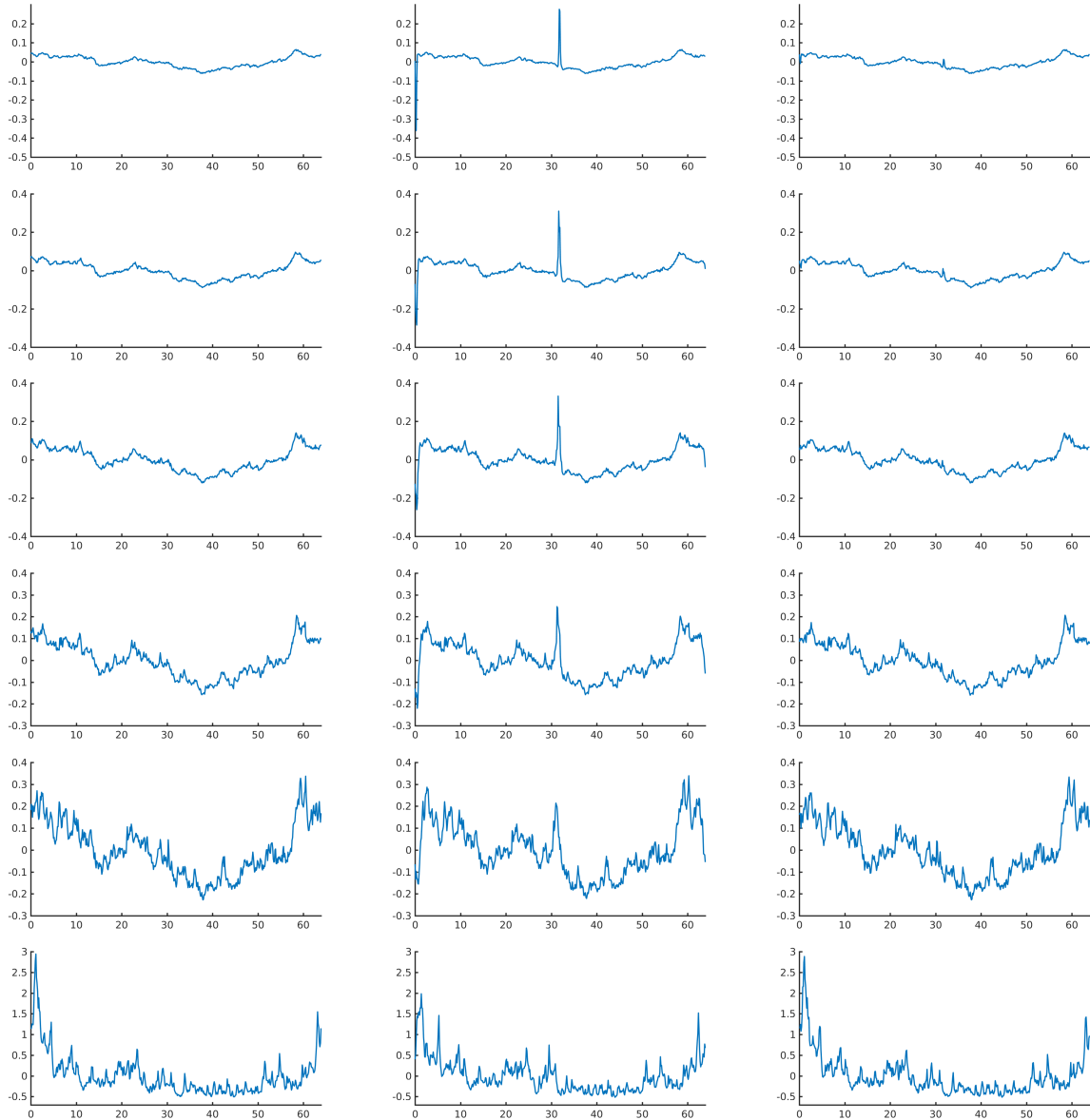


Figure 6.6 Each panel shows the density contrast of the density field projected in a $(64 \text{ Mpc}/h)$ axis perpendicular to the wake, when there is one. Each row depicts a redshift snapshot, chosen to be $z = 15, 10, 7, 5, 3, 0$ from top to bottom. The left column corresponds to pure ΛCDM , the middle contains a $G\mu = 8 \times 10^{-7}$ wake and the right column contains a $G\mu = 1 \times 10^{-7}$ wake.

choose $\gamma = 3$ (corresponding to the symmetric case). There are few oscillations if we choose β close to γ , so $\beta = 3.01$ is suitable for discontinuities detection. The wavelets are thus characterized by the position Z where they are centered and by their scale parameter (width) w . In the following plots of figure 6.7), the horizontal axis is Z , the vertical axis is the scale parameter. The color is a measure of the modulus of the wavelet coefficients.

A wake is a very thin feature at a particular value of Z . Hence, the wave signal will be concentrated at the lowest values of the scale parameter. Figure 9 shows a comparison between the wavelet transform coefficients in simulations without a wake (top) and including a wake with $G\mu = 10^{-7}$ (bottom) and $G\mu = 8 \times 10^{-7}$ (middle), all at a redshift of $z = 10$. The Gaussian noise gives rise to features in the continuous wavelet map which are mostly concentrated at large scale parameters, although there are some features which also appear at small scale parameters. As seen in the bottom panel of Figure 7, the wake adds a narrow feature at the value of Z where the wake is centered, which continues to $w \simeq 0.4h^{-1}\text{Mpc}$. It can be characterized as a narrow spike. The wake-induced spike and the spike-like features in the no-wake simulation can be distinguished in that the features coming from the Gaussian noise weaken as w approaches its minimum value, and are wider than the wake-induced spike. Note that the color scaling is the same in the three panels. We see that the wake signal stands out very strong at $z = 10$ for a wake with $G\mu = 10^{-7}$, and that it totally dwarfs all other features for $G\mu = 8 \times 10^{-7}$. The above maps are obtained for a high-resolution sampling along the Z direction (we move the center position of the wavelet in steps of 0.5 of the grid size).

Since the wavelet expansion is an expansion in a complete set of functions, it is possible to reconstruct the original data from the wavelet transform. By setting to zero all wavelet coefficients corresponding to scales higher than a given cutoff, here taken as $0.4h^{-1}\text{Mpc}$, we can construct filtered 1-d projection graphs in which the long-wavelength contributions of the Gaussian noise are eliminated and in which the string wake signal is more clearly visible. If we apply the reconstruction algorithm to the filtered wavelet maps, we can construct a *filtered 1-d projection* graph in which the long-wavelength contributions of the Gaussian noise are eliminated and in which the string wake signal is more clearly visible.

Figure 8 show the reconstructed filtered 1-d projection graphs at redshift $z = 10$ in the case of pure Gaussian noise (top panel), and including a string wake with $G\mu = 10^{-7}$ (bottom panel) and $G\mu = 8 \times 10^{-7}$ (middle panel). As in the previous two graphs, the horizontal axis is the coordinate Z , and here the vertical axis is the density contrast. The

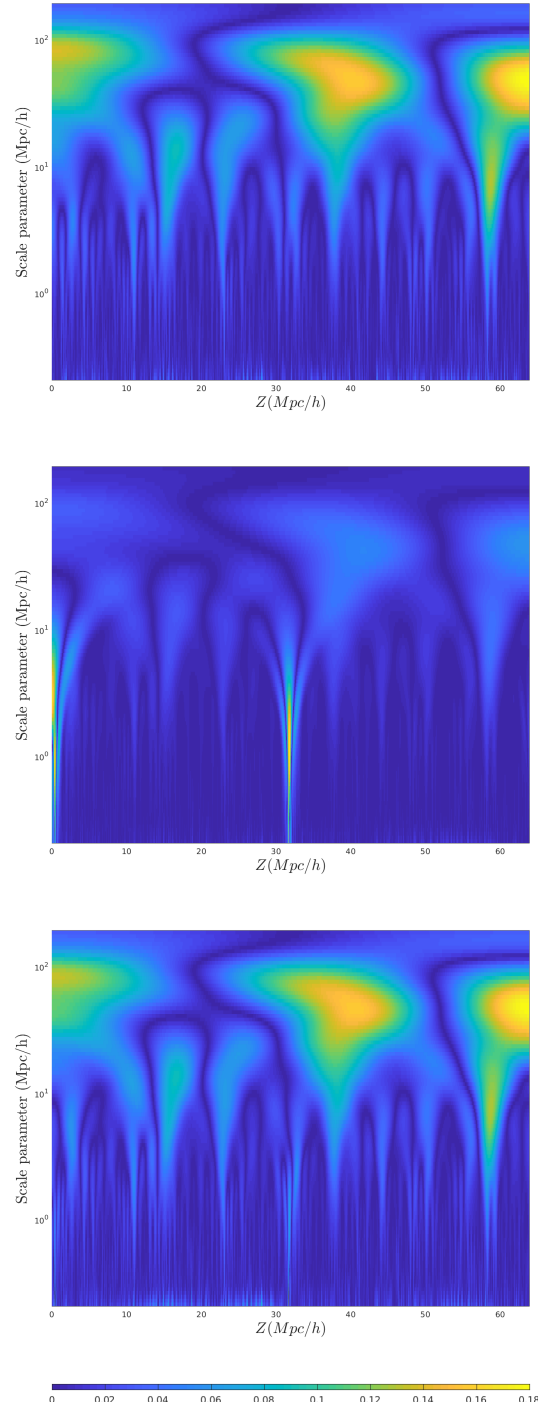


Figure 6.7 Continuous wavelet transforms of the density contrast of the 1-d projected dark matter density. The horizontal axis is the position parameter of the wavelet decomposition (with $Z = 32$ being the position of the wake), and the vertical axis is the width of the wavelet. The top panel is for a simulation without a wake, the middle panel includes a wake with $G\mu = 8 \times 10^{-7}$, and the bottom panel has a wake with $G\mu = 10^{-7}$. Note that the Λ CDM fluctuations are the same in all three simulations.

wake signals are greatly enhanced compared to what can be seen in the unfiltered projection graphs. For the value of $G\mu = 10^{-7}$, the wake signal is now almost an order of magnitude higher in amplitude than the peak value in the case of pure Λ CDM fluctuations.

To show a comparison, we can apply the continuous wavelet transformation to the one-dimensional projection filtered map, obtaining Figure 9. Comparing Figures 9 and 7, we see that the wake signal has been greatly enhanced by filtering.

A statistic which can be used to quantify the significance of the wake signal is the *signal to noise ratio* \mathcal{R} which we define to be

$$\mathcal{R} = \frac{s - \bar{n}}{\sigma(n)}, \quad (6.4.14)$$

where s is the peak value of the filtered 1-d projection graph with a wake, and \bar{n} is the mean of the peak value of the filtered 1-d projection graph without a wake for the 10 samples and $\sigma(n)$ is the standard deviation of the peak value of the filtered 1-d projection graph without a wake for the same 10 samples. We find that the average of the signal to noise ratio is

$$\bar{\mathcal{R}} = 17.07 \pm 0.83, \quad (6.4.15)$$

at redshift $z = 10$ in the case of a wake with $G\mu = 10^{-7}$ initially laid down at redshift $z = 15$ (the error bars are the standard deviation based on three simulations). Hence, we find that a cosmic string wake is identifiable with a 17.07σ significance. At redshift $z = 7$ the difference in the signal to noise is no longer statistically significant.

The results of the signal to noise analysis are given in the following figure (10). The horizontal axis gives the redshift (early times on the left), and the vertical axis is the signal to noise ratio. The bottom curve gives the results for a pure Λ CDM simulation, the next pair of curves (counting from bottom-up) give the results of a simulation where a wake with $G\mu = 10^{-7}$ is added, and the top two curves correspond to adding a wake with $G\mu = 8 \times 10^{-7}$. The two members of the pair correspond to different redshifts of inserting the wake. The difference in the predictions by changing the wake insertion time is not statistically significant. This figure shows the signal to noise ratios of the reconstructed 1-d projection graphs after wavelet transformation and filtering, for the high sampling scale. For $G\mu = 10^{-7}$ the wake effect can be clearly seen up to a redshift of $z = 10$, and for $G\mu = 8 \times 10^{-7}$ up to a redshift of $z = 5$.

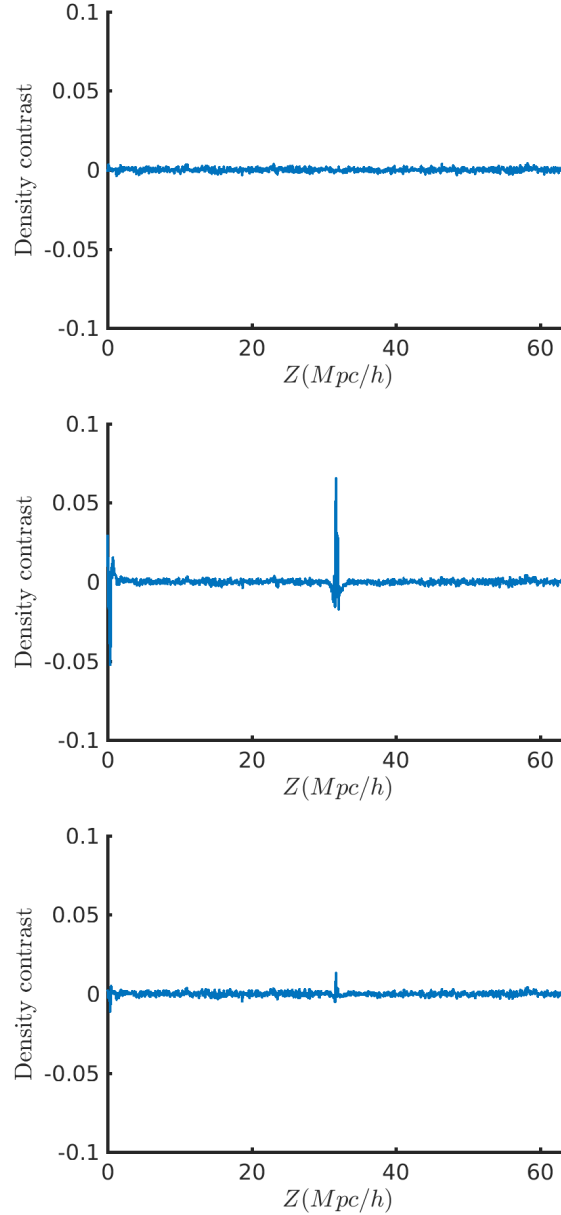


Figure 6.8 Reconstruction of the 1-d density contrast from the filtered wavelet transforms. The vertical axis is the density contrast, the horizontal axis is the distance of the projection plane from the wake plane. The top panel is the result of a simulation without a wake, the middle panel has a wake with $G\mu = 8 \times 10^{-7}$, and the bottom panel has a wake with $G\mu = 10^{-7}$. The data is for a redshift $z = 10$. Note that the wake signal is greatly enhanced compared to the original 1-d projection graphs of Fig. 8.

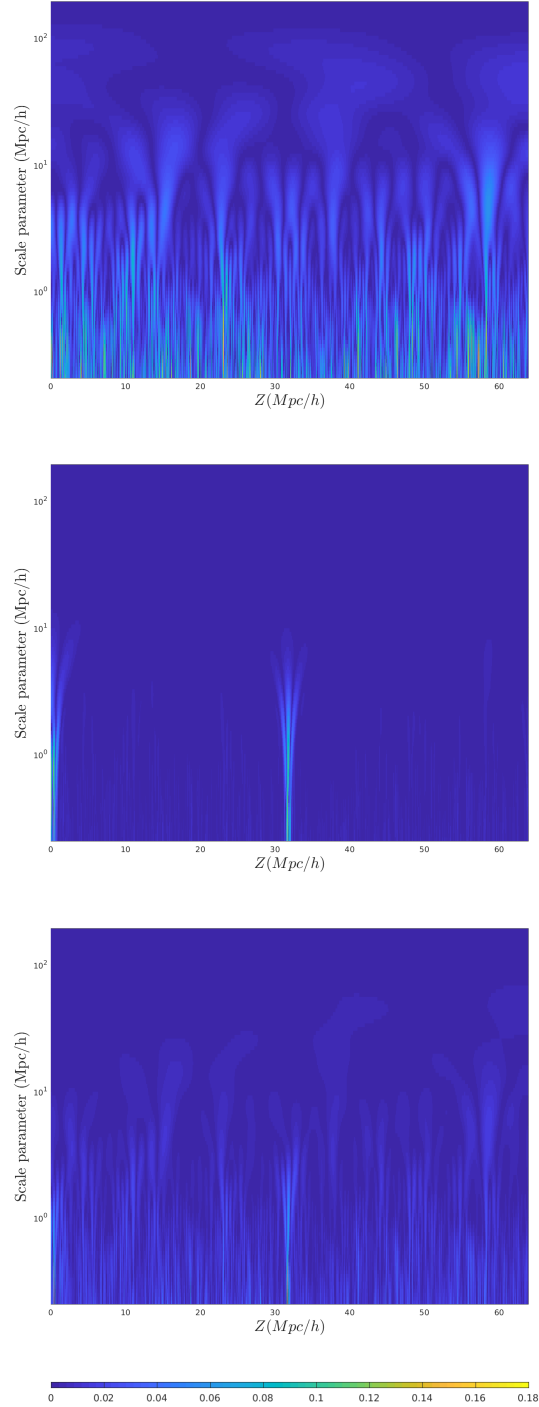


Figure 6.9 Continuous wavelet transforms after filtering. The axes are like in figure 7. The top panel is without a wake, the middle panel has a wake with $G\mu = 8 \times 10^{-7}$, and the bottom panel is for a wake with $G\mu = 10^{-7}$.

6.4.2 Spherical Statistic

In the previous analysis, the statistical analysis was based on an algorithm which presupposed knowing the planar orientation of the wake. For applications to data, we need an analysis tool which does not use this information. In this section, we develop such a statistic, which is an adaptation of a 3D ridgelet analysis ([104]).

The idea is to take the filtered one-dimensional projection, similar to Figure 8, for different directions on the sky and compute a relevant quantity. For choosing the angles, a Healpix [105] scheme was used⁷ with the help of S2LET [106], a free package available at www.s2let.org. The statistic is constructed in the following way: for any direction of the sphere, we consider an associated projection axis passing through the origin of the box. We then consider slices of the simulation box perpendicular to that axis at each point x of it with thickness given by the grid size of the simulation, and we compute the mass density $\delta(x)$ of dark matter particles in that slice as function of x . The range of x is half the simulation box, so we avoid slices with a small area (compared with the face of the cubic simulation box). A one-dimensional filter wavelet analysis similar to the one described in the previous section is then performed in the mass density $\delta(x)$, giving a filtered version for it, called $f\delta$.

We then compute the maximum value S of $f\delta(x)$ for each direction on the simulation. S is the map on the surface of the sphere which we now consider, and \hat{S} is its maximum value. For a simulation including a cosmic string wake with $G\mu = 1 \times 10^{-7}$ the resulting map at redshift $z = 10$ is shown in the top left panel of Figure 11, whereas the analysis without the wake is shown in Figure 12. The value of S is indicated in terms of color (see the sidebar for the values).

The wake signal appears at the center of the box, and its associated S value is about 40% higher than the maximum of the S value for the map without a wake. This can be better visualized in figures 13 and 14, where the center is zoomed-in 40 times. For each map, a peak \hat{S} over standard deviation σ of S was computed, and it was found that $\hat{S}/\sigma = 8.68$ for a simulation without wake and $\hat{S}/\sigma = 14.32$ for the simulation with a 1×10^{-7} wake.

A wake perpendicular to a particular direction will yield a high signal since the mass in the slice which overlaps with the wake will get a large contribution localized at a particular value of x .

⁷we choose $N_{side} = 512$,

The Healpix scheme does not contain the angles $(\theta, \phi) = (0, 0)$ where we know the wake is located, so we never probe the orientation exactly were the wake is. The wake signal has to be reached by increasing the resolution of the analyzed angles. This supports the idea that the information regarding the orientation of the angles should not be included in the analysis.

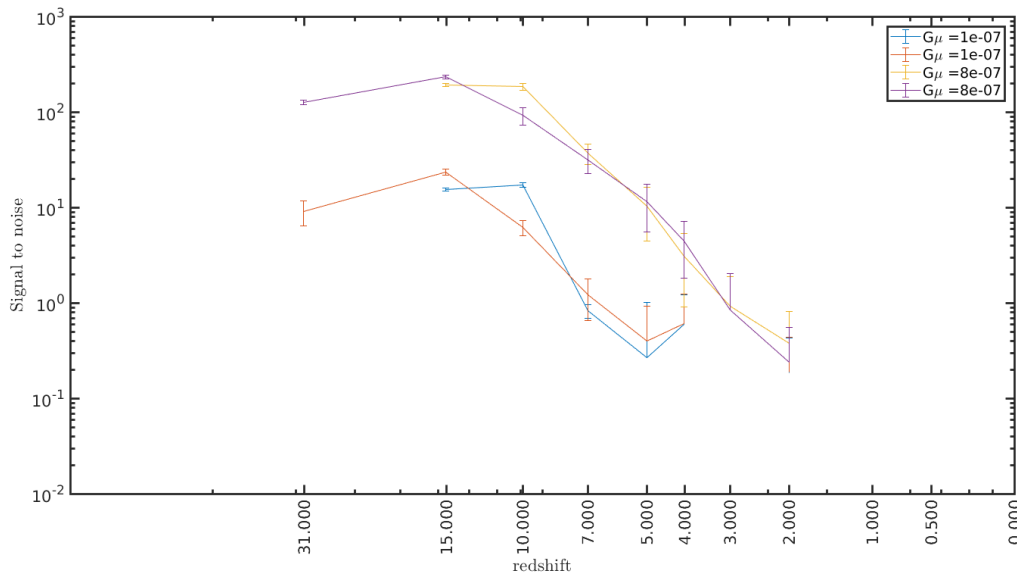


Figure 6.10 Signal to noise analysis for the 1-d projections after wavelet transformation, filtering and reconstruction, and for the finer of samplings in wavelet width. The horizontal axis shows the redshift, the vertical axis is the signal to noise ratio. The two pair of curves in the bottom contains a wake with $G\mu = 10^{-7}$, and the top two curves are for a wake with $G\mu = 8 \times 10^{-7}$. The two members of a pair of curves correspond to different redshifts of wake insertion (as is obvious from the starting points of the curves). The points that are not shown correspond to values for the signal to noise equal to zero.

At the present level, our analysis shows that cosmic string wakes with a tension of $1 \times G\mu = 10^{-7}$ can be extracted at redshift $z = 10$, as was found in our previous study where knowledge of the orientation of the wake was assumed. In work in progress, we are investigating whether string wakes are in fact visible at lower redshifts using this more sophisticated statistic. One could first imagine that an analysis which uses the knowledge of the wake orientation will yield better results than one which does not, but this may not be the case here since the analysis of this section uses more properties which differentiate

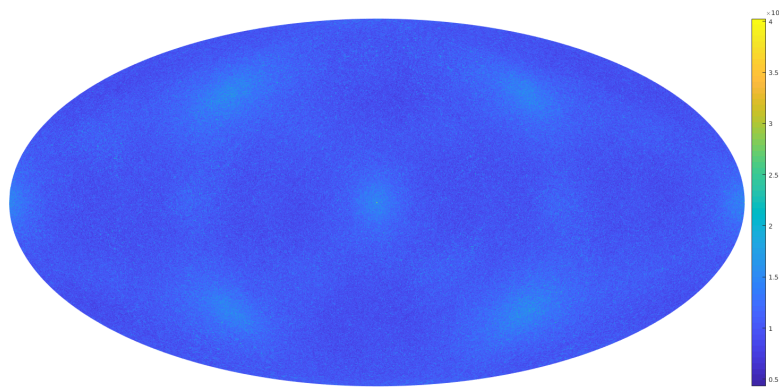


Figure 6.11 Reconstructed map for a simulation with wake tension $G\mu = 1 \times 10^{-7}$ at redshift $z = 10$.

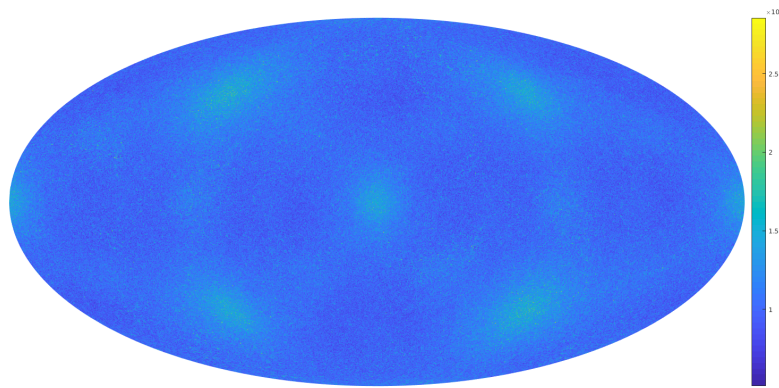


Figure 6.12 The same map for a simulation without a wake, at redshift $z = 10$.

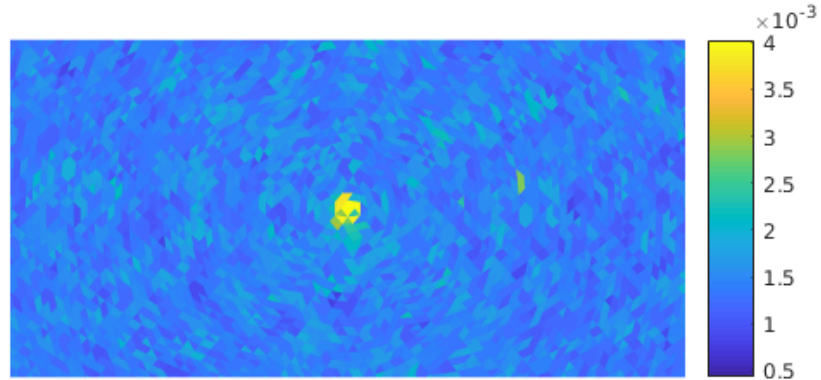


Figure 6.13 $40 \times$ zoom of the reconstructed map for a simulation with wake tension $G\mu = 1 \times 10^{-7}$ at redshift $z = 10$.

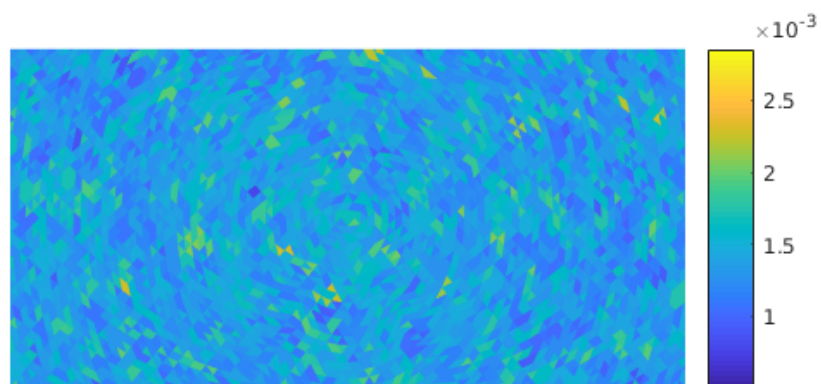


Figure 6.14 $40 \times$ zoom of the the same map for a simulation without a wake, at redshift $z = 10$.

Λ CDM fluctuations and wake signals than the previous analysis did.

6.5 Conclusions and Discussion

We have presented the results from N-body simulations of the effects of a planar cosmic string wake on the distribution of dark matter. We have demonstrated that cosmic string signals can be extracted from the background of Λ CDM fluctuations by considering the three-dimensional distribution of dark matter. Given the current resolution of the simulations, a threshold of

$$G\mu = 10^{-7} \quad (6.5.16)$$

can be reached if the dark matter distribution is considered at redshift $z = 10$. This value of the string tension is competitive with the current limit, which stems from the angular power spectrum of CMB anisotropies. With improved resolution, improved limits may be within reach. This means that the string signal might be identifiable for $G\mu = 10^{-7}$ even at redshifts lower than $z = 10$, and for smaller values of $G\mu$ at redshift $z = 10$.

Key to this work is that we are looking for the specific non-Gaussian signals which cosmic string wakes induce in position space. Position space algorithms are much more powerful at identifying cosmic string signals than by focusing simply on the power spectrum. It is possible that with improved statistical tools, better limits on the string tension can be reached. Work on this question is in progress.

Searching for signals of individual cosmic string wakes in position space has a further advantage compared to studying only the power spectrum: the position space algorithms are to first approximation insensitive to the number N of strings passing through each Hubble volume. This number is known only to within an order of magnitude, although we know from analytical arguments (see e.g., [15]) that N should be of the order one. In particular, this means that the constraint (6.1.2) on $G\mu$ from the angular power spectrum of CMB anisotropies is sensitive to the value of N which is assumed, whereas our analysis is not.

In this work, we have shown that by analyzing the distribution of dark matter, an interesting threshold value of the cosmic string tension can be reached. In future work, we plan to explore how changing the size of the simulation box, the spatial resolution of the simulations, and the sampling width can lead to improved bounds.

So far we have considered simulations with a single cosmic string wake. An extension of our work will involve studying the effects of a full scaling distribution of strings. This work will be conceptually straightforward but computationally intensive. Another extension for the current work would be to consider curvelet-like signal extraction, in which segments of the wake would be detected, possibly giving more information about the wake presence when it is bent due to the Λ C DM fluctuations at low redshifts, and it is not a plane anymore.

In order to compare our simulation results to observational surveys, we need to extend our work in several ways. To compare our work with optical and infrared galaxy survey results, we need to identify halos from our distribution of dark matter and run the statistical tools on the resulting distribution of halos. The N-body code we are using already contains a halo-finding routine. Hence, this extension of our work will also be straightforward.

As we have seen, the string signals are much easier to identify at higher redshifts. Hence, 21cm surveys might lead to tighter constraints on the cosmic string tension. At redshifts lower than the redshift of reionization, most of the neutral hydrogen which gives 21cm signals is in the galaxies. Hence, the distribution of 21cm radiation could be modeled by considering the distribution of galaxy halos obtained from our simulations and by inserting into each halo the distribution of neutral hydrogen obtained recently in the study of [107]. We plan to tackle this question in the near future.

The effect of cosmic strings on the 21cm signal from the *Epoch of Reionization* is a more difficult question. Here, the ionizing radiation from cosmic string loops (e.g. via cosmic string loop cusp decay [108]) will most likely play a dominant role. Finally, at redshifts greater than that of reionization, string wakes lead to a beautiful signal in 21cm maps: thin wedges in redshift direction extended in angular directions to the comoving horizon at t_{eq} where there is pronounced absorption of 21cm radiation due to the neutral hydrogen in the wake [37].

6.6 Peak Heights

In this appendix, we add a figure showing the distribution of peak heights used in the statistic in Section IV.A. The horizontal axis gives the redshift, the vertical axis is the peak height. Shown are the results for ten simulations without a wake (marked “o”) and for three simulations each with a wake with tension $G\mu = 10^{-7}$ inserted at redshift $z = 31$

(marked “*”), with the same tension and insertion redshift $z = 15$ (marked “+”), with tension $G\mu = 8 \times 10^{-7}$ and insertion redshifts $z = 31$ (marked with inverted triangles) and $z = 15$ (marked “x”).

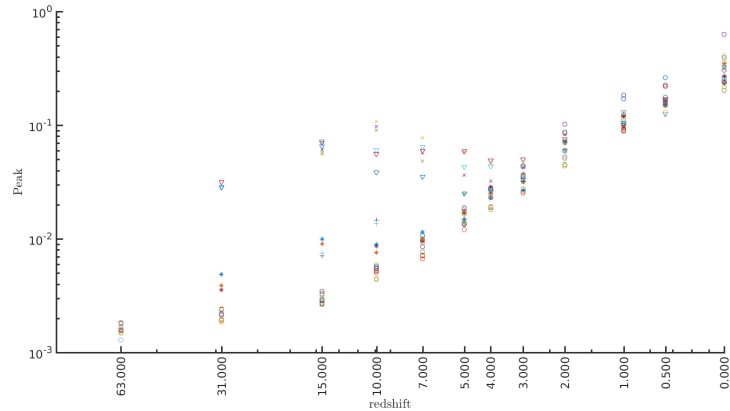


Figure 6.15 The peak values for simulations without a wake are marked by circles, for those with a wake with tension $G\mu = 10^{-7}$ inserted at redshift $z = 31$ and $z = 15$ by “*” and “+”, respectively, and for those with tension $G\mu = 8 \times 10^{-7}$ inserted at redshifts $z = 31$ and $z = 15$ by inverted triangles and “x”, respectively.

From this figure it is clear that wakes with $G\mu = 10^{-7}$ are identifiable until redshift of $z = 10$ while those with $G\mu = 8 \times 10^{-7}$ can be identified down to below $z = 7$.

Chapter 7

Cosmic String Wake Detection using 3D Ridgelet Transformations

7.1 Introduction

Cosmic strings [7] are topological defects [15] which arise in a range of relativistic quantum field theory models (for reviews see [15] and [11, 16]) beyond the Standard Model of particle physics. Good analogs of cosmic strings are vortex lines in superfluids and superconductors. Like their condensed matter counterparts, cosmic strings form lines of trapped energy density. This energy density can curve space-time and have important effects in cosmology [21, 109].

Cosmic strings are relativistic objects that can be described by a unique number μ . This quantity is the mass per unit length of the string, which is also equal to its tension. Alternatively, the string can be described by the dimensionless number $G\mu$, where G is Newton's gravitational constant. The value of μ is determined by the energy scale η at which the cosmic string is formed via the relationship [15]

$$\mu \sim \eta^2. \tag{7.1.1}$$

The cosmological signatures of cosmic strings are thus more substantial for larger values of μ which implies larger values of the energy scale η . Hence, searching for cosmic strings is a way to probe for new physics beyond the Standard Model of particle physics “from top-down”, in contrast to accelerator experiments which are more sensitive to new physics

at lower energy scales.

Cosmic strings lead to specific non-Gaussian signals in cosmic microwave background (CMB) temperature anisotropy maps, namely lines across which the temperature jumps by a value proportional to $G\mu$ [33, 110]. Edge detection algorithms [41] as well as wavelet and curvelet statistics [26, 52, 53] have been shown to be promising ways to search for these signals, and machine learning techniques [46, 47] have also recently been shown to have great promise. The current robust limit ¹ on the cosmic string tension is [25, 97]

$$G\mu < 1.5 \times 10^{-7}, \quad (7.1.2)$$

which rules out some Grand Unified particle physics models with very high scale symmetry breaking. This limit comes from the observational upper bound on the contribution of cosmic strings to the angular power spectrum of cosmic microwave background (CMB) anisotropies obtained by combining results of the WMAP satellite [113] with those of the South Pole Telescope [114]. Both improving the constraint on the cosmic string tension or detecting the signature of cosmic strings would help to constrain particle physics at high energy scales.

Cosmic strings come in two different forms: loops and infinite segments [15]. Cosmic string loops are formed when the infinite segments self-intersect. These loops then oscillate because of their tension and slowly decay by emitting gravitational waves. Numerical simulations lead to the conclusion that the number N of long string segments that pass through any Hubble volume is of order $N \sim 10$ [9, 58–64]. This is the so-called “cosmic string scaling solution”. String segments which are present between the time t_{eq} of equal matter and radiation and the present time t_0 and which our past light cone intersects produce wakes, overdense regions of dark matter and (after the time of recombination) baryons which lead to signatures in the large-scale structure of the Universe [22]. Since large-scale structure observations yield three-dimensional maps (position in the sky and redshift), they potentially contain more information than the two-dimensional CMB maps.

In this work, we will be interested in the signatures of the long cosmic string segments. Constraints on the string tension derived this way will be more robust than those which make use of assumptions about the distribution of string loops.

¹There are stronger limits which come from pulsar timing surveys [111, 112], but these depend on assumptions about the distribution of string loops which are not universally accepted.

The signatures of cosmic string wakes are highly non-Gaussian and have specific patterns in position space. Hence, position space-based algorithms will be more effective in searching for the signals of cosmic strings than traditionally used Fourier space techniques. Another advantage of working with position space analyses is that the resulting bounds on the string tension are less sensitive to the unknown number N than analyses operating in Fourier space. This is because we are looking for signals of individual strings (which are independent of N modulo superposition effects) rather than for signals in correlation functions (which depend strongly on N).

String wakes are nonlinear from the outset, while the fluctuations in the Standard Λ CDM model begin as Gaussian perturbations in the linear regime. On the other hand, at late times the non-linearities from the Λ CDM fluctuations become dominant [32]. Hence, searching for strings in high redshift data is, in principle, an easier avenue. For example, string wakes lead to narrow wedges in 21 cm redshift maps (at redshifts larger than that of reionization) with extra absorption [37]. On the other hand, data is harder to obtain at high redshifts, and the measurement errors are larger. Hence, a key goal is to probe down to which redshift any given statistic is able to extract wake signals for a fixed $G\mu$. In this work, we will study the distribution of dark matter. This could, in principle, be measured through weak lensing surveys. If baryons follow the dark matter distribution, then we could also probe the model predictions through large-scale galaxy redshift surveys and lower redshift 21cm studies.

At low redshifts, the density field is highly nonlinear on scales relevant to current cosmological observations of the distribution of galaxies. Hence, numerical simulations are required in order to study the predicted signals. In a recent work, a state-of-the-art N-body code [101] was extended to include the effects of a cosmic string wake [49]. These effects were added to the initial fluctuations from a Λ CDM cosmology. Results of runs with and without string wakes were compared, making use of a variety of specially designed statistics, and it was found that string wakes are identifiable for a string tension of $G\mu = 10^{-7}$ down to a redshift of $z = 7$. Wakes are nonlinear density perturbations present at arbitrarily early times with a distinctive geometric pattern in position space. In particular, the planar geometry of the wake suggests that such objects could be detected using 3D ridgelet statistics. In order to test this hypothesis, we analyzed part of the ridgelet spectrum of multiple simulated cosmic strings wakes in cosmological N-body simulations.

The conclusion of our analysis is the following. The full 3D ridgelet transform is hard

to compute as resolving a weak wake signal requires a very precise analysis. Since the ridgelet transform has four parameters, the time required to compute the transform scales as $\mathcal{O}(n^4)$ where n is the number of values probed in our analysis for a given parameter. This complicates the analysis on standard computers. However, a partial ridgelet transform analysis shows that a cosmic string of tension $G\mu = 10^{-7}$ can be detected at a high significance (5σ level) at a redshift of $z = 10$. This bound is competitive to what was obtained in [49].

The outline of this paper is as follows: In Sections 2 and 3, we present a brief review of cosmic string wakes and how they can be recreated in cosmological N-body simulations. Then, we discuss the 3D ridgelet transform and its implementation in cosmological N-body simulation in Section 4. Finally, we show how cosmic string wakes appear in ridgelet space in Section 5 and present our results for the detection of weak wake signals in Section 6. We use units of which the speed of light c is set to $c = 1$. We assume a homogeneous and isotropic cosmological background with vanishing spatial curvature and scale factor $a(t)$, where t is physical time. We set the scale factor to be $a(t_0) = 1$ at the present time t_0 . Thus, comoving lengths correspond to physical lengths today. The Hubble expansion rate is taken to be $h \times 100 \text{km s}^{-1} \text{Mpc}^{-1}$, where h is a constant.

7.2 Cosmic String Wake Formation

Space perpendicular to a long straight cosmic string segment is conical with a “deficit angle” [14] given by

$$\alpha = 8\pi G\mu. \quad (7.2.3)$$

For strings forming in a phase transition, this conical structure extends to a Hubble length from the string [98]. Hence, when a long string segment moves through a uniform matter distribution of the early universe, the matter behind the string acquires a velocity perturbation

$$\delta v = 4\pi v \gamma(v) G\mu \quad (7.2.4)$$

towards the plane spanned by the tangent vector to the moving string and the direction of motion, where v is the velocity of the string and $\gamma(v) = 1/\sqrt{1-v^2}$. This, in turn, leads to a wedge-shaped overdensity (density being twice the background density) behind the string, a “wake” [27, 28, 65, 66]. A cosmic string at the time t_i will lead to a wake with

comoving size

$$c_1 t_i \propto v \gamma(v) t_i \propto \delta v t_i, \quad (7.2.5)$$

where the factors are, from left to right, the length, the depth and the mean width of the wake. Here, c_1 is a constant of order 1. The geometry of the wake is shown in Figure 7.1.

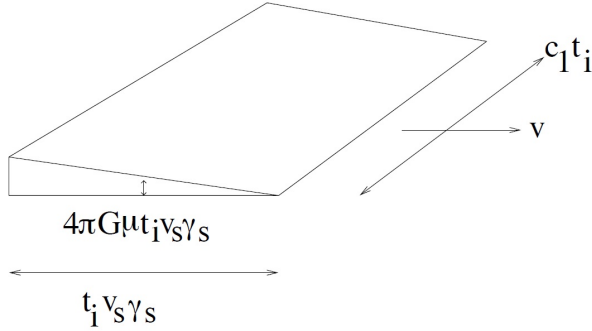


Figure 7.1 Geometry of a cosmic string wake [27, 28, 65, 66]. In the figure, v_s is the string velocity v , γ_s is the gamma factor $\gamma(v)$ and c_1 is a constant of order unity that depends on the length of the string.

Once formed, the cosmic string wake grows by gravitational accretion, which is studied using the Zel'dovich approximation [29]. The idea behind this approximation is to consider a thin shell of matter which is located initially at a physical height

$$H(t_i) = a(t_i)q \quad (7.2.6)$$

above the center of the wake, where t_i is the time when the wake is laid down. Here, $a(t_i)$ is the cosmological scale factor evaluated at time t_i and q is the initial comoving height. As a consequence of the gravitational pull of the matter overdensity inside the wake, a comoving displacement $\psi(t)$ gradually builds up (where $\psi(t_i) = 0$). The physical height at time $t > t_i$ then can be written as

$$H(q, t) = a(t)(q - \beta), \quad (7.2.7)$$

where β is a comoving displacement. If matter accretes via Newtonian gravity, the height of the wake at a later time is determined by

$$\ddot{H} = -\frac{\partial \Phi}{\partial H}, \quad (7.2.8)$$

where Φ is the Newtonian gravitational potential which is determined by the Poisson equation in terms of the mass overdensity. We then calculate the value $q(t)$ (which we call $q_{nl}(t, t_i)$) for which the shell stops growing in size at time t . This is given by

$$\dot{H}(q(t), t) = 0. \quad (7.2.9)$$

After this turnaround point, the shell virializes at a physical height which is half the value at its maximum. This virialized region forms the wake. For a cosmic string forming a perfectly straight line, the wake will take the form of a region of planar overdensity. This region of planar overdensity as a comoving height that grows linearly in the scale factor. As a result of a straight-forward computation, we obtain

$$q_{nl}(t, t_i) = \frac{a(t)}{a(t_i)} \frac{24\pi}{5} v\gamma(v) G\mu(z(t_i) + 1)^{-1/2} t_i, \quad (7.2.10)$$

which gives half the height the shell would have if it was simply expanding with the Hubble flow. Note that $z(t)$ is the cosmological redshift. Finally, the comoving planar dimension of the wake formed at time t_i is given by the comoving horizon at t_i , namely

$$d = z(t_i)^{-1/2} t_0. \quad (7.2.11)$$

A string segment only lives for one Hubble expansion time (before a string intersection occurs). However, since cosmic string wakes are made of accreted matter, they persist after the string segment has decayed. String wakes whose world sheet intersects the past light cone lead to an observable signal. The following section will explain how to recreate this signal in cosmological N-body simulations.

7.3 The Cosmological N-body simulations

The cosmological N-body simulations consist of a three-dimensional cubic box with a set of N points (representing equal mass particles) labeled by an index i represented by their coordinates \vec{x}_i and velocities \vec{v}_i . After setting up the initial distribution of points at redshift z_I (which is in general smaller than the redshift $z(t_i)$ when the wake is assumed to have been created), they are evolved using the Newtonian gravitational force equations to a later time t_w when a cosmic string wake is inserted. Once the wake is inserted, we once more

let the points in the box evolve according to Newtonian gravity to our current time while keeping track of the position and the velocity of the particles inside the box throughout the process. The simulations are described in more detail in [49]. In this section, we present information about the data boxes relevant to the analyses presented in Sections 5 and 6.

The simulations are produced with a public high-performance cosmological N-body code named CUBEP³M [101]. A data box is segmented in multiple cells and the number of particles per dimension introduced inside the box is chosen to be half the number of cells per dimension. To place the particles in the box, the initial conditions generator of the program reads a transfer function constructed with the CAMB online toolkit² and lays out a distribution of points corresponding to Λ CDM fluctuations [4] at the initial redshift z_I with the following cosmological parameters: $\Omega_\Lambda = 0.7095$, $\Omega_b = 0.0445$, $\Omega_{CDM} = 0.246$, $n_t = 1$, $n_s = 0.96$, $\sigma_8 = 0.8628$, $h = 0.70$ and $T_{CMB}(t_0) = 2.7255$. Here, Ω_Λ is the energy fraction of dark energy, Ω_b is the energy fraction of baryonic matter, Ω_{CDM} is the energy fraction of cold dark matter, n_t is the tensor spectral index, n_s is the scalar spectral index, σ_8 is the amplitude of the linear power spectrum on the scale of $8 h^{-1}\text{Mpc}$, h is the Hubble parameter and $T_{CMB}(t_0)$ is the temperature of the cosmic microwave background at our current time t_0 . Each particle inside the box has a distinct ID number associated to it which allows us to track its position inside the box. The initial redshift z_I is chosen at a point in time when the density fluctuations are in the linear regime.

As mentioned before, the particles move according to the gravitational interaction between them throughout the simulation. (See [101] for more information on how the gravitational attraction on each particle is computed.) The wake is introduced at a later time t_w after t_I . To produce a particle distribution corresponding to a wake overdensity, the particles are moved and given a velocity kick towards the central plane $y = 0 h^{-1}\text{Mpc}$ in the simulation box. The goal of this process is to simulate the velocity perturbation δv given by equation 7.2.4. We consider wakes laid down at the time of equal matter and radiation t_{eq} because they have had more time to grow in thickness than those created later, and since they are the largest among those present at t_{eq} . Since the comoving planar distance of such a wake, given by equation 7.2.11, is much bigger than the size of the simulation box, it is justified to insert the velocity perturbation as a planar perturbation. The exact magnitude of the velocities and displacements given to the particles are calculated according to the Zel'dovich approximation mentioned in the previous section, evolving the fluctuation from

²CAMB:https://lambda.gsfc.nasa.gov/toolbox/tb_camb_form.cfm

$t_i = t_{eq}$ to the time t_w of wake insertion. As a result of this computation, the comoving displacement $\psi(t)$ of the particles towards the plane at times $t > t_i$ is given by

$$\psi(t) = \frac{3}{5}4\pi G\mu v\gamma(v)t_i z(t_i) \frac{z(t_i)}{z(t)}. \quad (7.3.12)$$

The last factor represents the linear theory growth of the fluctuation while the other factor of $z(t_i)$ represent the conversion from physical to comoving velocity. The comoving velocity perturbation is

$$\dot{\psi}(t) = \frac{2}{5}4\pi G\mu v\gamma(v)t_i z(t_i) \frac{z(t_i)}{z(t)} \frac{1}{t}. \quad (7.3.13)$$

In the context of the simulations, the displacement and the velocity perturbation given to the particles towards the central plane $y = 0$ $h^{-1}\text{Mpc}$ are computed respectively from equation 7.3.12 and 7.3.13 at the time $t = t_w$ when the wake is inserted.

After the wake insertion, the modified data cube is evolved using CUBEP³M until redshift $z = 0$. This way, the behavior of the wake overdensity can be studied at lower redshift until it is completely disrupted by the other density fluctuations [32]. The next section will introduce the statistics used in order to study the wake overdensity.

7.4 The 3D Ridgelet Transform

Like the Fourier transform, which is an orthogonal projection of a function onto the space of phasors e^{ikx} , the 3D ridgelet transform [115] is an orthogonal projection of a function on the space of ridgelet functions $\Psi(\vec{x})$, which are wavelet functions ψ constant along a plane with normal vector

$$\vec{n}(\theta_1, \theta_2) = (\cos \theta_1 \sin \theta_2, \sin \theta_1 \sin \theta_2, \cos \theta_2). \quad (7.4.14)$$

Here, the angles $\theta_1 \in [0, 2\pi[$ and $\theta_2 \in [0, \pi[$ determine the orientation of the plane in spherical coordinates. For each plane with normal vector $\vec{n}(\theta_1, \theta_2)$, we can define the trivariate ridgelet function evaluated at \vec{x} by

$$\Psi_{a,b,\theta_1,\theta_2}(\vec{x}) = a^{-1/2} \psi \left(\frac{\vec{x} \cdot \vec{n}(\theta_1, \theta_2) - b}{a} \right), \quad (7.4.15)$$

where a , which satisfies $a > 0$, is a scale parameter and $b \in \mathbb{R}$ determines the position of the ridgelet function. Given an integrable trivariate function $f(\vec{x})$, its 3D ridgelet coefficients are defined by:

$$\mathcal{R}_f(a, b, \theta_1, \theta_2) = \int_{\mathbb{R}^3} f(\vec{x}) \Psi_{a,b,\theta_1,\theta_2}(\vec{x}) d\vec{x}, \quad (7.4.16)$$

Computing the ridgelet transform of a function means computing the ridgelet coefficients \mathcal{R}_f for all possible values of a , b , θ_1 and θ_2 , which constitutes the ridgelet space.

Given the planar geometry of the ridgelet function, the 3D ridgelet analysis can be constructed as a wavelet analysis in the Radon domain. In 3D, the Radon transform $\mathbf{R}(f)$ of f is the collection of hyperplane integrals indexed by the orientation (θ_1, θ_2) in spherical coordinates and a position coefficient $t \in \mathbb{R}$. The value of $\mathbf{R}(f)$ is given by

$$\mathbf{R}(f)(\theta_1, \theta_2, t) = \int_{\mathbb{R}^3} f(\vec{x}) \delta(\vec{x} \cdot \vec{n}(\theta_1, \theta_2) - t) d\vec{x}, \quad (7.4.17)$$

where δ is the Dirac delta function. Then, the 3D ridgelet transform is exactly the application of a 1D wavelet transform along the slices of the Radon transform where the orientation (θ_1, θ_2) is kept constant but t is varying:

$$\mathcal{R}_f(a, b, \theta_1, \theta_2) = \int \psi_{a,b}(t) \mathbf{R}(f)(\theta_1, \theta_2, t) dt, \quad (7.4.18)$$

where $\psi_{a,b} = \psi((t - b)/a)/\sqrt{a}$ is a 1-dimensional wavelet. Therefore, a good strategy for calculating the continuous ridgelet transform in 3D is to compute the Radon transform $\mathbf{R}(f)$ first and then apply a 1-dimensional wavelet to the slices defined by fixing the orientation (θ_1, θ_2) in $\mathbf{R}(f)$.

In order to define a way to perform a ridgelet transformation on the 3D data box which constitutes the cosmological N-body simulation, each point i at a position \vec{x}_i inside the box can be considered locally as a Dirac delta function in the energy density ρ . Using this representation, the local density $\rho(\vec{x})$ inside the box is given by

$$\rho(\vec{x}) = \sum_{i=1}^N \delta(\vec{x} - \vec{x}_i). \quad (7.4.19)$$

Here, the local density is normalized in a way that the total mass M of the particles in the box is a dimensionless quantity equal to the number N of particles in the box. This way,

each particle has a mass $m = 1$. To perform the Radon transform at a specific orientation (θ_1, θ_2) inside the box, it suffices to redefine the position of each point inside the box as their orthogonal projection $t_i(\theta_1, \theta_2) = \vec{x}_i \cdot \vec{n}(\theta_1, \theta_2)$ on a line spanned by $\vec{n}(\theta_1, \theta_2)$ passing through the center of the box. We obtain

$$\mathbf{R}(\rho)(\theta_1, \theta_2) = \sum_{i=1}^N \delta(t - t_i(\theta_1, \theta_2)). \quad (7.4.20)$$

Finally, each ridgelet coefficient can be computed using equation 7.4.18. The expression for the coefficients trivially reduces to

$$\mathcal{R}_\rho(a, b, \theta_1, \theta_2) = \sum_{i=1}^N \psi_{a,b}(t_i(\theta_1, \theta_2)). \quad (7.4.21)$$

A good choice of wavelet function ψ in the expression of $\psi_{a,b}$ is one that satisfies the following difference between two scaling functions ϕ :

$$\frac{1}{8}\psi\left(\frac{x}{2}\right) = \phi(x) - \frac{1}{8}\phi\left(\frac{x}{2}\right). \quad (7.4.22)$$

Here, the chosen scaling function ϕ is a B-spline of order 3:

$$\begin{aligned} \phi(x) = & \frac{1}{12}(|x - 2|^3 - 4|x - 1|^3 + 6|x|^3 \\ & - 4|x + 1|^3 + |x + 2|^3). \end{aligned} \quad (7.4.23)$$

The B-spline, defined by the equation above, is shown in Figure 7.2.

Each ridgelet coefficient has 4 independent parameters $a > 0$, $b \in \mathbb{R}$, $\theta_1 \in [0, 2\pi[$ and $\theta_2 \in [0, \pi[$. If we discretize ridgelet space into n intervals along each axis, then the time required to perform the ridgelet transformation grows as $\mathcal{O}(n^4)$. This also means that the time required to perform the ridgelet transformation grows as $\mathcal{O}(N^4)$ for a fixed value of n and a varying number of particles N . Therefore, the computation is very expensive for a high number of particles.

In order to analyze the cosmic string wake signature in ridgelet space, we will for the sake of simplicity restrict the numbers of unknown arguments in the ridgelet transformation. This will yield a bound on the string wake detection efficiency, as will be discussed in the

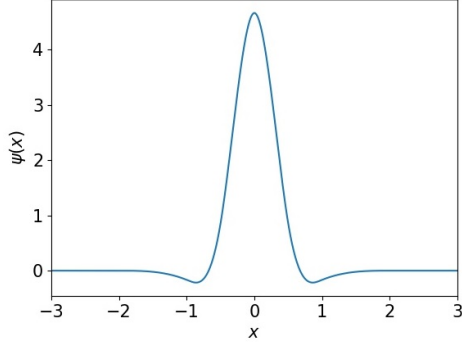


Figure 7.2 Plot of the wavelet function $\psi(x)$ in dimensionless units.

following section.

7.5 Plane Wakes signature in partial ridgelet transformations

The main idea behind using the 3D transform in order to detect cosmic string wakes is to find a subspace of the ridgelet space where the wake appears as a maximum in the ridgelet coefficients \mathcal{R}_ρ . A good way to do this is to perform the ridgelet transformation for a fixed value of the parameters a and b while varying the orientation (θ_1, θ_2) .

The values of a and b are chosen in a way that maximizes the ridgelet coefficients. Since the wake and the ridgelet function Ψ have planar geometry, we expect that the ridgelet coefficients \mathcal{R}_ρ , which are an inner product of the density ρ with Ψ , will be optimized for the parameters a , b , θ_1 and θ_2 that match the characteristic width and position of the wake. That is, we expect that a value of a close to the width of the wake, a value of b close to the position of the wake and an orientation (θ_1, θ_2) normal to the plane made by the wake will yield a maximum ridgelet coefficient. In our simulation, where the center of the box is at the origin and the wake is located on the z-x plane, this means that $b = 0 \text{ } h^{-1}\text{Mpc}$, $\theta_1 = \pi/2$, $\theta_2 = \pi/2$ and a value of a corresponding to the width of the wake should optimize the value of \mathcal{R}_ρ .

We tested this hypothesis using a data box which describes a $32 \text{ } h^{-1}\text{Mpc} \times 32 \text{ } h^{-1}\text{Mpc} \times 32 \text{ } h^{-1}\text{Mpc}$ cubic volume. The number of cells per dimension for the simulation and the number of particles per dimension in the box was respectively 512 and 256. The simulations started at redshift $z_I = 63$ and the wake produced by a cosmic string of string tension $G\mu = 10^{-6}$ was introduced at redshift $z = 7$. The 2D density contrast of the box on the

y-z plane at this redshift is shown in Figure 7.3. As we can see, the line overdensity visible

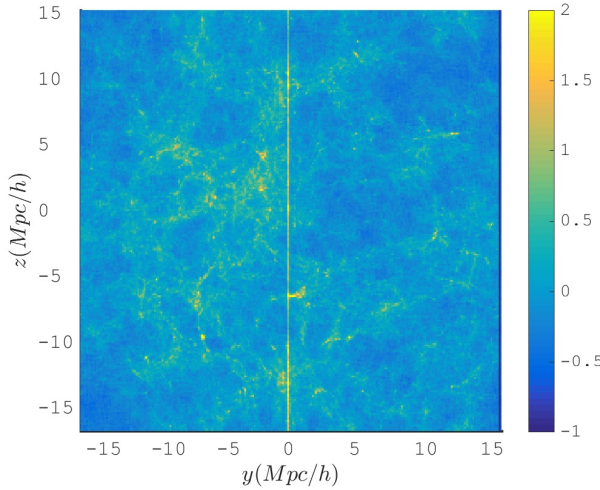


Figure 7.3 Density contrast of a 2D projection of the box on the y-z plane [49]. The $32 h^{-1}\text{Mpc} \times 32 h^{-1}\text{Mpc} \times 32 h^{-1}\text{Mpc}$ data box contains a cosmic string wake caused by a cosmic string of tension $G\mu = 10^{-6}$ at the position $y = 0 h^{-1}\text{Mpc}$ and the redshift $z = 7$. The color scheme, shown on the right, depicts the range of possible values for the fluctuation ratio $\delta S/S$. Here, S is the mean surface density and δS is the difference between the local surface density and the mean surface density.

at the position $y = 0 h^{-1}\text{Mpc}$ is in the non-linear regime which indicates the presence of the cosmic string wake.

The analysis was performed at the redshift of insertion of the wake ($z = 7$). Since the wake can move to another position at later redshift, this ensures that the wake is at the center of the box at the moment of the analysis. This position can be seen in the density projection of the box on the y-axis (see Figure 7.4), where the peak at the origin exposes the overdensity created by the wake. To find the value of a that maximises the ridgelet coefficients, we imposed the parameters $b = 0 h^{-1}\text{Mpc}$ and $\theta_1 = \theta_2 = \pi/2$ and studied the behavior of \mathcal{R}_ρ as the value of a was varied. A good way to do this is to plot the ratio of \mathcal{R}_ρ at a specific scale a with respect to the average of \mathcal{R}_ρ over all orientations. Assuming the ridgelet coefficients are described by $\mathcal{R}_\rho = \mathcal{R}_\rho(a, b, \theta_1, \theta_2)$, this ratio can be defined as

$$R(a) = \frac{\mathcal{R}_\rho(a, 0, \pi/2, \pi/2)}{\langle \mathcal{R}_\rho(a, 0, \theta_1, \theta_2) \rangle}, \quad (7.5.24)$$

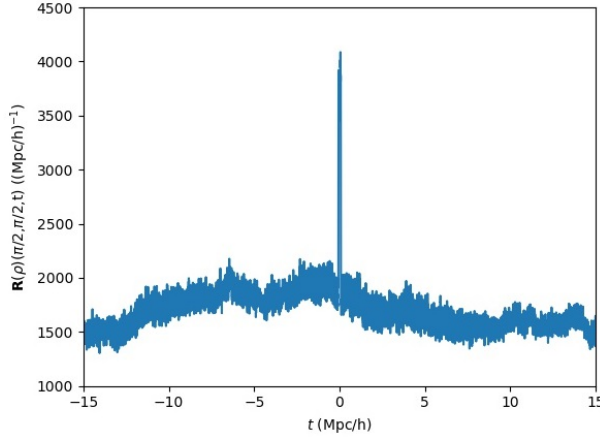


Figure 7.4 For a wake caused by a cosmic string of string tension $G\mu = 10^{-6}$ at redshift $z = 7$, the Radon transform $\mathbf{R}(\rho) = \mathbf{R}(\rho)(\theta_1, \theta_2, t)$ where $\theta_1 = \theta_2 = \pi/2$, is plotted for 10000 values of t between $-15 h^{-1}\text{Mpc}$ and $15 h^{-1}\text{Mpc}$. For this specific orientation and position, t corresponds to the y axis which gives us a density projection on the y axis. The width of the wake is $(1.1382 \pm 0.0003) \times 10^{-1} h^{-1}\text{Mpc}$, where the uncertainty is defined as half the distance between two evaluated values of t .

where $\langle \mathcal{R}_\rho(a, 0, \theta_1, \theta_2) \rangle$ is the mean value of \mathcal{R}_ρ with respect to the orientation (θ_1, θ_2) and a fixed value of a . For the present data box, the plot of this ratio is shown in Figure 7.5. As we can see, $R(a)$ as a maximum at $a_{max} = (1.168 \pm 0.006) \times 10^{-1} h^{-1}\text{Mpc}$. This value of a_{max} is close to the physical width of the wake. Therefore, it makes sense to fix a to the value of a_{max} for the partial ridgelet transformation.

At this point, there should be no doubt that $b = 0 h^{-1}\text{Mpc}$ is also a good parameter to fix. However, to ensure that $b = 0 h^{-1}\text{Mpc}$ yields a maximum coefficient in the ridgelet transformation, we plotted \mathcal{R}_ρ for $a = a_{max}$ and $\theta_1 = \theta_2 = \pi/2$ and varied b around the value of zero. As shown in Figure 7.6, the ridgelet coefficients have a maximum at $b_{max} = (0 \pm 8) \times 10^{-1} h^{-1}\text{Mpc}$. Since the uncertainty of b_{max} includes the value of zero, $b = 0 h^{-1}\text{Mpc}$ is a good fixed parameter. Finally, choosing $a = a_{max}$ and $b = 0 h^{-1}\text{Mpc}$ as fixed parameters, we can compute the partial ridgelet transformation. To avoid any edge effects that could be caused by the geometry of the box, we only consider the points inside the largest possible sphere centered on the wake inside the box. Then, we compute \mathcal{R}_ρ for n^2 orientations $(\theta_1, \theta_2) \in [0, \pi] \times [0, \pi]$. This process is shown in Figure 7.7. Here, the orientations are constrained to a hemisphere in order to avoid any unwanted periodicities in the ridgelet coefficients. The resulting subspace of the ridgelet space can be visualized

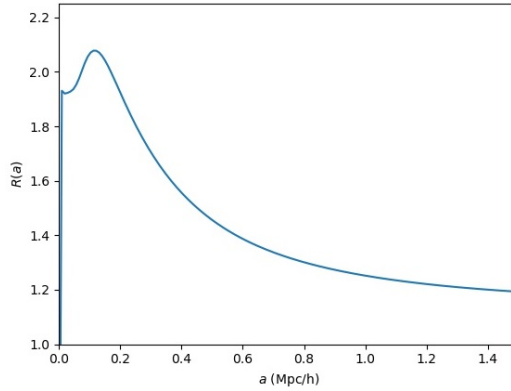


Figure 7.5 For a wake caused by a cosmic string of tension $G\mu = 10^{-6}$ at redshift $z = 7$, the ratio $R(a)$ is depicted for 1000 values of a between $0 h^{-1}\text{Mpc}$ and $1.5 h^{-1}\text{Mpc}$. The ratio has a maximum at $a_{max} = (1.168 \pm 0.006) \times 10^{-1} h^{-1}\text{Mpc}$, where the uncertainty is defined as half the distance between two evaluated values of a . As a becomes larger, $R(a)$ eventually converges to 1 as the wake signal becomes indistinguishable from the Gaussian fluctuations.

as a surface plot. As shown in Figure 7.8, the ridgelet coefficients have a clear maximum at $\theta_1 = \theta_2 = \pi/2$ which confirms our hypothesis that the parameters $a = a_{max}$, $b = 0 h^{-1}\text{Mpc}$ and $\theta_1 = \theta_2 = \pi/2$ maximise the ridgelet coefficients. Coincidentally, we can use this signal as a way to quantify at which level a cosmic string wake can be detected using ridgelet transformations. In order to do this, we compute the how much the maximum value of the ridgelet coefficients varies from its mean value, then compare this observable to the same maximum value in simulations where no wake is inserted. The steps are the following. Define the maximum fluctuation by

$$\delta\mathcal{R}_{\rho_{max}} = \mathcal{R}_{\rho_{max}} - \langle \mathcal{R}_\rho \rangle, \quad (7.5.25)$$

where $\mathcal{R}_{\rho_{max}}$ is the absolute maximum and $\langle \mathcal{R}_\rho \rangle$ is the mean value of the ridgelet coefficients over all orientations in the subspace that we have defined. Using this definition, we compute the maximum fluctuation for a simulation with a wake and multiple simulations without a wake for comparison. Then, a good measure of detection for the cosmic string wake is the confidence level \mathcal{C} which we define as

$$\mathcal{C} = \frac{s - \mu}{\sigma}. \quad (7.5.26)$$

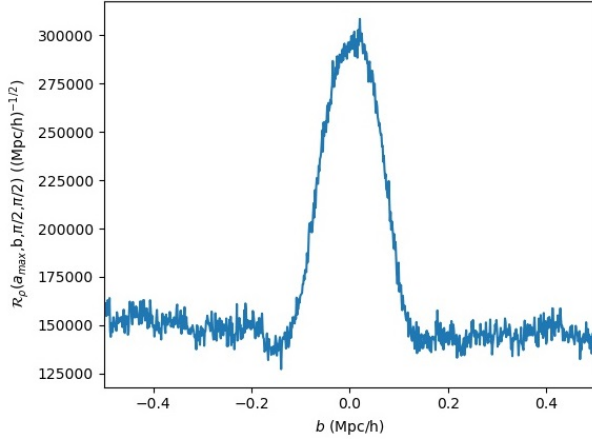


Figure 7.6 For a wake cased by a cosmic string of tension $G\mu = 10^{-6}$ at redshift $z = 7$, the ridgelet coefficients \mathcal{R}_ρ are plotted for 1000 values of b between $-0.5 h^{-1}\text{Mpc}$ and $0.5 h^{-1}\text{Mpc}$ while imposing that $a = a_{max}$, $\theta_1 = \theta_2 = \pi/2$. The ridgelet coefficients have a maximum at $b_{max} = (0 \pm 8) \times 10^{-1} h^{-1}\text{Mpc}$. The uncertainty is defined as half the width at half maximum of the peak.

Here, s is the maximum fluctuation for a simulation with a wake and μ and σ are respectively the mean and the standard deviation of the maximum fluctuations without a wake. This confidence level is the number of σ 's away from the mean of maximum fluctuations without wakes.

7.6 Weak plane wakes detection in partial ridgelet transformations

The method described in the previous section provides a way to detect wake signals which would not be visible by eye in the three-dimensional density maps. As discussed at the beginning of the paper, it is of interest to determine the lowest value of the string tension which can be detected in data at a particular redshift or to ask down to which redshift the string wake remains visible for a fixed value of the string tension. It is this second question which we study here. We fix the string tension to be $G\mu = 10^{-7}$, a value close to but below the current limit. We find that given the limited resolution of the simulations of the present study, string wakes remain identifiable down to a redshift of $z = 10$. We expect (as in the work of [49]) that with an improved resolution the string wake will remain visible to

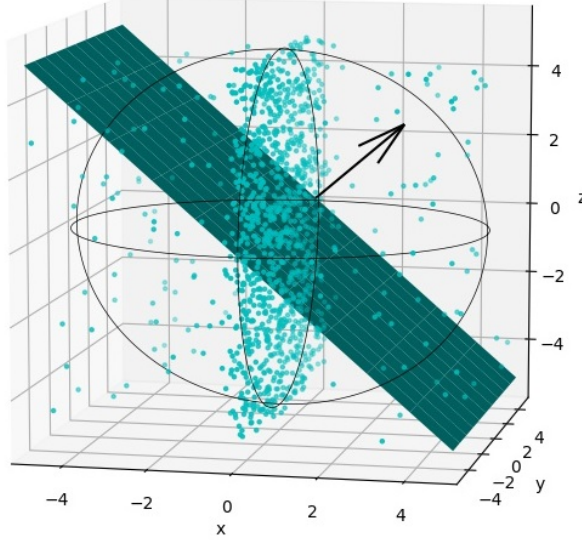


Figure 7.7 Sketch of the partial wavelet transformation. The ridgelet transform is computed inside a sphere the size of the box for different orientations $(\theta_1, \theta_2) \in [0, \pi] \times [0, \pi]$. The ridgelet function is constant along the planes normal to the direction vector $\vec{n}(\theta_1, \theta_2)$ shown in black. Therefore, we expect the ridgelet coefficients to be maximised when $\theta_1 = \theta_2 = \pi/2$; that is, when the plane with normal $\vec{n}(\theta_1, \theta_2)$ coincides with the plane formed by the wake.

a lower redshift.

We studied two sets of 4 data boxes which describe a $64 h^{-1}\text{Mpc} \times 64 h^{-1}\text{Mpc} \times 64 h^{-1}\text{Mpc}$ cubic volume. For both sets of simulations, the number of cells per dimensions for the simulations and the number of particles per dimension in the box was, respectively, 512 and 256, and the simulations started at redshift $z_I = 63$. In the first set of simulations, the perturbations from a wake produced by a cosmic string of string tension $G\mu = 10^{-7}$ was introduced at redshift $z = 31$. In the second set of simulations, no wake was introduced in the data box. The purpose of having a second set of simulations without wake was to expose and quantify the signal difference between a simulation with a wake and without a wake.

At redshift $z = 10$, the typical 2D density contrast of a data box where a cosmic string wake was introduced shows no wake signal which is observable by eye. This can be seen in Figure 7.9. Even though the wake signal cannot be observed in the 2D density projections, it can be extracted using ridgelet statistics. In contrast to the example in the previous section where we study the wake at the time of insertion, we now study it at a later time.

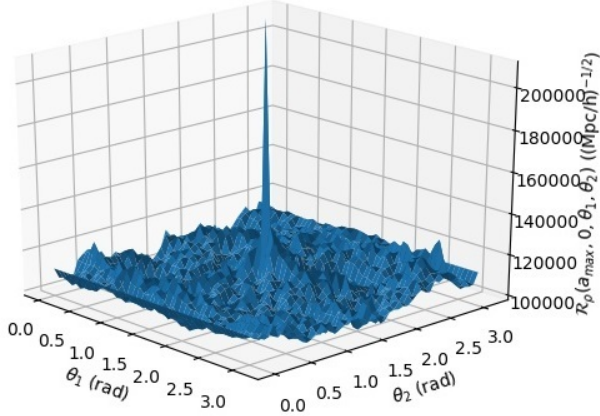


Figure 7.8 Surface plot of \mathcal{R}_ρ for $a = a_{max}$, $b = 0 h^{-1}\text{Mpc}$ and 50^2 orientations $(\theta_1, \theta_2) \in [0, \pi[\times [0, \pi[$. The plot has a clear maximum at $\theta_1 = \theta_2 = \pi/2$ for a wake cased by a cosmic string of string tension $G\mu = 10^{-6}$ at redshift $z = 7$.

The wake slightly moves in position along the y-axis between the time when it is inserted ($z = 31$) and the time at which it is studied ($z = 10$). In order to track the position of the wake between different redshifts, we index the ID of each particle in the overdensity made by the wake at $z = 31$. Then, we let the system evolve to lower redshift while highlighting the interval in which the points in the initial overdensity are situated. This process is shown in Figure 7.10. For the set of 4 simulations where the effects of a cosmic string are introduced, the mean value of the wake position at $z = 10$ is $(0.1 \pm 0.8)h^{-1}\text{Mpc}$ which is consistent with the fact that the wake is inserted in the middle of the box at $y = 0 h^{-1}\text{Mpc}$.

Once the wake is localized, the rest of the analysis is done on the points inside a sphere of radius of approximately $30 h^{-1}\text{Mpc}$ centered on the wake. To make sure that the wake was well centered in the sphere, we plotted the Radon transformation of this sphere for the fixed orientation $\theta_1 = \theta_2 = \pi/2$ in order to obtain the density projection of the sphere on the y-axis. Then, the density projection on the y-axis was fitted to a second-degree polynomial. As shown in Figure 7.11, the studentized residuals of the fit exposes a peak at the center which confirms the presence of the wake at the center of the sphere for one of the simulations that were studied. For the set of 4 simulations where a wake was introduced, the average measured width of the region of the peak was $(4.8 \pm 0.7) \times 10^{-2}h^{-1}\text{Mpc}$. In comparison, the same density projection for the box without the wake has no region of overdensity which confirms the presence of the wake in the data box and its location.

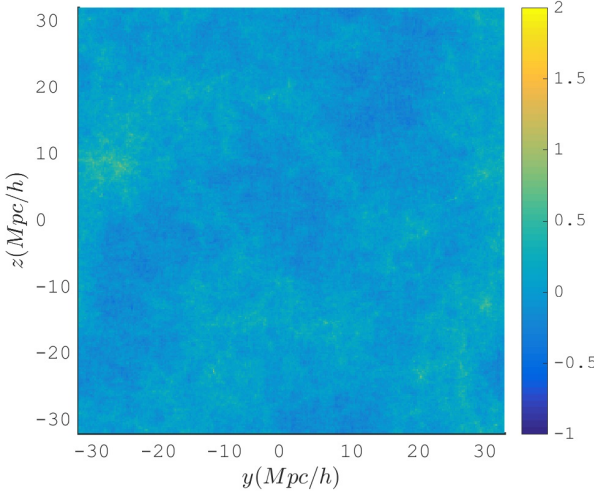


Figure 7.9 Density contrast of a 2D projection of the box onto the y - z plane at redshift $z = 10$ [49]. The $64 h^{-1}\text{Mpc} \times 64 h^{-1}\text{Mpc} \times 64 h^{-1}\text{Mpc}$ data box contains a wake caused by a cosmic string of tension $G\mu = 10^{-7}$ at the position $y = 0 h^{-1}\text{Mpc}$. The color scheme, shown on the right, shows the range of possible values for the fluctuation ratio $\delta\rho/\rho$ (ρ being the density). The wake is not visible by eye.

In order to find the scale a_{max} corresponding to the wakes, we fixed the position parameter b at the center of the sphere ($b = 0 h^{-1}\text{Mpc}$) for $\theta_1 = \theta_2 = \pi/2$ and plotted the ratio $R(a)$ for the set of data boxes with a wake and the set of boxes without the wake. The mean value of the plots for the set of data boxes with a wake and the set of data boxes without a wake is shown in Figure 7.12. The ratios for the data box with the wake show a maximum at $a_{max} = (1.7 \pm 0.1) \times 10^{-2} h^{-1}\text{Mpc}$. Conversely, the ratios for the data without the wake (in red) stay close to 1. Therefore, we conclude that $a_{max} = 1.7 \times 10^{-2} h^{-1}\text{Mpc}$ is a good fixed parameter for the scale parameter a . Also, Figure 7.12 gives us information on the range of scale parameters a which allow the wake to be detected when compared to a set of simulations without a wake. Indeed, if the lower bound on the mean of $R(a)$ for the data boxes with a wake is higher than the upper bound on the mean of $R(a)$ for the data boxes without a wake, we expect to be able to detect the wake for the given value of a . In this case, we would be able to detect the wake for a value of a lower than $0.90 h^{-1}\text{Mpc}$, which is where the bounds of the two curves meet in Figure 7.12.

To ensure that $b = 0 h^{-1}\text{Mpc}$ is a good parameter to impose for the Ridgelet transformation, we plotted \mathcal{R}_ρ for $a = a_{max}$ and $\theta_1 = \theta_2 = \pi/2$ and different values of b . The

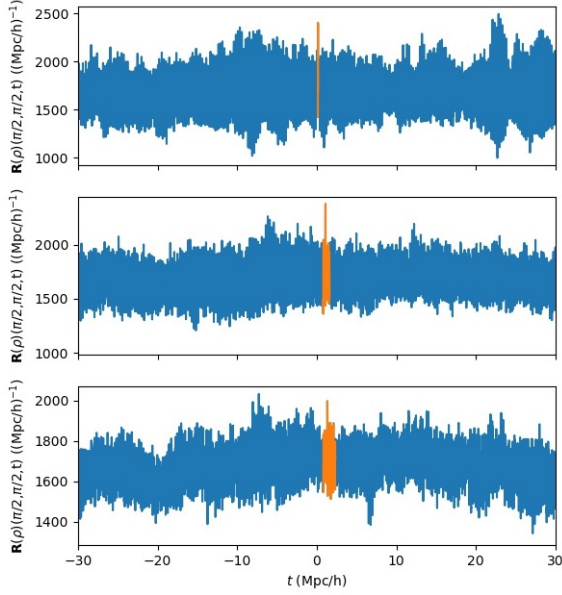


Figure 7.10 For a wake caused by a cosmic string of string tension $G\mu = 10^{-7}$ introduced at redshift $z = 31$ at the center of the box in the x - z plane, the Radon transform $\mathbf{R}(\rho) = \mathbf{R}(\rho)(\theta_1, \theta_2, t)$ where $\theta_1 = \theta_2 = \pi/2$, is plotted for 10000 values of t between $-32 h^{-1}\text{Mpc}$ and $32 h^{-1}\text{Mpc}$. For this specific orientation and position, t corresponds to the y axis which gives us a density projection onto the y -axis. The orange region shows how points in the original wake spread in the density projection at lower redshifts.

mean value of \mathcal{R}_ρ for the set of data boxes with a wake and the set of data boxes without a wake is shown in Figure 7.13. On average, the ridgelet coefficients have a maximum at $b_{max} = (-4 \pm 4) \times 10^{-3} h^{-1}\text{Mpc}$. This agrees with the fact that $b = 0 h^{-1}\text{Mpc}$ should maximize the ridgelet coefficients. Therefore, $b = 0 h^{-1}\text{Mpc}$ is a good fixed parameter. In the same way as Figure 7.12, Figure 7.13 gives us information on the range of position parameters b which allow the wake to be detected when compared to a set of simulations without a wake. This range of values, marked by dashed black lines in the figure, goes from $-0.01 h^{-1}\text{Mpc}$ to $0.01 h^{-1}\text{Mpc}$.

Finally, choosing $a = a_{max}$ and $b = 0 h^{-1}\text{Mpc}$ as fixed parameters, we computed the partial ridgelet transformation for each data box with a wake and each data box without a wake. The result is shown in Figure 7.14 for one round of simulations with and without wakes. For each simulation, the ridgelet coefficients of the data box with the wake have a maximum at $\theta_1 = \theta_2 = \pi/2$. On average, the confidence level was $\mathcal{C} = (6.8 \pm 0.9)\sigma$ for the

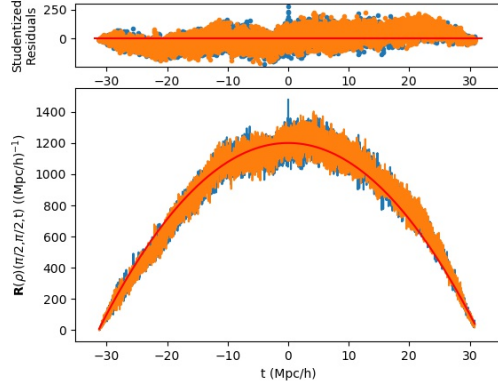


Figure 7.11 For a wake caused by a cosmic string of string tension $G\mu = 10^{-7}$ at redshift $z = 10$, the Radon transform of the data box with a wake (in blue) and without a wake (in orange) is plotted for 10000 values of t between $-32 h^{-1}\text{Mpc}$ and $32 h^{-1}\text{Mpc}$ for the fixed orientation $\theta_1 = \theta_2 = \pi/2$. The Radon transform is fitted to as a second degree polynomial shown in red. The studentized residuals reveal the presence of a small region of overdensity at $t = 0 h^{-1}\text{Mpc}$ in the blue plot which is not found in the orange plot. We conclude that this region of overdensity is caused by the wake.

simulations with a wake. This confirms that the weak signal observed was indeed created by the cosmic string wake.

7.7 Conclusions and Discussion

We have applied 3D ridgelet transformations to output data from cosmological N-body simulations in which the effects of a cosmic string wake have been added to the standard ΛCDM fluctuations. The goal of our study was to determine down to which redshifts the wake signals remain visible for a string tension of $G\mu = 10^{-7}$, a tension slightly lower than the current upper bound. Given the limited resolution of our simulations, we found that the string signals can be extracted down to a redshift of $z = 10$. These results were reached by comparing the output data of N-body simulations with and without the effects of the string wake on the positions and velocities of the dark matter particles in the simulations. We expect that with higher resolution simulations, the string signals remain visible to slightly lower redshifts. Our results are based on statistical analyses of a two-dimensional subspace of ridgelet coefficients, the other two having been fixed by independent considerations. An

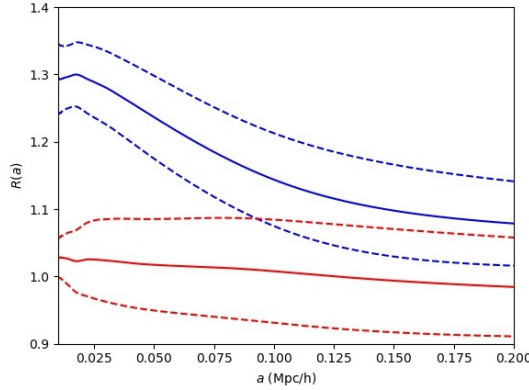


Figure 7.12 For a wake caused by a cosmic string of string tension $G\mu = 10^{-7}$ at redshift $z = 10$, the mean value of the ratio $R(a)$ is plotted for 3000 values of a between $0.01 h^{-1}\text{Mpc}$ and $0.20 h^{-1}\text{Mpc}$. The dashed lines show the standard deviation with respect to the means. The mean ratio for the data boxes is plotted in blue while the mean ratios for the data boxes without wakes are plotted in red.

analysis of the full four-dimensional space of ridgelet coefficients will likely yield stronger limits.

Our simulations yield the distribution of the dark matter. This could be probed observationally using weak lensing surveys. In order to compare with galaxy or quasar redshift surveys, our simulations would have to be extended with a halo-finding algorithm. On the other hand, we have seen that the wake signals rapidly get swamped by the non-Gaussianities due to the ΛCDM fluctuations. Hence, it may be more promising to study cosmic string signals in 21cm surveys at redshifts approaching that of reionization.

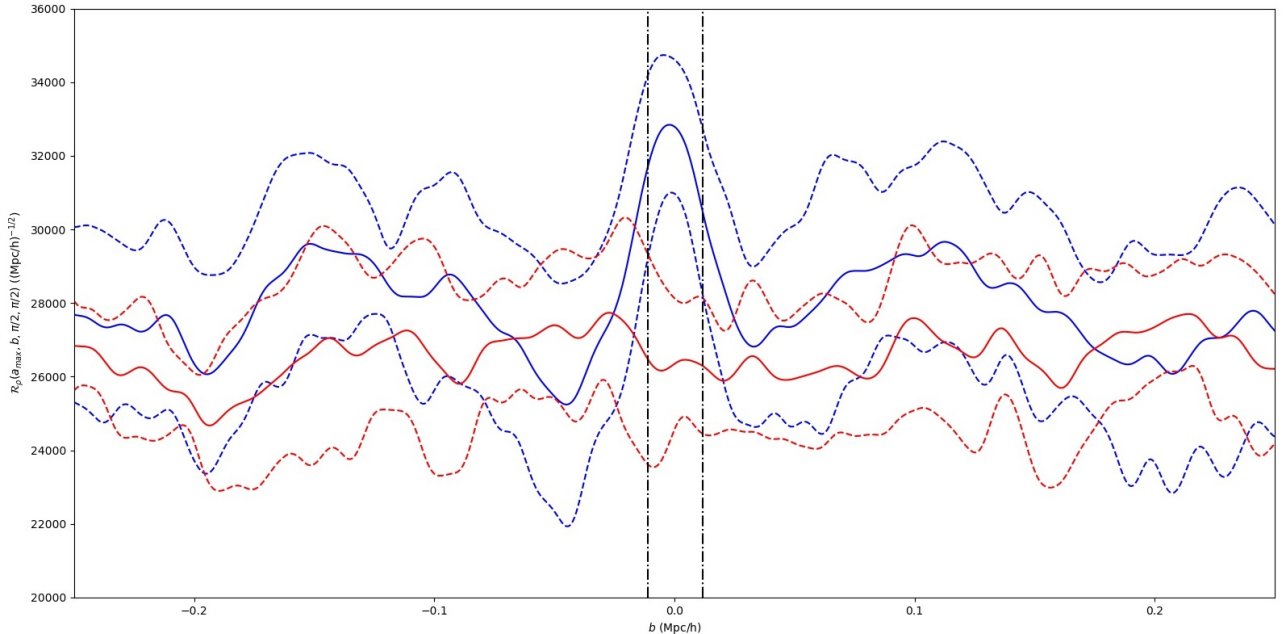


Figure 7.13 For a set of data boxes with a wake caused by a cosmic string of string tension $G\mu = 10^{-7}$ at redshift $z = 10$ (in blue) and a set of data boxes without wake (in red), the mean ridgelet coefficients \mathcal{R}_ρ are plotted for 1000 values of b between $-0.25 h^{-1}\text{Mpc}$ and $0.25 h^{-1}\text{Mpc}$ while imposing that $a = a_{max}$, $\theta_1 = \theta_2 = \pi/2$. The dashed lines show the standard deviation with respect to the means and the vertical black lines show the interval in which the peak caused by the wake can be detected when compared to a set of simulations without wakes.

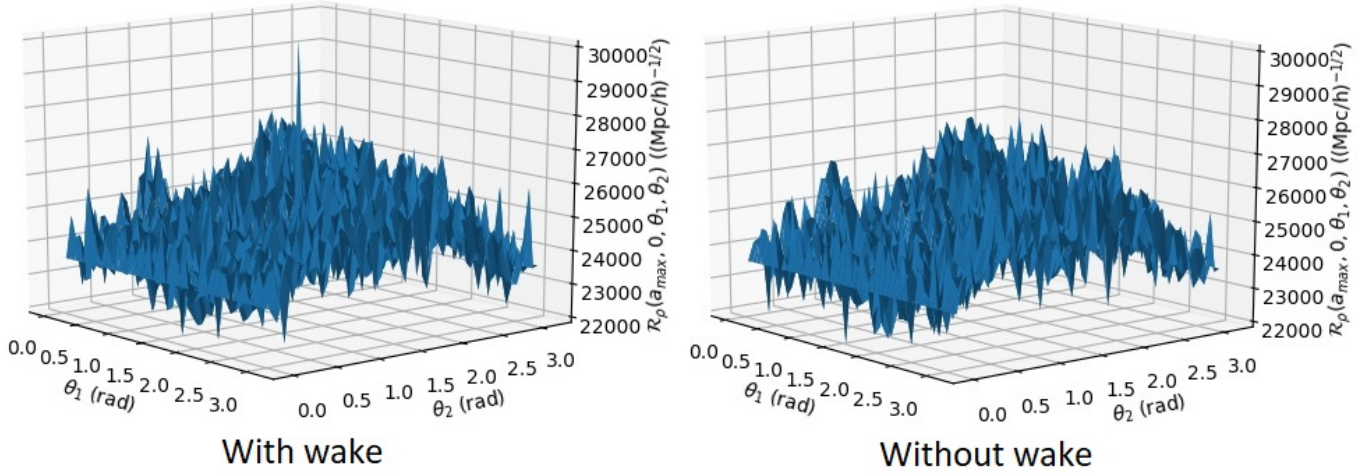


Figure 7.14 Surface plot of \mathcal{R}_ρ for the data box with the wake caused by a cosmic string of string tension $G\mu = 10^{-7}$ at redshift $z = 10$ (on the left) and without a wake at the same redshift (on the right). In both cases, the values of the ridgelet coefficients are computed for $a = a_{max}$, $b = 0 h^{-1}\text{Mpc}$ and 50^2 orientations $(\theta_1, \theta_2) \in [0, \pi[\times [0, \pi[$. For this example of data box with a wake, the coefficients have a clear maximum at $\theta_1 = \theta_2 = \pi/2$. This maximum is not observable in the coefficients of the data box without a wake. Therefore, we conclude that the maximum in the ridgelet coefficients on the left plot is indeed caused by the wake.

Chapter 8

Signature of a Cosmic String Wake at $z = 3$

8.1 Introduction

Cosmic strings are linear topological defects in Quantum Field Theory which exist as solutions in some models that go beyond the Standard Model of Particle Physics [15, 56]. A cosmic string consists of a one-dimensional region of trapped energy, having significant gravitational effects for cosmology. If a model of nature admits cosmic string solutions, strings will necessarily form during the early universe [94, 95]. For example, in some models, they form after the end of inflation, and in others, they form during a phase transition in the early radiation phase of Standard Big Bang Cosmology. After the cosmic strings form, they will persist as a scaling network. This means that the network of cosmic strings will have the same properties at all times if we scale the length observables to the Hubble radius [94, 95]. The network will consist of a few long strings moving near the speed of light and also of loops of different sizes, and it will source sub-dominant fluctuations at all times. The gravitational effects of a cosmic string are characterized by only one number μ , its tension, which does not affect the scaling solution properties of the cosmic string network. The tension can also be seen as the energy per unit of length of the cosmic string, and it is related to the energy scale η at which the strings form by the following equation:

$$G\mu \simeq (\eta/m_{pl})^2 \quad (8.1.1)$$

where G is Newton's constant and m_{pl} is the Planck mass. The presence of cosmic strings does not produce acoustic oscillation features on the Cosmic Microwave Background (CMB) angular power spectrum. This fact contributes to the current upper bound ¹ on the cosmic string tension [25]:

$$G\mu \approx 1.5 \times 10^{-7} \quad (8.1.2)$$

A good study on the observational aspects of cosmic strings has two possible outputs [57]. One possibility is observing a cosmic string, which would be a significant achievement on probing particle physics models beyond the Standard Model of Particle Physics. The other option is not to observe cosmic strings, which will lower the bound on the cosmic string tension, thus ruling out classes of particle physics models. Besides this, cosmic strings could produce interesting results for cosmology such as explaining the origin of Fast Radio Bursts [116], primordial magnetic fields [117], and the origin of supermassive black holes [118].

This work will concentrate on the Large Scale Structure (LSS) as a complementary (in addition to the CMB) arena for probing cosmic string. The primary motivation is that LSS data contains three-dimensional information, which includes many more modes than the two-dimensional maps from the CMB. The disadvantage of LSS is that the effects of non-linearities are essential, so theoretical predictions are harder to be obtained.

In a recent paper [49] (see also [50]) we began a study of the dark matter distribution induced by string wakes [27, 28, 65, 66] inserted at $z = 31$, using a simulation box of lateral size $L = 64Mpc/h$ and $np = 512$ particles per dimension. We found that the string signals for a wake with a string tension of $G\mu = 10^{-7}$ can be identified down to a redshift of $z \geq 10$. A possible cause for not being able to identify the wake at lower redshifts comes from the fact that the wake thickness was about one order of magnitude smaller than the resolution length of the simulation grid at the time of wake insertion. The fact that the wake survives down to redshift $z = 10$ supports the idea that the wake global signal remains present despite losing its local signal [32]. In the current work, we take a complementary

¹Note that there are stronger limits on the string tension which comes from limits on the stochastic background of gravitational waves on length scales which the pulsar timing arrays are sensitive to (see e. g. [112]). These bounds come from gravitational radiation from string loops, and assume a scaling distribution of string loops where the total energy in strings is dominated by the loops [9, 58–64]. However, field theory cosmic string simulations [20] do not yield a significant distribution of string loops. Thus, bounds on the cosmic string tension from gravitational radiation from string loops are less robust than the ones coming from the long strings.

approach, and we use a box with a small lateral size (of $L = 4Mpc/h$) and a higher number of particles ($np = 1024$ particles per dimension), so the wake becomes well-resolved. The downside of this approach is that we lose part of the global wake signal, and the advantage is that the effect of the wake lasts for more time.

A cosmic string wake is a planar overdense region that forms behind a long string as it passes by the matter distribution [27, 28, 65, 66]. This effect is a consequence of the fact that a space perpendicular to the long string will have a missing angle given by $\alpha = 8\pi G\mu$ [11, 15], causing two test dark matter particles initially at rest to receive a velocity kick towards behind the string as soon as it passes by between the two. The expression for the velocity perturbation is the following:

$$\delta v = 4\pi\gamma_s v_s G\mu \quad (8.1.3)$$

where v_s is the transverse velocity of the string and γ_s is the associated Lorentz factor. The velocity kick makes the particles meet behind the string, forming a wedge-like structure with two times the average matter density. This is the wake. The initial geometry of the wake after formation at $t = t_{wf}$ will be a box of volume V , consisting of two large planar dimensions of the order of the Hubble radius $\approx t_f$ and one smaller thickness with a length of the order of the Hubble radius multiplied by the deficit angle:

$$V \approx t_f \times t_f v_s \gamma_s \times 4\pi G\mu t_f v_s \gamma_s \quad (8.1.4)$$

At early times it is possible to obtain an analytical understanding of the wake evolution thanks to the fact that the matter fluctuation outside the wake was in the linear regime. The Zeldovich approximation [29] gives the evolution of the comoving wake thickness ψ_3 as a function of redshift z [30, 31] :

$$\psi_3 = \frac{24\pi}{5} G\mu v_s \gamma_s t_0 \frac{\sqrt{1 + z_{eq}}}{(1 + z)} \quad (8.1.5)$$

where t_0 is the present time and z_{eq} is the redshift of matter and radiation equality. Note that the wake produces a nonlinear density fluctuation at arbitrarily early times. Since structures start to grow only after the time of equal matter and radiation, we choose this time as the time for wake formation (so we will consider $t_f = t_{eq}$). We use the value

$z_{eq} = 1000$. As the thickness grows as in linear theory, the planar dimension increases just with the Hubble flow, and are fixed in comoving coordinates. For the formation time we are considering, the planar dimension of the wake is about $\approx 100 Mpc$. If the analytical thickness evolution remains valid up to today, we would have wakes with the thickness of $\approx 0.1 Mpc$ at present (for $G\mu = 1 \times 10^{-7}$).

Once the ΛCDM perturbations enter the nonlinear regime (at about the time of reionization), the local mass distribution in the wake becomes highly nonlinear, the ΛCDM fluctuations will disrupt the wake [32], and the subsequent dynamics has to be studied numerically. In this paper, we simulate cosmic string wakes using an N-body code called CUBEP3M [101] and apply a statistic that extracts the wake signal.

The paper is organized as follow: Section II contains a discussion on the previous works regarding wake evolution in the nonlinear regime; Section III describes the simulations performed in the present work, and the analysis of the data described in section III is performed in section IV; Finally, in section V we summarize the essential results obtained and indicate experimental prospects and possible paths for an extension of the analysis.

8.2 Review of Cosmic string wakes in the non-linear regime

The wake produces a planar non-linear density perturbation at arbitrarily early times, so early on the wake is unambiguously distinguishable from ΛCDM fluctuations. Once the ΛCDM fluctuations start to dominate, nearby halos begin to accrete material from the wake, causing wake fragmentation. An analytical study regarding the wake disruption by ΛCDM fluctuations was presented in [32], where two criteria for wake disruption were introduced. The first one concerns local stability, which was studied by considering a cubic box with the dimension of the wake thickness and computing the standard deviation of the density contrast in this region from ΛCDM fluctuations. The second criterion takes the global extension of the wake region into account, by computing the standard deviation of the density contrast from ΛCDM inside a box with dimension V (see (8.1.4)) given by the whole wake. Both conditions were computed, and the main result indicates that although a $G\mu = 10^{-7}$ wake could be locally disrupted at $z \approx 8$ it could in principle be distinguished from ΛCDM fluctuations at all times using the global information of the wake.

A method used to extract the wake signal from the dark matter distribution was presented in [49] and can be summarized as follows: for any direction of the sphere, we consider

an associated projection axis passing through the origin of the box. We then consider slices of the simulation box perpendicular to that axis at each point x of this axis with thickness given by the grid size of the simulation, and we compute the mass density $\delta(x)$ of dark matter particles in that slice as a function of x . A one-dimensional filter wavelet analysis is then performed on the mass density $\delta(x)$, giving a filtered version of it, called $f\delta$. We then compute the maximum value S of $f\delta(x)$ for each direction (pair of spherical angles) in the simulation box. S is a map on the surface of the sphere (which represent the spherical angles), and \hat{S} is its maximum value. The signal to noise ratio for the spherical peak($\max(S)$) divided by standard deviation ($\max(S)/\text{std}(S)$) distribution for ten simulations without wake and three simulations with a $G\mu = 10^{-7}$ wake was found to be $\bar{\mathcal{R}} = 8.1$ at redshift $z = 10$ and insignificant at lower z .

The setup of the N-body simulation is the following. We used an N-body simulation program called CUBEP³M, a public high performance cosmological N -body code based on a two-level mesh gravity solver augmented with sub-grid particle-particle interactions [101]. This code generates and evolves initial conditions (which are realizations of Λ CDM fluctuations) containing positions and velocities of particles inside a cubic box. There is an option to save the phase space of the distribution at any redshift and rerun the code from this checkpoint. We use this feature for wake insertion, by modifying the saved phase space distribution at time t_i by including effects of a wake. The modification consists in displacing and giving a velocity kick to particles towards the wake plane. The absolute value of the displacement $\psi(t_i)$ and velocity perturbation $\dot{\psi}(t_i)$ in comoving units can be computed using the following equations (see [30, 31] for details)

$$\psi(t_i) = \frac{3}{5} 4\pi G \mu v_s \gamma_s t_{eq} z(t_{eq}) \frac{z(t_{eq})}{z(t_i)}. \quad (8.2.6)$$

and

$$\dot{\psi}(t_i) = \frac{2}{5} 4\pi G \mu v_s \gamma_s t_{eq} z(t_{eq}) \frac{z(t_{eq})}{z(t_i)} \frac{1}{t_i}. \quad (8.2.7)$$

Once the wake insertion is made, the new modified distribution is further evolved by the N-body code.

The primary goal of this paper is to find a statistic which can extract the wake presence without using information about the simulation without a wake. In the next section, we will describe the simulations in more detail.

8.3 Simulations

We performed six N-body simulations without wakes with the following cosmological parameters: $\Omega_\Lambda = 0.7095$, $\Omega_b = 0.0445$, $\Omega_{\text{CDM}} = 0.246$, $n_t = 1$, $n_s = 0.96$, $\sigma_8 = 0.8628$, $h = 0.70$, $T_{\text{cmb}}(t_0) = 2.7255$. Those simulations consists of $np = 1024$ particles per dimension, a lateral size of $L = 4\text{Mpc}/h$, and initial conditions generated at $z = 31$, with checkpoints at $z = 15$, $z = 10$, $z = 7$, $z = 5$ and $z = 3$. The wake is inserted at the $z = 10$ checkpoint. All simulations used 512 cores divided into 64 MPI tasks and were run in the Graham Cluster of Calcul Quebec, part of the Compute Canada consortium.

As pointed out in [32], if we displace all particles towards a central plane, this creates a nonphysical void on the parallel planes at the boundary of the simulation box. Here we circumvent this problem by using a suppression of the velocity and displacement perturbations that starts halfway between the wake and the boundary and linearly decreases to zero at the boundary. This procedure avoids the creation of a planar void at the boundary since the particles are not displaced there.

Figure 8.1 shows the average displacement induced by the wake on each particle and compares it with the analytical prediction. As in the previous work, the numerical simulation results for the wake-induced displacement are about a factor of two higher than the analytical prediction. We conjectured that this could be due to the nonphysical void, but here it is evident that this was not the case since there is no void in our new simulations. This fact indicates that the analytical prediction is incomplete, and we should trust more in the numerical simulations. Another reason is that we are in the non-linear regime, where the assumptions of the analytical predictions are not valid. Also, the analytical prediction assumes a late time matter-dominated cosmology, whereas the numerical work is done in the context of a ΛCDM background. The analytical prediction should be modified for the cosmological constant dominated period. We plan to do that in the future.

A similar analysis was done for the induced velocity perturbation. As figure 8.2 shows, the difference between the numerical and analytical velocity perturbations is not significant.

8.4 Analysis

The wake presence is not clear if we compare the visualization of a two-dimensional projection for a pure ΛCDM simulation with a ΛCDM plus wake simulation. Figure 8.3

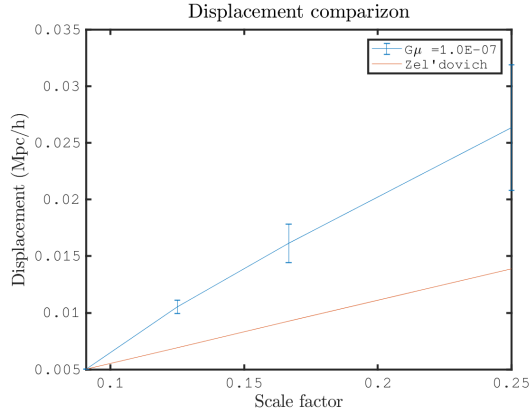


Figure 8.1 Average displacement induced by the wake (in blue), compared with the analytical prediction (in red).

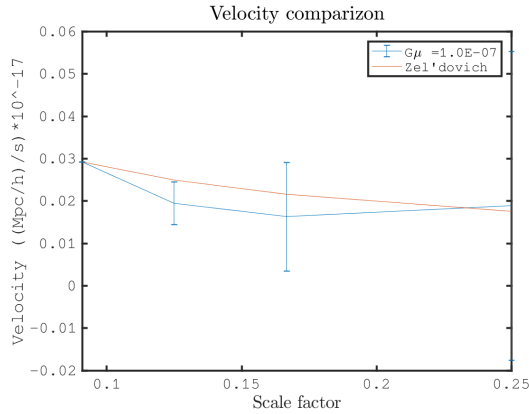


Figure 8.2 Average velocity perturbation induced by the wake (in blue), compared with the analytical prediction (in red).

illustrates this at $z = 3$. Both figures show the density contrast of logarithm of two-dimensional projections of the dark matter distribution (in simulation units). The upper figure contains just ΛCDM fluctuations, and the bottom figure contains the same ΛCDM fluctuations plus a $G\mu = 10^{-7}$ wake. A trained eye could perceive that a wake is located at the plane $Z \approx 2 Mpc/h$ which under projection appears as a vertical line at the middle of the panel (since we are projecting onto a plane perpendicular to the wake plane). It was not possible to find a good statistics that extracts the wake signal for such projections.

This occurs because the Gaussian fluctuations displace the particles on the wake, and these particles no longer form a straight plane. However, the wake can be better recovered if we project not the entire x direction, but several slices of it. It was found that if we

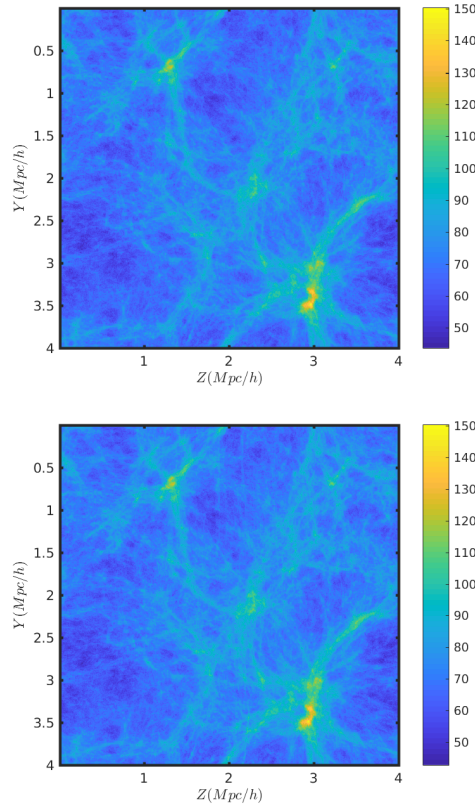


Figure 8.3 Logarithm of the mass of a two-dimensional projection of simulation particles for lateral size $L = 4Mpc/h$ and redshift $z = 3$. The upper plot shows the simulation without the wake, and the plot on the bottom shows the simulation with a $G\mu = 10^{-7}$ wake at the central position of the z axis.

slice the x direction in 32 different parts and perform a two-dimensional projection on each slice, the wake can be better visualized. Figure 8.4 shows the slice number 31 associated with the same simulations of figure 8.3. The wake presence is more explicit in this case and corresponds to a clear vertical line at the middle of the panel on the bottom figure of 8.4.

Unfortunately, this does not mean that wake detection is granted since the wake presence should be obtained quantitatively and without previous knowledge of the simulation without a wake.

In the next subsection, we will show the result of a statistic that analyses a set of two-dimensional projections of the dark matter particles. We ask the question if it is possible to differentiate the images of the two-dimensional projections perpendicular to the wake

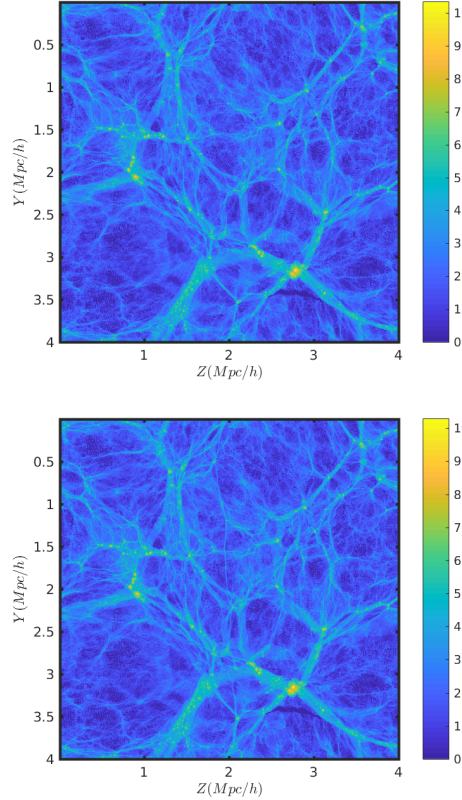


Figure 8.4 Logarithm of the mass of a two-dimensional projection of a slice of the simulation box with lateral size $L = 4Mpc/h$ and redshift $z = 3$. The upper plot shows the slice without the wake, and the plot on the bottom shows the slice with a $G\mu = 10^{-7}$ wake at the central position of the z axis.

from any other projection without the wake.²

A sky map with a specific redshift layer can be further subdivided into several square images (using small angle approximation), and in a universe with a cosmic string network, there is a small non-zero probability that one of those images has a wake perpendicular to it. We will see that this small fraction is still sufficient to pinpoint a universe with $G\mu = 10^{-7}$ cosmic strings at redshift down to $z = 3$.

² One motivation for this approach is that some experiments, like SKA [119, 120] have a poor redshift resolution compared with the angular resolution, so the data set can be better viewed as layers of two-dimensional intensity maps with each layer corresponding to a redshift range.

8.4.1 A curvelet filtering of the two-dimensional projections

Here we describe the pipeline for the statistics that we use for wake detection. All computations were performed using Matlab, together with the curvelet package CURVELAB [121]. We will also use ridgelet transformation [122], which detects straight lines (ridges) which cross an entire image. Similarly, the curvelet base functions are line segments, which can be seen as a local version of the ridges.

The first of the filtering procedure step is, for each cubic simulation box, to slice it into 32 different tiles (where the slice is perpendicular to the x direction, while the wake is parallel) and to obtain a two-dimensional map of it by projecting the associated slice onto the $y - z$ plane.

For each two-dimensional dark matter map particle number (which is proportional to the dark matter mass) pn (viewed as a two-dimensional array with the projected number of particles as each one of its elements) we perform the following steps:

- 1-) Compute the logarithm of the dark matter mass $pn_{log} = \log(1 + pn)$. The number one is added for the result to be strictly positive.
- 2-) Compute the curvelet-filtered transformation $curv(s, w, i, j) = C(pn_{log})$, where s corresponds to the scale of the ridge, w to the angle, i and j to the positions. All the curvelet coefficients with scales higher than the expected wake thickness were set to zero.
- 3-) A wake ridge corresponds to coefficients that are much higher than the others if we fix the position, scale and allow the angles to vary. Therefore we would like to highlight the maximum of the function $f_{s,i,j}(w) = curv(s, w, i, j)$ in the angle variable w . We implement that for each (s, i, j) by multiplying the function $g(w) = f_{s,i,j}(w)$ by its own density contrast $\tilde{g}(w) = (g(w) - \bar{g})/\bar{g}$, where $\bar{g} = mean(g(w))$. The resulting new wavelet coefficient becomes $\tilde{f}_{s,i,j}(w) = f_{s,i,j}(w) \times \tilde{g}(w)$.
- 4-) After the previous filter, the inverse curvelet transformation is taken and $dm_{2d} = curv^{-1}(\tilde{f}_{s,i,j}(w))$.

Once the 32 filtered images are computed, we combine them together again in a three-dimensional map dm_{3d} , where one of the dimension corresponds to the direction of slicing (and go from one to 32) and the remaining two dimensions are the labels for the filtered image pixels. The image of each slice corresponds to the filtered image obtained in the steps above for each one of the slices.

- 5-) Compute a 3d curvelet decomposition $curv3d = C(dm_{3d})$, and set the negative

coefficients to zero. The motivation for this threshold is to consider just planar over-density detection in the image since the negative curvelet coefficients represent planar under densities (or planar voids, which are not important for us). After that, we do the inverse curvelet transformation. This procedure will also highlight pixels with high density that are next to each other. By doing the inverse curvelet transformation, we obtain 32 filtered slices $dmFilt(i, j, k) = C^{-1}(curv3d)$ from the original 32 slices, where i and j range from 1 to 1024 and k range from 1 to 32.

Steps 3 and 5 are crucial since they highlight line segment discontinuities (as produced by the wake). To see this, consider figure 8.5 which shows the result of the fifth step for the maps of figure 8.4. The wake presence is clear now, with a large line segment on the bottom panel indicating the wake position.

6-) Perform a ridgelet transformation [122] on each slice $rad_k(l, a) = R(dmFilt_k(i, j))$, where k indicates the slice, l the position of the ridge, a its angle and $dmFilt_k(i, j) = dmFilt(i, j, k)$ its image before the ridgelet transformation. A ridgelet transformation is suitable for detection such as the ones produced by the wake.

7-) The wake statistical signal indicator $s(k) = pk(k)/std(k)$ of the slice k is the peak $pk(k) = \max(rad_k(l, a))$ divided the standard deviation $std(rad_k(l, a))$ of the Radon transformation, where $\max(rad_k(l, a))$ denotes the maximum value of the two dimensional array $rad_k(l, a)$ (with respect to (l, a)) and $std(rad_k(l, a))$ denotes the standard deviation of the same array $rad_k(l, a)$ (also with respect to (l, a)). A high peak means that there is a line in the two-dimensional map with high contrast, such as the one produced by the wake.

8-) Finally, take the sum of $s(k)$ as the wake indicator statistical signal of the $(4Mpc/h)^3$ volume. The wake presence will increase each one of the $s(k)$ systematically, so that is why we take their sum as the wake signal S :

$$S = \sum_k s(k) \quad (8.4.8)$$

The analysis above is applied in two different situations: in the first one, the orientation of the wake is used as prior information, and in the second situation, this information is not used beforehand. Each case will be described in the next two subsections.

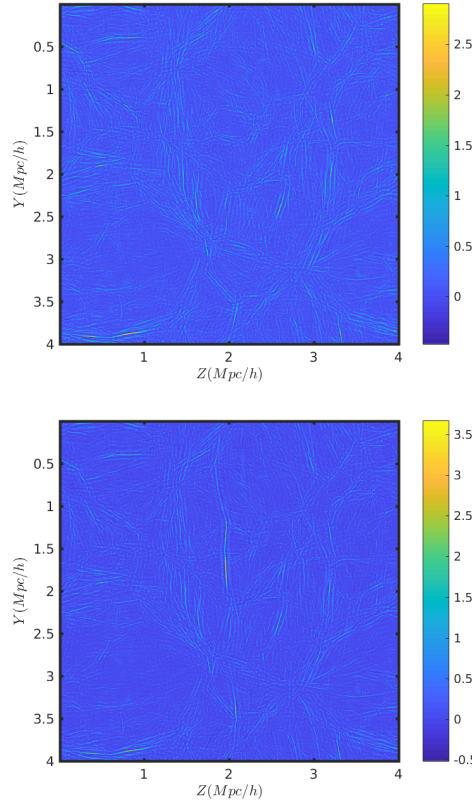


Figure 8.5 Filtered version of the logarithm of the mass of a two-dimensional projection of a slice of the simulation box with lateral size $L = 4Mpc/h$ and redshift $z = 3$. The upper plot shows the slice without the wake, and the plot on the bottom shows the slice with a $G\mu = 10^{-7}$ wake at the center.

8.4.2 Wake signal extraction with wake orientation prior

We have inserted the wake at the plane $Z = 2Mpc/h$. Therefore, by choosing the axis x as the projection axis for our analysis, we will be automatically selecting an axis perpendicular to the wake plane and therefore, will have an optimal statistical analysis.

For each simulation and orientation aligned with the wake, we chose the wake indicator S from 8.4.8. The result of the distribution of the signal S for each one of the ten simulations (with and without wakes) is shown in figure 8.6.

This statistic has a confidence level of $\bar{R} = 9.9$, where $\bar{R} = mean(R)$ is the mean of the

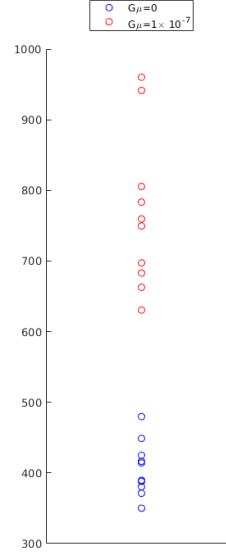


Figure 8.6 Distribution of the wake indicator S for the wake simulations (in red), and with pure ΛCDM (in blue).

signal to noise ratio for the wake simulation, defined as

$$R = \frac{S - \bar{S}_{nw}}{std(S_{nw})} \quad (8.4.9)$$

where S is computed for a given simulation with a wake, \bar{S}_{nw} is the mean S of all simulations without wakes and $std(S_{nw})$ is the standard deviation of all S from simulations without a wake. \bar{R} is the mean of R for all simulations with wakes.

8.4.3 Wake signal extraction without wake orientation prior

In this subsection, we consider various orientations for the two-dimensional projections, without introducing the wake orientation information beforehand. For choosing different angular orientations, we consider a Healpix set of spherical angles [105], which give equally-spaced adjacent spherical angles. In addition to considering different orientations, we also take advantage of the periodic boundary condition and perform random displacements and rotations on the two-dimensional figures, so the wake line does not lie on the $z = 2Mpc/h$ plane anymore. By choosing the parameter $N_{side} = 8$ for the Healpix scheme, we can

survey $N_{\text{angles}} = 384$ different projecting angles for each simulation (we are considering just non-antipodal angles since they produce equivalent two-dimensional projections). Figure 8.7 shows an example for one of the simulations of a sphere in which each point is a pair of spherical angles, and the color specifies the value of the wake indicator S for that orientation.

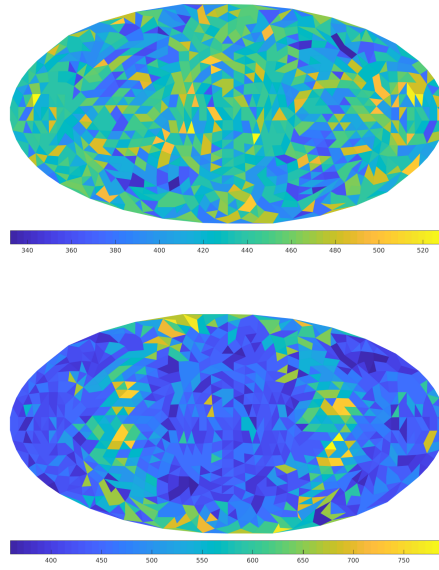


Figure 8.7 Wake indicator S values for different orientations for a simulation box with lateral size $L = 4 \text{Mpc}/h$ and redshift $z = 3$. The upper plot shows the spherical map without the wake, and the plot on the bottom shows the spherical map with a $G\mu = 10^{-7}$ wake.

If we consider the wake indicator S value for all angles of the ten samples, we can construct the histogram of figure 8.8, which shows the histograms for both the wake case and also for the no wake case.

There are 10 outliers with $S > 532$ for the histogram without wakes and 833 outliers for the histograms with wakes. We choose $S_t = 532$ as a threshold that indicates the wake presence. In principle, we could have chosen a higher threshold, such as $S = 590$, where there is just one outlier for the histogram without wake, and we would obtain better results (because the probability of finding such an outlier would be much smaller). But we want to construct our statistics based not in only one point, which could lead to a non-robust result. Therefore if in a pure ΛCDM universe a random set of 32 dark matter

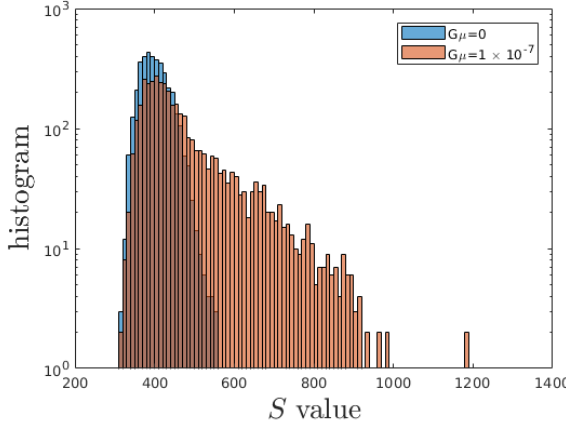


Figure 8.8 Histogram in logarithmic scale of the S values for all 384 angles and ten simulation boxes with lateral size $L = 4Mpc/h$ and redshift $z = 3$. The blue histogram correspond to the simulations without wakes, and the red histogram correspond to $G\mu = 10^{-7}$ wakes.

maps of $(4Mpc/h)^2$ with a resolution of 1024^2 at redshift $z = 3$ is taken in the sky, the probability of it to have $S > 532$ is $p_{nw} \approx 10/3840 = 0.0026$. We would naively expect that the probability of finding a similar $S > 532$ dark matter maps for a universe with wakes would be $\approx 833/3840 = 0.2169$, but that is not true, since not every map of this kind will intercept a wake. With the simplest (and most conservative) assumption that in a ΛCDM plus cosmic string universe there is just one long string per Hubble volume, we would expect that only a fraction of about $1/24 = 4Mpc/95Mpc$ of the boxes (95 Mpc corresponds to the comoving Hubble radius at wake formation) would contain a wake, so we have to multiply the previous probability estimation by this factor. Therefore the expected probability of finding a similar $S > 532$ dark matter map would be $p_w \approx 0.2169 * (1/24) = 0.0090$, which is 3.4 higher than in the no wake case.

We will assume that we can cover one-quarter of all angles in the entire dark matter sky, so we have about $N = 10^4$ dark matter maps similar to the ones we are, and for each one of them, we would find one wake indicator S value. Multiplying this number N by the probability of finding $S > 532$ outliers we expect to obtain $N_{nw} = 26$ outliers in a universe without wakes and $N_w = 90$ outliers in a universe with cosmic string wakes. With this result now we can know what is the probability of discarding the null hypothesis that our universe is pure ΛCDM in favor of an alternative hypothesis that our universe contains a network of $G\mu = 10^{-7}$ cosmic strings. The probability of a universe with wakes to have

more than 45 (this is half the expected one, chosen to be sure the probability is very close to one) outliers from the N quantities discussed above is very close to one (by one part in 10^7). On the other hand, the probability of having more than 45 outliers in a pure ΛCDM universe is 4.5594×10^{-4} , which is a p-value equivalent to 4 sigmas of confidence level.

We showed above that it is possible to identify the presence of cosmic string wakes of $G\mu = 10^{-7}$ at $z = 3$ with a confidence level of four sigmas if a set of three-dimensional dark matter maps covering one-quarter of the sky is given. Each map should consist of 32 consecutive slices (with respect of the field of view, and having $4Mpc/h$ of depth) of $(4mpc/h)^2$ squares with 1024 pixels per dimension. We argued that with the most simplistic assumptions of one wake per Hubble volume, there would be 90 outliers indicating the wake presence, whereas there will be 26 outliers in the case of a universe without cosmic string wakes.

8.5 Conclusion

With this work, we can affirm that a sky map of the dark matter distribution can be used to constrain the existence of cosmic strings with high statistical significance. It is worth mentioning that the values used to construct this argument are conservative ones, and increasing then (the number of maps in the sky (N), the wake indicator threshold $S_t = 532$, the number of outliers 45 and the number of long cosmic strings per Hubble volume (here taken as one)) will give better results than quoted in this paper.

We are investigating whether neural networks could improve the wake detection. The hope is that they will be able to distinguish maps with and without wakes at redshifts below $z = 3$ and lower string tension parameter.

The experimental prospects to find the wake signal will be analyzed in future works, where resolution (angular and redshift) is essential together with intensity sensitivity. Finally, it remains to be seen if the dark matter tracers, such as halos and galaxies, will maintain the wake signal. All of those aspects are under current investigation.

Chapter 9

Conclusion

Cosmic strings are objects that are generated in many theories that go beyond the SMPP characterized by a simple parameter, namely their tension. Therefore constraining this parameter is an important way to see which of these models are acceptable and can be further studied or must be discarded. The CMB power spectrum is the traditional window for constraining the cosmic string parameter which is already complemented by a real-spaced based approaches, giving similar results. Contemporary cosmology starts to have extensive data sets available on the three-dimensional distribution of matter, which in principle will contain much more power to constrain models since three-dimensional maps encode more information than two-dimensional ones, opening the possibilities for better testing fundamental physics using cosmological data.

The present thesis is devoted to finding strategies to search for effects of cosmic strings on the LSS. Motivated by the fact that a cosmic string creates a wake with a planar over-density pattern, locally changing the distribution of dark matter, developing specific pipelines that show how to extract this signal is a fundamental step toward a realistic forecast. This step will make it possible to constrain the cosmic string parameter using LSS experiments, such as 21-cm or optical surveys.

The first important conclusion that can be drawn from this thesis is that although wakes will be locally indistinguishable from other usual Λ *CDM* overdense regions, they will still imprint a unique global characteristic that is unlikely to appear from usual Λ *CDM* fluctuations. This conclusion opens the possibility to study the wake in the non-linear regime, where the analytical predictions cease to be reliable.

The second important conclusion is that, beyond the existence of a wake of cosmic string signal in the LSS, there exists a method for extracting this wake signal. More than just a proof-of-concept this study confirmed the first conclusion above that albeit the wake is locally disrupted, it is still reliably present in the dark matter distribution. In order to show this, a novel threshold method was implemented on the curvelet coefficients.

The present work can be extended in many directions. Inspired by similar works on CMB cosmic string detection in position space, a possible fruitful venue would be to use artificial intelligence methods, alongside with hybrid methods. The most important challenge would be to extend the two-dimensional pipelines to three-dimensions.

The options above will point towards an optimal statistic for wake detection. Armed with what was presented regarding curvelet analysis, it is already possible to forecast what constraints experiments would give for the cosmic string tension. Both 21 cm intensity maps (like SKA and HERA) and optical (such as EUCLID and WFIRST) experiments are suitable for this task.

Bibliography

- [1] W. L. Freedman, B. F. Madore, B. K. Gibson, L. Ferrarese, D. D. Kelson, S. Sakai, J. R. Mould, R. C. Kennicutt, Jr., H. C. Ford, J. A. Graham, J. P. Huchra, S. M. G. Hughes, G. D. Illingworth, L. M. Macri, and P. B. Stetson, "Astrophys. J." **553**, 47 (2001), astro-ph/0012376 .
- [2] Y. Akrami *et al.* (Planck), (2018), arXiv:1807.06205 [astro-ph.CO] .
- [3] N. Aghanim *et al.* (Planck), (2018), arXiv:1807.06209 [astro-ph.CO] .
- [4] S. Dodelson, *Modern Cosmology* (Academic Press, Amsterdam, 2003).
- [5] S. Sarangi and S. H. H. Tye, Phys. Lett. **B536**, 185 (2002), arXiv:hep-th/0204074 [hep-th] .
- [6] R. H. Brandenberger, in *String Cosmology*, J. Erdmenger (Editor). Wiley, 2009. p.193-230 (2008) pp. 193–230, arXiv:0808.0746 [hep-th] .
- [7] T. W. B. Kibble, J. Phys. **A9**, 1387 (1976).
- [8] M. Hindmarsh, J. Lizarraga, J. Urrestilla, D. Daverio, and M. Kunz, Phys. Rev. **D99**, 083522 (2019), arXiv:1812.08649 [astro-ph.CO] .
- [9] J. J. Blanco-Pillado, K. D. Olum, and B. Shlaer, Phys. Rev. **D83**, 083514 (2011), arXiv:1101.5173 [astro-ph.CO] .
- [10] C. J. A. P. Martins and E. P. S. Shellard, Phys. Rev. **D54**, 2535 (1996), arXiv:hep-ph/9602271 [hep-ph] .
- [11] A. Vilenkin and E. P. S. Shellard, *Cosmic Strings and Other Topological Defects* (Cambridge University Press, 2000).
- [12] E. W. Kolb and M. S. Turner, Front. Phys. **69**, 1 (1990).
- [13] H. B. Nielsen and P. Olesen, Nucl. Phys. **B61**, 45 (1973), [,302(1973)].
- [14] A. Vilenkin, Phys. Rev. **D23**, 852 (1981).

- [15] R. H. Brandenberger, *Int. J. Mod. Phys. A***9**, 2117 (1994), arXiv:astro-ph/9310041 [astro-ph].
- [16] A. Vilenkin and A. E. Everett, *Phys. Rev. Lett.* **48**, 1867 (1982).
- [17] E. Witten, *Phys. Lett.* **153B**, 243 (1985).
- [18] E. J. Copeland, R. C. Myers, and J. Polchinski, *JHEP* **06**, 013 (2004), arXiv:hep-th/0312067 [hep-th].
- [19] T. Vachaspati and A. Vilenkin, *Phys. Rev. D***30**, 2036 (1984).
- [20] M. Hindmarsh, S. Stuckey, and N. Bevis, *Phys. Rev. D***79**, 123504 (2009), arXiv:0812.1929 [hep-th].
- [21] A. Vilenkin, *Phys. Rev. Lett.* **46**, 1169 (1981), [Erratum: *Phys. Rev. Lett.* **46**, 1496 (1981)].
- [22] R. H. Brandenberger, *Proceedings, 9th International Symposium on Cosmology and Particle Astrophysics (CosPA 2012): Taipei, Taiwan, November 13-17, 2012*, *Nucl. Phys. Proc. Suppl.* **246-247**, 45 (2014), arXiv:1301.2856 [astro-ph.CO].
- [23] J. Magueijo, A. Albrecht, D. Coulson, and P. Ferreira, *Phys. Rev. Lett.* **76**, 2617 (1996), arXiv:astro-ph/9511042 [astro-ph].
- [24] A. Albrecht, D. Coulson, P. Ferreira, and J. Magueijo, *Phys. Rev. Lett.* **76**, 1413 (1996), arXiv:astro-ph/9505030 [astro-ph].
- [25] C. Dvorkin, M. Wyman, and W. Hu, *Phys. Rev. D***84**, 123519 (2011), arXiv:1109.4947 [astro-ph.CO].
- [26] P. A. R. Ade *et al.* (Planck), *Astron. Astrophys.* **571**, A25 (2014), arXiv:1303.5085 [astro-ph.CO].
- [27] J. Silk and A. Vilenkin, *Phys. Rev. Lett.* **53**, 1700 (1984).
- [28] A. Stebbins, S. Veeraraghavan, R. H. Brandenberger, J. Silk, and N. Turok, *Astrophys. J.* **322**, 1 (1987).
- [29] Ya. B. Zeldovich, *Astron. Astrophys.* **5**, 84 (1970).
- [30] R. H. Brandenberger, L. Perivolaropoulos, and A. Stebbins, *Int. J. Mod. Phys. A***5**, 1633 (1990).
- [31] L. Perivolaropoulos, R. H. Brandenberger, and A. Stebbins, *Phys. Rev. D***41**, 1764 (1990).

- [32] D. C. N. da Cunha, O. F. Hernández, and R. H. Brandenberger, Phys. Rev. **D93**, 123501 (2016), arXiv:1508.02317 [astro-ph.CO] .
- [33] N. Kaiser and A. Stebbins, Nature **310**, 391 (1984).
- [34] J. D. Jackson, *Classical Electrodynamics* (Wiley, 1998).
- [35] U.-L. Pen, U. Seljak, and N. Turok, Phys. Rev. Lett. **79**, 1611 (1997), arXiv:astro-ph/9704165 [astro-ph] .
- [36] R. J. Danos, R. H. Brandenberger, and G. Holder, Phys. Rev. **D82**, 023513 (2010), arXiv:1003.0905 [astro-ph.CO] .
- [37] R. H. Brandenberger, R. J. Danos, O. F. Hernandez, and G. P. Holder, JCAP **1012**, 028 (2010), arXiv:1006.2514 [astro-ph.CO] .
- [38] S. Furlanetto, S. P. Oh, and F. Briggs, Phys. Rept. **433**, 181 (2006), arXiv:astro-ph/0608032 [astro-ph] .
- [39] S. Amsel, J. Berger, and R. H. Brandenberger, JCAP **0804**, 015 (2008), arXiv:0709.0982 [astro-ph] .
- [40] R. J. Danos and R. H. Brandenberger, JCAP **1002**, 033 (2010), arXiv:0910.5722 [astro-ph.CO] .
- [41] R. J. Danos and R. H. Brandenberger, Int. J. Mod. Phys. **D19**, 183 (2010), arXiv:0811.2004 [astro-ph] .
- [42] J. Schmalzing, M. Kerscher, and T. Buchert, *Dark matter in the universe. Proceedings, 132nd course of the International School of Physics *Enrico Fermi**, Varenna, Italy, July 25-August 4, 1995, Proc. Int. Sch. Phys. Fermi **132**, 281 (1996), arXiv:astro-ph/9508154 [astro-ph] .
- [43] T. Buchert, M. J. France, and F. Steiner, Class. Quant. Grav. **34**, 094002 (2017), arXiv:1701.03347 [astro-ph.CO] .
- [44] E. McDonough and R. H. Brandenberger, JCAP **1302**, 045 (2013), arXiv:1109.2627 [astro-ph.CO] .
- [45] B. K. Spears, J. Brase, P.-T. Bremer, B. Chen, J. Field, J. Gaffney, M. Kruse, S. Langer, K. Lewis, and R. Nora, Physics of Plasmas **25**, 080901 (2018), arXiv:1712.08523 [physics.comp-ph] .
- [46] R. Ciuca and O. F. Hernández, JCAP **1708**, 028 (2017), arXiv:1706.04131 [astro-ph.CO] .

- [47] R. Ciuca, O. F. Hernández, and M. Wolman, *Mon. Not. Roy. Astron. Soc.* **485**, 1377 (2019), arXiv:1708.08878 [astro-ph.CO] .
- [48] J.-L. Starck, F. Murtagh, and J. Fadili, *Sparse Image and Signal Processing: Wavelets, Curvelets, Morphological Diversity* (Cambridge University Press, New York, NY, USA, 2010).
- [49] D. C. Neves da Cunha, J. Harnois-Deraps, R. Brandenberger, A. Amara, and A. Refregier, *Phys. Rev. D* **98**, 083015 (2018), arXiv:1804.00083 [astro-ph.CO] .
- [50] S. Laliberte, R. Brandenberger, and D. C. N. da Cunha, (2018), arXiv:1807.09820 [astro-ph.CO] .
- [51] D. C. N. da Cunha, (2018), arXiv:1810.07737 [astro-ph.CO] .
- [52] J. D. McEwen, S. M. Feeney, H. V. Peiris, Y. Wiaux, C. Ringeval, and F. R. Bouchet, *Mon. Not. Roy. Astron. Soc.* **472**, 4081 (2017), arXiv:1611.10347 [astro-ph.IM] .
- [53] L. Hergt, A. Amara, R. Brandenberger, T. Kacprzak, and A. Refregier, *JCAP* **1706**, 004 (2017), arXiv:1608.00004 [astro-ph.CO] .
- [54] A. Vafaei Sadr, S. M. S. Movahed, M. Farhang, C. Ringeval, and F. R. Bouchet, *Mon. Not. Roy. Astron. Soc.* **475**, 1010 (2018), arXiv:1710.00173 [astro-ph.CO] .
- [55] A. Vafaei Sadr, M. Farhang, S. M. S. Movahed, B. Bassett, and M. Kunz, *Mon. Not. Roy. Astron. Soc.* **478**, 1132 (2018), arXiv:1801.04140 [astro-ph.CO] .
- [56] M. B. Hindmarsh and T. W. B. Kibble, *Rept. Prog. Phys.* **58**, 477 (1995), arXiv:hep-ph/9411342 [hep-ph] .
- [57] R. H. Brandenberger, *The Universe* **1**, 6 (2013), arXiv:1401.4619 [astro-ph.CO] .
- [58] A. Albrecht and N. Turok, *Phys. Rev. Lett.* **54**, 1868 (1985).
- [59] D. P. Bennett and F. R. Bouchet, *Phys. Rev. Lett.* **60**, 257 (1988).
- [60] B. Allen and E. P. S. Shellard, *Phys. Rev. Lett.* **64**, 119 (1990).
- [61] C. Ringeval, M. Sakellariadou, and F. Bouchet, *JCAP* **0702**, 023 (2007), arXiv:astro-ph/0511646 [astro-ph] .
- [62] V. Vanchurin, K. D. Olum, and A. Vilenkin, *Phys. Rev. D* **74**, 063527 (2006), arXiv:gr-qc/0511159 [gr-qc] .
- [63] L. Lorenz, C. Ringeval, and M. Sakellariadou, *JCAP* **1010**, 003 (2010), arXiv:1006.0931 [astro-ph.CO] .

- [64] J. J. Blanco-Pillado, K. D. Olum, and B. Shlaer, Phys. Rev. **D89**, 023512 (2014), arXiv:1309.6637 [astro-ph.CO] .
- [65] M. J. Rees, Mon.Not.Roy.Astron.Soc. **222**, 27P (1986).
- [66] T. Vachaspati, Phys. Rev. Lett. **57**, 1655 (1986).
- [67] N. Turok and R. H. Brandenberger, Phys. Rev. **D33**, 2175 (1986).
- [68] H. Sato, Progress of Theoretical Physics **75**, 1342 (1986), <http://oup.prod.sis.lan/ptp/article-pdf/75/6/1342/5338029/75-6-1342.pdf> .
- [69] A. Stebbins, "Astrophys. J." **303**, L21 (1986).
- [70] L. Perivolaropoulos, Astrophys. J. **451**, 429 (1995), arXiv:astro-ph/9402024 [astro-ph] .
- [71] O. F. Hernández, Phys. Rev. **D90**, 123504 (2014), arXiv:1403.7522 [astro-ph.CO] .
- [72] L. Pogosian, S. H. H. Tye, I. Wasserman, and M. Wyman, Phys. Rev. **D68**, 023506 (2003), [Erratum: Phys. Rev.D73,089904(2006)], arXiv:hep-th/0304188 [hep-th] .
- [73] M. Wyman, L. Pogosian, and I. Wasserman, Phys. Rev. **D72**, 023513 (2005), [Erratum: Phys. Rev.D73,089905(2006)], arXiv:astro-ph/0503364 [astro-ph] .
- [74] A. A. Fraisse, JCAP **0703**, 008 (2007), arXiv:astro-ph/0603589 [astro-ph] .
- [75] U. Seljak, A. Slosar, and P. McDonald, JCAP **0610**, 014 (2006), arXiv:astro-ph/0604335 [astro-ph] .
- [76] R. A. Battye, B. Garbrecht, and A. Moss, JCAP **0609**, 007 (2006), arXiv:astro-ph/0607339 [astro-ph] .
- [77] R. A. Battye, B. Garbrecht, A. Moss, and H. Stoica, JCAP **0801**, 020 (2008), arXiv:0710.1541 [astro-ph] .
- [78] N. Bevis, M. Hindmarsh, M. Kunz, and J. Urrestilla, Phys. Rev. **D75**, 065015 (2007), arXiv:astro-ph/0605018 [astro-ph] .
- [79] N. Bevis, M. Hindmarsh, M. Kunz, and J. Urrestilla, Phys. Rev. Lett. **100**, 021301 (2008), arXiv:astro-ph/0702223 [ASTRO-PH] .
- [80] R. Battye and A. Moss, Phys. Rev. **D82**, 023521 (2010), arXiv:1005.0479 [astro-ph.CO] .
- [81] R. H. Brandenberger and C. Vafa, Nucl. Phys. **B316**, 391 (1989).

- [82] A. Nayeri, R. H. Brandenberger, and C. Vafa, *Phys. Rev. Lett.* **97**, 021302 (2006), arXiv:hep-th/0511140 [hep-th] .
- [83] D. Wands, *Phys. Rev.* **D60**, 023507 (1999), arXiv:gr-qc/9809062 [gr-qc] .
- [84] F. Finelli and R. Brandenberger, *Phys. Rev.* **D65**, 103522 (2002), arXiv:hep-th/0112249 [hep-th] .
- [85] R. H. Brandenberger, (2012), arXiv:1206.4196 [astro-ph.CO] .
- [86] O. F. Hernandez, Y. Wang, R. Brandenberger, and J. Fong, *JCAP* **1108**, 014 (2011), arXiv:1104.3337 [astro-ph.CO] .
- [87] A. Stewart and R. Brandenberger, *JCAP* **0902**, 009 (2009), arXiv:0809.0865 [astro-ph] .
- [88] R. Brandenberger, N. Park, and G. Salton, (2013), arXiv:1308.5693 [astro-ph.CO] .
- [89] O. F. Hernandez and R. H. Brandenberger, *JCAP* **1207**, 032 (2012), arXiv:1203.2307 [astro-ph.CO] .
- [90] A. Sornborger, R. H. Brandenberger, B. Fryxell, and K. Olson, *Astrophys. J.* **482**, 22 (1997), arXiv:astro-ph/9608020 [astro-ph] .
- [91] S. M. Carroll, W. H. Press, and E. L. Turner, *Ann. Rev. Astron. Astrophys.* **30**, 499 (1992).
- [92] J. M. Bardeen, J. R. Bond, N. Kaiser, and A. S. Szalay, *Astrophys. J.* **304**, 15 (1986).
- [93] K. Olive, *Chinese Physics C* **38**, 090001 (2014).
- [94] T. W. B. Kibble, *Sixth Autumn School in Theoretical Physics Szczyrk, Poland, September 21-29, 1981*, *Acta Phys. Polon.* **B13**, 723 (1982).
- [95] T. W. B. Kibble, *COMMON TRENDS IN PARTICLE AND CONDENSED MATTER PHYSICS. PROCEEDINGS, WINTER ADVANCED STUDY INSTITUTE, LES HOCHES, FRANCE FEBRUARY 18-29, 1980*, *Phys. Rept.* **67**, 183 (1980).
- [96] E. Witten, *Nucl. Phys.* **B249**, 557 (1985).
- [97] T. Charnock, A. Avgoustidis, E. J. Copeland, and A. Moss, *Phys. Rev.* **D93**, 123503 (2016), arXiv:1603.01275 [astro-ph.CO] .
- [98] J. C. R. Magueijo, *Phys. Rev.* **D46**, 1368 (1992).
- [99] E. Jeong and G. F. Smoot, *Astrophys. J.* **624**, 21 (2005), arXiv:astro-ph/0406432 [astro-ph] .

- [100] A. S. Lo and E. L. Wright, (2005), arXiv:astro-ph/0503120 [astro-ph] .
- [101] J. Harnois-Deraps, U.-L. Pen, I. T. Iliev, H. Merz, J. D. Emberson, and V. Desjacques, *Mon. Not. Roy. Astron. Soc.* **436**, 540 (2013), arXiv:1208.5098 [astro-ph.CO] .
- [102] J. H. Traschen, *Phys. Rev.* **D31**, 283 (1985).
- [103] S. C. Olhede and A. T. Walden, *IEEE Transactions on Signal Processing* **50**, 2661 (2002).
- [104] J. L. Starck, N. Aghanim, and O. Forni, *Astron. Astrophys.* **416**, 9 (2004), arXiv:astro-ph/0311577 [astro-ph] .
- [105] K. M. Gorski, E. Hivon, A. J. Banday, B. D. Wandelt, F. K. Hansen, M. Reinecke, and M. Bartelman, *Astrophys. J.* **622**, 759 (2005), arXiv:astro-ph/0409513 [astro-ph] .
- [106] B. Leistedt, J. D. McEwen, P. Vandergheynst, and Y. Wiaux, *Astron. Astrophys.* **558**, A128 (2013), arXiv:1211.1680 [cs.IT] .
- [107] H. Padmanabhan, A. Refregier, and A. Amara, *Mon. Not. Roy. Astron. Soc.* **469**, 2323 (2017), arXiv:1611.06235 [astro-ph.CO] .
- [108] R. H. Brandenberger, *Nucl. Phys.* **B293**, 812 (1987).
- [109] Ya. B. Zeldovich, *Mon. Not. Roy. Astron. Soc.* **192**, 663 (1980).
- [110] R. Moessner, L. Perivolaropoulos, and R. H. Brandenberger, *Astrophys. J.* **425**, 365 (1994), arXiv:astro-ph/9310001 [astro-ph] .
- [111] S. Kuroyanagi, K. Miyamoto, T. Sekiguchi, K. Takahashi, and J. Silk, *Phys. Rev.* **D87**, 023522 (2013), [Erratum: Phys. Rev.D87,no.6,069903(2013)], arXiv:1210.2829 [astro-ph.CO] .
- [112] Z. Arzoumanian *et al.* (NANOGRAV), *Astrophys. J.* **859**, 47 (2018), arXiv:1801.02617 [astro-ph.HE] .
- [113] C. L. Bennett *et al.* (WMAP), *Astrophys. J. Suppl.* **148**, 1 (2003), arXiv:astro-ph/0302207 [astro-ph] .
- [114] J. E. Ruhl *et al.* (SPT), *SPIE Astronomical Telescopes and Instrumentation Symposium Glasgow, Scotland, United Kingdom, June 21-25, 2004*, *Proc. SPIE Int. Soc. Opt. Eng.* **5498**, 11 (2004), arXiv:astro-ph/0411122 [astro-ph] .

- [115] F. Lanusse, J.-L. Starck, A. Woiselle, and J. M. Fadili, in *Advances in Imaging and Electron Physics*, Vol. 183, edited by P. W. Hawkes (Academic Press, Elsevier, 2014) pp. 99 – 204, chapitre 3.
- [116] R. Brandenberger, B. Cyr, and A. V. Iyer, (2017), arXiv:1707.02397 [astro-ph.CO]
- .
- [117] R. Brandenberger, Y.-F. Cai, W. Xue, and X.-m. Zhang, (2009), arXiv:0901.3474 [hep-ph].
- [118] S. F. Bramberger, R. H. Brandenberger, P. Jreidini, and J. Quintin, **JCAP** **1506**, 007 (2015), arXiv:1503.02317 [astro-ph.CO] .
- [119] D. Barbosa, S. Anton, L. Gurwits, and D. Maia, eds., *Proceedings, Symposium 7: The Square Kilometre Array: Paving the way for the new 21st century radio astronomy paradigm (JENAM 2010)* (2012).
- [120] A. Raccanelli *et al.*, (2015), arXiv:1501.03821 [astro-ph.CO] .
- [121] E. Candès, L. Demanet, D. Donoho, and L. Ying, *Multiscale Modeling & Simulation* **5**, 861 (2006), <https://doi.org/10.1137/05064182X> .
- [122] R. N. Bracewell, *Two-dimensional Imaging* (Prentice-Hall, Inc., Upper Saddle River, NJ, USA, 1995).